Analysis of actuation and instabilities in dielectric elastomer devices

Pietro Liguori

Department of Engineering
Cardiff University

This dissertation is submitted for the degree of
Doctor of Philosophy

May 2023

I would like to dedicate this thesis to all my role models that have pushed me to be curious and question things and to everyone, not always recognised, who puts in the work to expand the horizons of human knowledge to get us to where we are today.

Declaration

This thesis is the result of my own independent work, except where otherwise stated, and the views expressed are my own. Other sources are acknowledged by explicit references. The thesis has not been edited by a third party beyond what is permitted by Cardiff University's Use of Third Party Editors by Research Degree Students Procedure

Statement 1

This thesis is being submitted in partial fulfilment of the requirements for the degree of PhD.

Statement 2

This work has not been submitted in substance for any other degree or award at this or any other university or place of learning, nor is it being submitted concurrently for any other degree or award (outside of any formal collaboration agreement between the University and a partner organisation)

Statement 3

I hereby give consent for my thesis, if accepted, to be available in the University's Open Access repository (or, where approved, to be available in the University's library and for inter-library loan), and for the title and summary to be made available to outside organisations, subject to the expiry of a University-approved bar on access if applicable.

Pietro Liguori
May 2023

Acknowledgements

I would like to express my sincere gratitude to my primary supervisor, Professor Massimiliano Gei, for his guidance, support, and encouragement throughout my PhD journey. He has always been available for me even with the difficulties of the Covid situation and distance. I am also deeply thankful to my second supervisors Dr. Zhangming Wu and Dr. Lorenzo Morini for their valuable insights and assistance. A special thanks to Dr. Ze Ji, whom I consider a friend, who helped me pursue my interest in robotics during my PhD journey.

I am grateful to my family for their love and support throughout all my studies. I also want to thank my girlfriend Bekah for her constant love and encouragement during this period, and my fellow researcher and friend Alessandro for his friendship and support and all the moments that we shared throughout this PhD journey.

I would also like to acknowledge the EPSRC for providing financial support for my research.

Abstract

Dielectric elastomer (DE) devices have gained significant interest in fields such as soft robotics, mechanical engineering, biomedical technology, and energy engineering due to their lightweight and fast actuation capabilities. However, these devices have several shortcomings that this thesis aims to address through the analysis of instabilities and actuation in various configurations.

The electroelasticity theory is presented, defining the general kinematics and constitutive equations for these hyperelastic materials. Using this theory as a foundation, various configurations are introduced and analysed, with a focus on the novel ‘floating’ device as both a slab and tubular elastomer. These configurations are examined under different boundary conditions, and the deformation paths are analysed as geometrical parameters are varied. The onset of electro-mechanical instability is shown, as well as the introduction of the expansion limit.

The theory of incremental deformations is specialised to investigate surface instabilities in three previously introduced elastomer slab configurations. It is shown that the instability is more sensitive to pre-stress in the ‘floating’ configuration, while the configuration deformed by sprayed charges is more stable against surface instabilities compared to the same configuration actuated by voltage. The effects of stiff electrodes on surface instabilities are also studied using surface-coating models, and it is demonstrated that the stability domain is significantly reduced when the device contracts. New bifurcation modes come into play and each one has been studied and characterised.

Laminated composite elastomers are then considered, which are of particular interest due to their ability to enhance actuation characteristics. Using a small strain model and various boundary conditions, it is shown how, with specific parameters, an inverse mode of actuation can be achieved in both rank-1 and rank-2 laminated composites. The rank-2 laminate is demonstrated to enhance the rank-1 inverse actuation mode, and a guideline for optimizing composite parameters is provided. Existing materials are also analysed to show how

current technology requires a rank-2 laminate to obtain the inverse mode of actuation.

Table of contents

List of figures

List of tables

Chapter 1

Introduction

1.1 Electro-active polymers

The use of electro-active polymers (EAPs) is an ever-growing field with an increasing number of applications and research articles. As a type of EAP, dielectric elastomers (DEs) work as an actuator, which typically consists of an elastomer membrane actuated by a difference in electric potential across the thickness, which induces in-plane large strains. Comparing these to other actuation technologies, such as piezoelectric, magnetostrictive, and shape memory materials, the advantages of DEs include low density and strain modulus, large actuation strain coupled with fast actuation speed and high specific energy density. These lightweight and flexible actuators have attracted interest in areas such as soft robotics [7–9], mechanical [10–12], biomedical [13–15] and energy engineering [16–18, 6] (the review [19] provides a broad overview of the topic). The mechanisms of DEs have been known for a long time, with Röntgen showing in 1880 [20] how a pre-stretched rubber band showed elongation when subjected to an electric field. In the last two decades, improvements in material science and fabrication technology, which have made these devices viable, have led to increased interest in DE actuators. In 1998 Pelrine et al. [21] showed a bending actuator with one layer of silicon rubber coated with polyamide electrodes showing strains of $> 30\%$. This was followed up with a paper in 2000 [22] showing increased strains of up to 215% with the use of acrylic elastomers and the application of high pre-strain.

In the robotics field, these advancements coupled with a shift from conventional rigid body robots to soft robots with compliant bodies have made DE actuators of particular interest. Several reviews exist which lay out recent advancements and challenges of DEA applications in soft robotics such as Gu et al. [23], Gupta et al. [24] and Yuon et al. [25] among others. So far soft actuators have allowed many designs of artificial muscles, bio-inspired robots and user interfaces. Soft robotics is preferred for robots that need to interact with humans and unstructured environments where large deformations are required with little pressure or damage when manoeuvring. DE actuators can be stacked or designed to allow various deformation modes. This has allowed various locomotion designs using soft actuators as seen in Fig. 1.1 (a) and (b) which show a rolling DE device proposed by Li et al. [1] and a frog inspired DE actuated robot proposed by Tang et al. [2] respectively. Wearable robotics is another important challenge where soft actuators are of interest because of the weight and comfort requirements. Fig 1.1 (c) shows a wearable fingertip tactile display proposed by Koo et al. [3]. Challenges for DE actuators in soft robotics remain the requirement of high voltage for actuation, limited breakdown strength of actuators, and poor reliability due to unexpected breakdown phenomena or various types of instabilities.

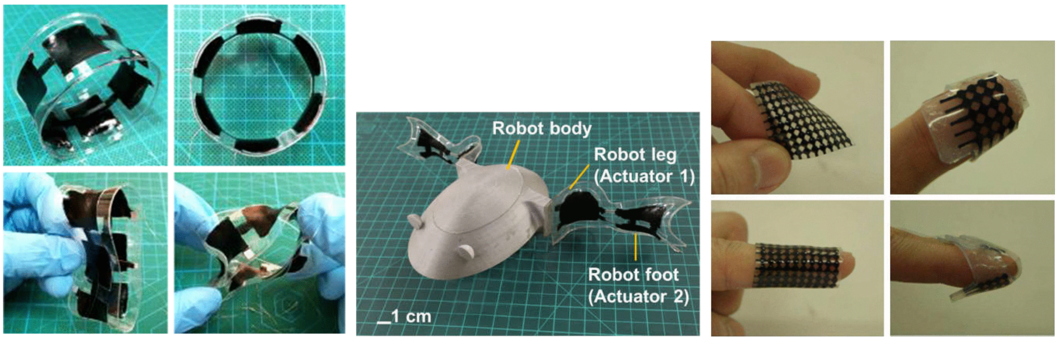

(a) Rolling robot (b) Frog inspired robot (c) Tactile display

Fig. 1.1 Three DE driven designs: (a) rolling robot using DEA for locomotion [1], (b) frog inspired DE actuated robot [2], (c) wearable fingertip tactile display [3]

A DE device can also be used as a dielectric elastomer generator (DEG), by exploiting the fact that the capacitance of the dielectric changes during deformation to extract electric energy. The general load cycle works by initially stretching then charging and subsequently releasing the capacitor and collecting the charge at a higher electric potential. Springhetti et al. [26] investigated the optimal cycle for a DEG within the electric breakdown and stretch limits of an elastomer. DEGs are a promising technology for the conversion of mechanical energy into electrical energy due to their very large energy densities, good efficiency, and extremely low cost of the constituent materials compared to other generator technologies. Moretti et al. [27] provided a review of state of the art small and large scale DEG systems DEGs are seeing development both in small-scale devices conceived for wearable or portable power systems for other wearable electronics and in large-scale systems such as generators designed for renewable energy conversion. DEGs have been proposed such as embedded in a shoe heel or backpack straps to potentially power portable electronics [17]. The challenges with small-scale DEGs are safety due to the high voltages required and the need for low-cost solutions for the step-down electronics required to provide the low voltage usable output. DEGs have been recognised particularly for use in wave energy converter technologies. The advantages of DEGs compared to more typical generators are the simplicity and low cost of the raw materials, the low mass density, the resistance of DE materials to corrosion and in particular the matching between the frequency of waves with the DEG working cycle. Wave energy DEGs are currently in the proof-of-concept stage with small scale prototypes in laboratory environments. Several architectures have been studied such as floating buoys or oscillating bodies and water columns. Fig. 1.2 shows a few of these different devices.

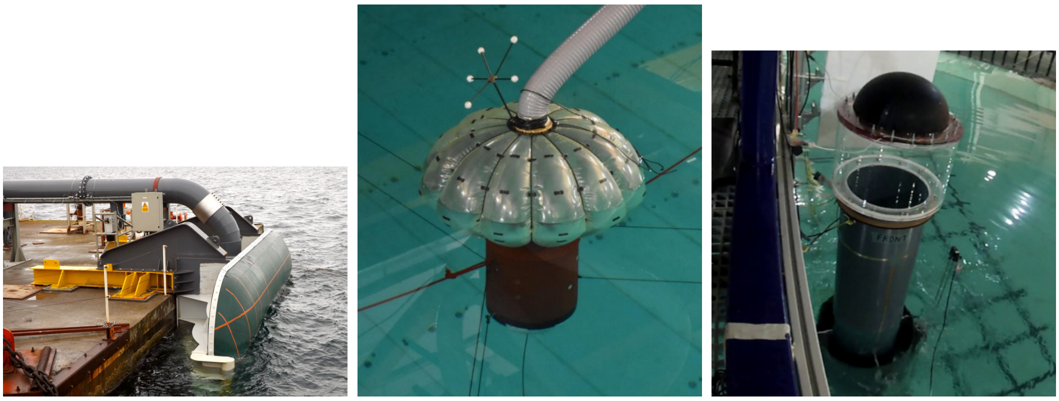

(a) AWS-III (b) SQ1 (c) Poly-A-OWC

Fig. 1.2 Three DEG prototype devices: (a) cassette type horizontal diaphragm DEG [4], (b) air-filled bags used as DEG [5], (c) vertical diaphragm DEG [6]

Overall the challenges in design are similar for all the reviewed applications. These include understanding what causes breakdown and instabilities, being able to achieve specific types of deformations fitted to the task as well as overall larger deformations for a given actuation voltage by improving the properties of DEs. A common problem is also that the high voltage needed to operate a DE device can present safety issues and require electrical circuits able to handle the voltage conversion in small form factor.

1.2 Instabilities

It is evident that one of the main issues to consider when designing DE devices are the onset of instabilities. There are several types of instablities that can affect such a device which will be summarised here.

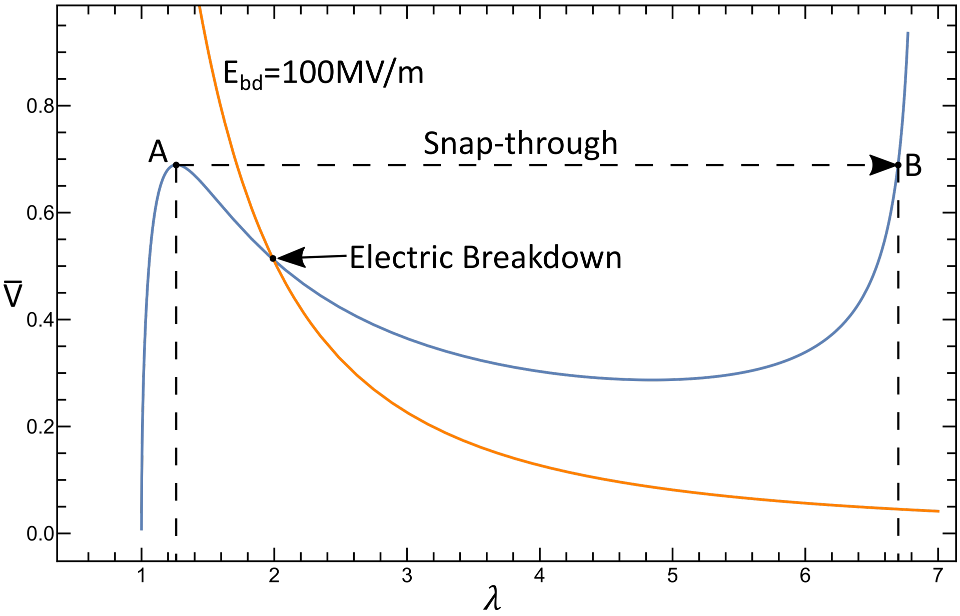

Fig. 1.3 Figure showing a fundamental loading path for an elastomer slab undergoing equi-biaxial deformation in blue and the electric breakdown curve in orange. The onset of electro-mechanical instabilities and electric breakdown are highlighted.

Electro-mechanical instabilities

Electro-mechanical instabilities occur when the nonlinear voltage-stretch response curve reaches a peak point [28]. Figure 1.3 shows an example of an elastomer slab undergoing equi-biaxial deformation with a Gent material model. As can be seen, when the actuation voltage reaches the peak at point A, the elastomer experiences a snap-through instability causing the elastomer to thin down drastically. This occurs because of a positive feedback between the elastomer thinning and the electric field increasing which only ceases (point B) at a state close to the limiting stretch due to the elastomer chain extensibility. Typically this type of instability triggers the electric breakdown of the material, shown as an example with the orange curve in the figure. However, there are some studies which try to harness this snap-through instability to achieve giant deformations such as by Su et al. [29].

Diffuse modes of bifurcation

Diffuse buckling modes can be induced under compression of the elastomer [30, 31]. They are typical of a pre-stretched elastomer, where the pre-stress may reduce due to the electrical actuation. These instabilities can be detected by investigating the propagation of small-amplitude perturbations superimposed on a given deformation state. When this study is done for a half-space it reveals surface instabilities.

Electric breakdown

The electric or dielectric breakdown is a failure mode arrising from an intrinsic property of the dielectric material, called its dielectric strength, and can be observed experimentally. It occurs when the dielectric material is being subjected to a large enough electric field which causes it to suddenly becomes a conductor allowing current to flow. This type of failure mode causes catastrophic failure of the DE device. Typical dielectric strength values of elastomer materials range in the hundreds MV/m [22, 32]. Often other types of instabilities lead to electric breakdown as any local thinning of the elastomer could cause high enough electric fields for breakdown to occur as is shown in figure 1.3 with the electro-mechanical instability.

1.3 Literature Review

The aim of this thesis' work was to carry out novel research to advance the understanding of acuation of DE devices. To achieve this goal a couple of different focus areas were picked, highlighting for each some novel phenomena. At first novel configurations were investigated and their fundamental loading paths were studied in order to advance general knowledge of potential devices. The onset of instabilities pertaining to these new configurations was investigated in order to understand the operating regimes. Surface instabilities were also analysed for the classical configuration but enriched with a surface coating model to include the effects of a stiff electrode. Hierarchical laminated composites configurations were also investigated as a way to enhance traditional DE actuation. This section of the thesis breaks down each chapter and provides for each detailed insight on existing research and highlights on the novel aspects of this work.

1.3.1 Chapter 2 - Electroelasticity for homogeneous materials

Chapter 2 introduces the general continuum mechanics theory used to analyse electroactive elastomer devices throughout the thesis. The first theory for non-linear electro-elasticity was developed by Toupin [33]. McMeeking and Landis [34] derived the governing equations in Eulerian form using a free energy function dependent on the deformation gradient and material polarization. They also obtained the constitutive equations for the electric field and total Cauchy stress for non-dissipative materials. Dorfmann and Ogden [35] then expanded the theory by providing a novel Lagrangian formulation based on the notion of a total energy function. This led to simple and compact forms of the governing and constitutive equations facilitating the formulation of boundary-value problems. Suo et al. [36] expanded on this theory by using a different starting point. The general theory for electroactive elastomer devices is now well established.

Several constitutive models for hyperelastic materials are then introduced which are used throughout the thesis to describe the stress-strain relationship of the elastomers. A myriad of models have been proposed with new models to account for specific characteristics still being proposed to date, such as Xiang et al. [37]. In this thesis the purely elastic effects are assumed decoupled from the electrostatic effects, allowing the use of existing mechanical models to be employed with an ideal dielectric electro-elastic model. Several investigations showed that the decoupled free energy well captures the behaviour of dielectric elastomers [38–40].

Lastly, the incremental electro-elasticity theory is introduced as developed by Dorfmann and Ogden [30]. Incremental deformations and electric fields are superimposed on a known underlying finite deformation and electric field. This theory will be used in chapter 4 to investigate diffuse modes of instabilities on a half-space.

1.3.2 Chapter 3 - Electro-elastic boundary value problems

In chapter 3 some electro-elastic boundary value problems are introduced. The classic configuration for these actuators (first reported by Pelrine et al. [21]) consists of an elastomer film sandwiched between compliant electrodes (carbon grease, ion-implanted polymers, ionogels, etc.). The device is actuated by applying a potential difference across the electrodes. Spraying charges directly on the surface of the elastomer is another way to actuate a dielectric elastomer film. This method was pioneered by Röntgen [20] and proposed recently by Keplinger et al. [41] who showed experimentally how surface charges could be sprayed onto the elastomer. These first two modes are well known and the governing equations are expressed and briefly discussed for further use in chapter 4 to analyse surface instabilities. A third possible actuation mode is that where the membrane 'floats' between two fixed electrodes surrounded by either a fluid or a vacuum and is actuated via a potential difference across the electrodes. This was proposed by Díaz-Calleja et al. [42] who addressed non-linear actuation law and pull-in instability in terms of contrast between dielectric permittivities of the elastomer and surrounding environment. Su et al. [43] also examined the Hessian instability of a dielectric slab floating in a conductive fluid undergoing equi-biaxial deformation. The fundamental paths have not been well defined and as such in this chapter a deeper analysis of the fundamental paths of the 'floating' elastomer, under plane-strain conditions, is undertaken. This is used to understand how changing the geometrical parameters of the device affects the actuation. The idea of the expansion limit, where the elastomer expands up to the fixed electrodes, is also introduced and the onset of electro-mechanical instability is analysed using both a neo-Hookean and Gent constitutive model.

The 'floating' elastomer is then modified to use a tubular configuration, such that a tubular elastomer is placed in between two fixed coaxial tubular electrodes and actuated via a potential difference across them. There has been work on a tubular elastomer in a classical configuration with attached compliant electrodes, which was proposed by Pelrine et al. [21]. Dorfmann and Ogden [44] first reviewed an elastomer with cylindrical symmetry analysing the extension and inflation of a tube with axial or radial electric field. Zhu et al. [45] then analysed the onset of electro-mechanical instability of a tubular elastomer with varying amounts of pre-stretch. Calabrese et al. [15] also showed a potential medical bandage device using the concept of sandwiched electro-active tubular structures with attached electrodes. However, there has not been any work on the 'floating' configuration, where the elastomer tube is subjected to an external electric field. In this chapter the governing equations of the problem are expressed using a cylindrical co-ordinate system. Two boundary conditions are then analysed, the first when the transverse stretch λ_z is held constant and the second where it is allowed to vary as a function of the radius. The fundamental paths of the geometry are analysed as the parameters are altered, to understand the deformation of the tubular device when actuated, as well as the conditions for the onset of electro-mechanical instabilities.

1.3.3 Chapter 4 - Electro-elastic surface instabilities

In chapter 4 a systematic approach is undertaken to investigate surface bifurcations of electro-elastic half-spaces deforming homogeneously in the fundamental path according to the three actuated elastomer slab devices introduced in chapter 3.

There are several methods to investigate instabilities of an elastomer, such as the internal stress balance, the hessian method and the energy method with Dorfmann and Ogden providing a review of instabilities of soft dielectrics [46]. In this thesis the incremental method is used to analyse diffuse modes of instabilities on a half-space. The general theory, developed by Dorfmann and Ogden [30] and laid out in chapter 2, is specialised in this chapter to the three actuated elastomer slab devices introduced in chapter 3. A systematic approach is undertaken to investigate surface bifurcations of the electro-elastic half-spaces deforming homogeneously in the investigated fundamental paths. This method has been used to analyse bifurcations by authors such as Dorfmann and Ogden [47], Díaz-Calleja et al. [48], Su et al. [49], in elastomer blocks and thin films. It has also been used to investigate instabilities in dielectric composites such as by Bertoldi and Gei [31], Rudykh et al. [50, 51] and Spinelli and Lopez-Pamies [52]. In this thesis the focus is on surface instabilities, with particular interest on the ‘floating’ elastomer actuation as the geometrical parameters are changed. Incremental fields are also analysed to characterise the surface instability modes at the onset of bifurcation.

The effect of the stiffness of electrodes is commonly neglected in electro-elastic actuation as they are assumed to be fully compliant. Elastic surface-substrate interactions, a valid model for thin and stiff films coating elastic solids, were analysed by Murdoch [53] and later by Ogden and Steigmann [54, 55] who refined the theory and introduced the bending stiffness. The latter approach is used to take into account the additional effects of the electrode on surface bifurcations of the previously analysed half-space using the compliant electrodes actuation mode. Guided by experimental measurements, three different kinds of electrodes are analysed possessing a range of material parameters to cover a variety of cases and assess their effects on electro-elastic surface instabilities and bifurcation modes. The results show that they may limit considerably the stability domain when the half-space contracts.

1.3.4 Chapter 5 - Small strain actuation of electro-elastic laminates

Composite dielectric elastomers exhibit a variety of interesting actuation features. A significant part of the research has been focused on (hierarchical) layered components, looking at overcoming some of the previously mentioned limitations that affect DEAs. The key principle is to enhance the electro-mechanical coupling by reinforcing a soft matrix with stiff, high permittivity particles, such that the overall actuation is improved despite the expected increase in stiffness. A homogenization framework for characterizing the behaviour of laminated composites was provided by deBottom et al. [56] and Tevet-Deree [57]. Several papers investigated the optimisation of layered composites, such as Rudykh et al. [50], Gei et al. [58], Gei and Mutasa [59], among others. In the small strain setting, Tian et al. [60] showed that two-phase dielectric rank–n laminates could exhibit improvements in the actuation strain of more than one order of magnitude.

In this chapter laminate composites are studied which are characterised by a softer matrix material laminated with a stiffer inclusion. It is shown that laminate composite elastomers can also exhibit an inversion of actuation with the right geometrical and material parameters. To better understand this mode of actuation the conditions which cause the onset of this actuation inversion are analysed. The presence of this inversion of actuation is shown in both rank–1 and rank–2 laminates. At first the rank–1 laminate is analysed, looking at the geometrical and material criteria with different boundary conditions, namely, ‘aligned’ loading and macroscopic stress-free conditions. The actuation response is analysed to understand how each composite phase deforms before, during and after the onset of inversion. A rank–2 composite is then compared against a rank–1 composite and it is shown how the rank–2 structure is able to enhance this mode of actuation. As a rank–2 has a lot more parameters, a general guideline is provided on how to optimise each to obtain the desired actuation.

Finding the right material for each soft and stiff material phase is crucial to the actuation response of the composite and is the main challenge when trying to achieve the results shown. The development of new soft electro-active materials with enhanced permittivity is an ongoing field of study. A review of currently studied materials is provided, highlighting those which could potentially be used in each material phase to achieve the inversion of actuation in both rank–1 and rank–2 laminate composites.

The research results in this thesis have also been published in

Liguori, P., Gei, M., "Surface instabilities of soft dielectric elastomers with implementation of electrode stiffness", *Math. Mech. Solids*, March 2022,

Liguori, P., Gei, M., "New actuation modes of composite dielectric elastomers" has been submitted for peer review to *Proc. R. S. A.*

A short note on "Large deformation of soft dielectric cylindrical tubes under external radial electric field" is also in the works.

Chapter 2

Electroelasticity for homogeneous materials

This thesis will analyse electroactive elastomer devices using a continuum mechanics approach. The underlying theory has been developed for many years and for additional information, the interested reader is referred to Truesdell et al. [61], Gurtin [62] and Holzapfel [63], among others. This chapter contains an introduction to the general theory of large-strain electro-elasticity for a homogeneous isotropic material developed by Toupin [33] in 1956. An electro-elastic elastomer device consists of an elastomer with a coupled electromechanical response to an applied electric field. This chapter will define the general kinematics and constitutive equations describing this coupled response of the material.

2.1 Kinematics and field equations

Figure 2.1 shows a homogeneous material in its initial and deformed configurations. We assume that in the stress-free configuration the electro-elastic material occupies a region $B^0 \in \mathbb{R}^3$. After a given deformation $\boldsymbol{\chi}$, the deformed body covers a space $B \in \mathbb{R}^3$. We can define a material particle in B^0 by its position vector $\boldsymbol{x}^0$ that is transformed to $\boldsymbol{x} = \boldsymbol{\chi}(\boldsymbol{x}^0)$ in B; $\boldsymbol{F} = \partial\boldsymbol{\chi}/\partial\boldsymbol{x}^0$ denotes the deformation gradient. The space surrounding the body will be denoted by B^{sur} or $B^{0^{sur}}$ in the deformed or undeformed configuration respectively. The particular case of vacuum will be denoted by B^*, where no undeformed configuration is introduced in the case of a vacuum as the deformation gradient is undefined.

In the mechanical problem, the stress is caused by surface tractions per unit area A. These are denoted as $\boldsymbol{t}$ in the deformed configuration B with the outward unit normal vector denoted as $\boldsymbol{n}$. From Cauchy's theorem it is known that these tractions cause a second order stress tensor known as the Cauchy stress tensor $\boldsymbol{\tau}_{mech}$ in the deformed configuration, given by

$$\boldsymbol{t} = \boldsymbol{\tau}_{mech}\boldsymbol{n}. \tag{2.1}$$

The Eulerian equation of motion is given by

$$\mathrm{div}\boldsymbol{\tau}_{mech} + \boldsymbol{b} = \rho\boldsymbol{a}, \tag{2.2}$$

where $\boldsymbol{b}$, ρ and $\boldsymbol{a}$, are the body forces, density and acceleration respectively in B. The div is the divergence operator in the deformed configuration B. Under the assumption of no body forces and a static problem the equilibrium equation reduces to

$$\mathrm{div}\boldsymbol{\tau}_{mech} = \boldsymbol{0}. \tag{2.3}$$

In the electric part of the problem, the surface charges on the electro-elastic body together with the polarization of the material generate an electric field $\boldsymbol{E}$ in the whole deformed space B. The electric displacement field within the material $\boldsymbol{D}$ is thus given by

$$\boldsymbol{D} = \varepsilon_0\boldsymbol{E} + \boldsymbol{P}, \tag{2.4}$$

where $\boldsymbol{P}$ is the polarization of the material and ε_0 the permittivity in vacuum. In a vacuum or a non polarizable medium, this relation turns into

$$\boldsymbol{D} = \varepsilon_0\boldsymbol{E}. \tag{2.5}$$

In order to formulate the equilibrium equations, a 'total' stress tensor, $\boldsymbol{\tau}$, should be defined which includes the electro-mechanical effects in B such that

$$\boldsymbol{\tau} = \boldsymbol{\tau}_{mech} + \boldsymbol{\tau}_{elec}. \tag{2.6}$$

Under the assumption of the absence of both volume free charges and body forces, the governing equations in the eulerian formulation are the following:

$$\mathrm{div}\boldsymbol{\tau} = \boldsymbol{0}, \quad \mathrm{div}\boldsymbol{D} = 0, \quad \mathrm{curl}\boldsymbol{E} = \boldsymbol{0}, \tag{2.7}$$

with curl being the curl operator in the deformed configuration B. The balance of angular momentum also requires that

$$\boldsymbol{\tau} = \boldsymbol{\tau}^T. \tag{2.8}$$

The last equation implies that $\boldsymbol{E}$ can be derived from the electric potential $\phi(\boldsymbol{x})$ such that $\boldsymbol{E} = -\text{grad}\phi(\boldsymbol{x})$.

When the surrounding of the body is a vacuum (B^*), there is a surface force acting on the body due to the electric field which is given by the Maxwell stress tensor $\boldsymbol{T}^*$ i.e.

$$\boldsymbol{T}^* = \varepsilon_0\Big(\boldsymbol{E}^* \otimes \boldsymbol{E}^* - \frac{1}{2}(\boldsymbol{E}^* \cdot \boldsymbol{E}^*)\boldsymbol{I}\Big), \tag{2.9}$$

where * denotes quantities in a vacuum. Here the Maxwell stress tensor does not take into account any magnetic effects as throughout this work they are assumed to be null. The permittivity of a vacuum has the value of, $\varepsilon_0 = 8.85 \cdot 10^{-12}$ F m^{-1} and $\boldsymbol{I}$ is the appropriate identity tensor. The electric quantities in the vacuum follow the relationship previously described, $\boldsymbol{D}^* = \varepsilon_0\boldsymbol{E}^*$, while eq. $(2.10)_4$ implies an electric potential in the vacuum given by $\boldsymbol{E}^* = -\text{grad}\phi^*(\boldsymbol{x})$.

With a surrounding vacuum, the governing eqs. (2.7) and (2.8) specialise to,

$$\text{div}\,\boldsymbol{T}^* = \boldsymbol{0}, \quad \boldsymbol{T}^* = (\boldsymbol{T}^*)^T, \quad \text{div}\boldsymbol{D}^* = 0, \quad \text{curl}\boldsymbol{E}^* = \boldsymbol{0}, \tag{2.10}$$

where the total stress has null mechanical contribution and is given by the Maxwell stress only.

The boundary conditions need to be prescribed due to the discontinuity between the homogeneous solid material B and the surrounding space B^{sur} as demonstrated in figure 2.2. Because of the discontinuity, we define jump conditions across as

$$[\![\xi]\!] = \xi_B - \xi_{B^{sur}}, \tag{2.11}$$

with ξ being some variable defined in both the material and surrounding space. In the deformed configuration these boundary conditions take the form,

$$\boldsymbol{n} \cdot [\![\boldsymbol{D}]\!] = -\omega, \quad \boldsymbol{n} \times [\![\boldsymbol{E}]\!] = \boldsymbol{0}, \quad [\![\boldsymbol{\tau}]\!]\boldsymbol{n} = \boldsymbol{t}, \tag{2.12}$$

where ω is the surface charge density and $\boldsymbol{t}$ are any prescribed surface tractions. When the discontinuity occurs at the boundary between the elastomer B and an adjacent vacuum B^*, the above equations specialise as

$$\boldsymbol{n}\cdot\boldsymbol{D} = -\omega + \varepsilon_0\boldsymbol{E}^*\cdot\boldsymbol{n}, \quad \boldsymbol{n}\times(\boldsymbol{E}-\boldsymbol{E}^*) = \boldsymbol{0}, \quad \boldsymbol{\tau}\boldsymbol{n} = \boldsymbol{t} + \boldsymbol{T}^*\boldsymbol{n}. \tag{2.13}$$

It could be useful to define nominal or Lagrangian measures. It can be more useful to have a measure of the first Piola-Kirchhoff tensor which is a two point tensor linking the total stress to the undeformed area A^0. According to Nanson's formula we have

$$\boldsymbol{n}dA = J\boldsymbol{F}^{-T}\boldsymbol{n}^0 dA^0, \tag{2.14}$$

where J is the Jacobian given by $J = \det\boldsymbol{F}$ and $\boldsymbol{n}^0$ is the outward unit normal vector in the undeformed configuration. If the material is incompressible then $J = 1$. We can thus use this to obtain the Piola-Kirchhoff total stress tensor $\boldsymbol{S}$ given by,

$$\begin{aligned} \boldsymbol{t}dA = \boldsymbol{\tau}\boldsymbol{n}dA &= \boldsymbol{S}\boldsymbol{n}^0 dA^0 \\ \boldsymbol{S} &= J\boldsymbol{\tau}\boldsymbol{F}^{-T}. \end{aligned} \tag{2.15}$$

The governing eqs. (2.7) and (2.8) updated to the reference configuration thus become:

$$\mathrm{Div}\boldsymbol{S} = \boldsymbol{0}, \quad \boldsymbol{S}\boldsymbol{F}^T = \boldsymbol{F}\boldsymbol{S}^T, \quad \mathrm{Div}\boldsymbol{D}^0 = 0, \quad \mathrm{Curl}\boldsymbol{E}^0 = \boldsymbol{0}, \tag{2.16}$$

where Div and Curl are the appropriate operators with respect to coordinates in B^0. The Lagrangian electric displacement and electric fields are given by

$$\boldsymbol{D}^0 = J\boldsymbol{F}^{-1}\boldsymbol{D}, \quad \boldsymbol{E}^0 = \boldsymbol{F}^T\boldsymbol{E}, \tag{2.17}$$

respectively. The jump conditions eqs. (2.12) in the Lagrangian formulation take the form of,

$$\boldsymbol{n}^0\cdot[\![\boldsymbol{D}^0]\!] = -\omega^0, \quad \boldsymbol{n}^0\times[\![\boldsymbol{E}^0]\!] = \boldsymbol{0}, \quad [\![\boldsymbol{S}]\!]\boldsymbol{n}^0 = \boldsymbol{t}^0, \tag{2.18}$$

with all the appropriate quantities in the reference configuration.

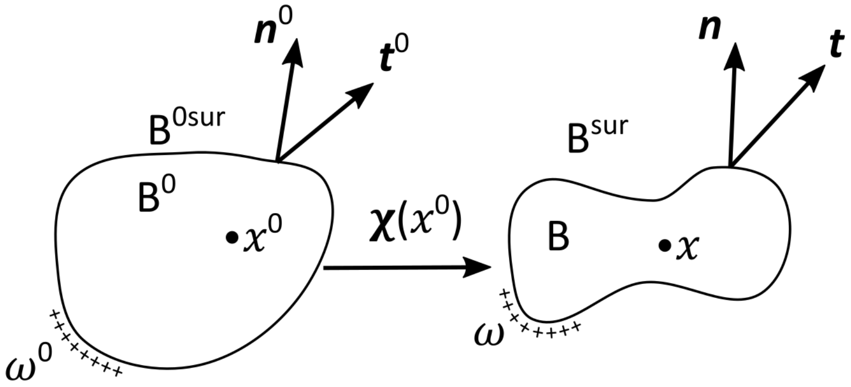

Fig. 2.1 Diagram of a homogeneous material body in undeformed (left) and deformed (right) configurations, with surface tractions $\boldsymbol{t}$ and charges ω on its boundary.

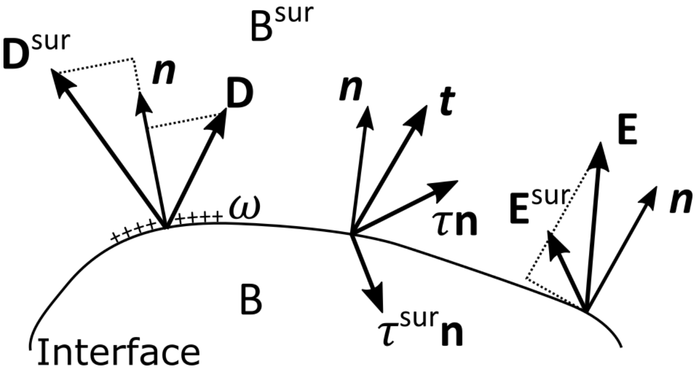

Fig. 2.2 Diagram showing jump conditions at an interface in the deformed configuration, with surface tractions $\boldsymbol{t}$ and charges ω on its boundary.

2.2 Electro-elastic constitutive equations

This section deals with the selection of a constitutive equation to model the elastomer materials used for dielectric elastomer devices. The aim is to introduce constitutive models suitable to describe the stress-strain relationship, as such we are particularly interested in hyperelastic material models or ‘Green’ elastic materials. This field is of particular interest in polymer chemistry, polymer physics and polymer engineering, where there exist many studies trying to accurately model and describe the stress-strain relationship of elastomer materials [64–66]. The range of models to pick from is vast and can be broadly classified into three classes. The first are phenomenological models where the model describes the empiric behaviour of the material observed from testing. This type of model does not attempt to describe the first principles of the ongoing phenomena but merely tries to fit a curve to the data. The second class of models are the mechanist models where the model tries to understand the macro and microscopic properties of the material to deduce how it will respond. These kinds of models tend to look at how elastomer chains stretch and interact at a molecular level in order to obtain their mathematical relationship. The third and final class of models is the hybrid of these two, where some elements are taken from each of the two previous classes to obtain the material model.

When picking an adequate material model there are certain factors to keep into account. Ideally, the model should have as few parameters as possible which should be obtainable from a small number of experiments to characterise each specific elastomer. It is also important to understand how much deformation the material will undergo, as some models are more suited than others in the various stages of deformation.

The dielectric elastomers considered can be defined by an electro-elastic strain-energy function W which is based on the deformation gradient and nominal electrical displacement $\boldsymbol{D}^0$ such that

$$W = W(\boldsymbol{F}, \boldsymbol{D}^0). \tag{2.19}$$

For this type of material, the constitutive equations take the form

$$\boldsymbol{S} = \frac{\partial W}{\partial \boldsymbol{F}}, \quad \boldsymbol{E}^0 = \frac{\partial W}{\partial \boldsymbol{D}^0}. \tag{2.20}$$

When the material is said to be incompressible it is known that $J = \det\boldsymbol{F} = 1$, meaning that the incompressibility constraint becomes $J - 1 = 0$. To account for the incompressibility of the material, the strain-energy function can be written in the form of

$$W = W(\boldsymbol{F}, \boldsymbol{D}^0) - p(J-1), \tag{2.21}$$

where p represents an unknown hydrostatic pressure to be defined by boundary conditions, functioning as a Lagrange multiplier. The incompressible constitutive equations now take the form

$$\boldsymbol{S} = \frac{\partial W}{\partial \boldsymbol{F}} - p\boldsymbol{F}^{-T}, \quad \boldsymbol{E}^0 = \frac{\partial W}{\partial \boldsymbol{D}^0}. \tag{2.22}$$

Isotropy requires that $W(\boldsymbol{F}, \boldsymbol{D}^0)$ be a function of both the invariants of the right Cauchy-Green tensor $\boldsymbol{C} = \boldsymbol{F}^T\boldsymbol{F}$, namely

$$I_1 = \mathrm{tr}\boldsymbol{C}, \quad I_2 = \frac{1}{2}\Big[(\mathrm{tr}\boldsymbol{C})^2 - \mathrm{tr}(\boldsymbol{C}^2)\Big], \quad I_3 = \det\boldsymbol{C} = 1, \tag{2.23}$$

and those involving both $\boldsymbol{C}$ and $\boldsymbol{D}^0$, i.e.

$$I_4 = \boldsymbol{D}^0 \cdot \boldsymbol{D}^0, \quad I_5 = \boldsymbol{D}^0 \cdot \boldsymbol{C}\boldsymbol{D}^0, \quad I_6 = \boldsymbol{D}^0 \cdot \boldsymbol{C}^2\boldsymbol{D}^0. \tag{2.24}$$

It is to note that a convenient form of the energy function $W(I_i)$ $(i = 1, \dots, 6)$ is the one where the purely elastic part is split from the remaining part involving coupled electrostatic effects, namely $W(I_i) = W_{elas}(I_1, I_2) + W_{elec}(I_4, I_5, I_6)$. This allows existing purely mechanical hyperelastic models to be employed by adding an appropiate model for the coupled effects.

2.2.1 Neo-Hookean elastic model

Simple models that are easier to handle analytically are of particular interest. For the elastic part of the strain-energy, the simplest of all commonly used hyperelastic models is the neo-Hookean model. The neo-Hookean model is a mechanistic model expressed in terms of invariants by Rivlin [67] and based on the statistical thermodynamics of cross-linked polymer chains. It is particularly fitting for lower stretch values as the polymer chains are able to move relative to each other when a stress is applied. The strain-energy function for an incompressible neo-Hookean material is defined as,

$$W_{elas}(I_1) = \frac{\mu}{2}(I_1 - 3), \tag{2.25}$$

where μ is the shear modulus of the material. The advantages of the neo-Hookean model are its simplicity while still providing accurate results for small to medium strain conditions. The material parameter required is also easily obtained experimentally and compatible with various types of deformations.

2.2.2 Gent elastic model

The Gent material model is a hybrid model proposed by Gent [68] in 1996. It tries to improve on the shortcoming of the neo-Hookean model at large strains by providing a limiting strain factor that is fitted to experimental data. It is the simplest model that deals with the problem of limiting polymer chain extensions; as the polymer chains stretch out they reach a limit over which they are unable to stretch anymore. The Gent material model for incompressible elastomers is defined as,

$$W_{elas}(I_1) = -\frac{\mu J_m}{2} \mathrm{Ln}\left(1 - \frac{I_1 - 3}{J_m}\right). \tag{2.26}$$

The limit of stretch is defined by the Gent parameter $J_m = I_1^{lim} - 3$ where I_1^{lim} is the first invariant evaluated at the stretch limit value. As $J_m \to \infty$, such that the stretch limit is not a factor, the neo-Hookean model is obtained. This model, in many cases, is able to accurately simulate strain stiffening by only introducing an extra variable.

To achieve a better understanding of the stretch ranges in which each of these mechanical models is better, a material slab under plane-strain conditions is analysed. Figure 2.3 shows the results for a neo-Hookean and Gent material model with a typical Gent parameter for an elastomer of $J_m = 91$. The mechanical stress $\boldsymbol{\tau}_{mech}$ is plotted as the elastomer is stretched along the x_1 axis. As can be seen up until a stretch of $\lambda_1 = 2$ the results between the neo-Hookean and Gent are almost identical. After that there is a transition zone between $\lambda_1 = 2$ and $\lambda_1 = 4$, where the two models show a similar response, with the Gent showing 18% higher stress at $\lambda_1 = 4$. For higher stretch values the neo-Hookean model diverges from the Gent model, with the Gent model being more accurate for these stretch ranges when compared to experimental results.

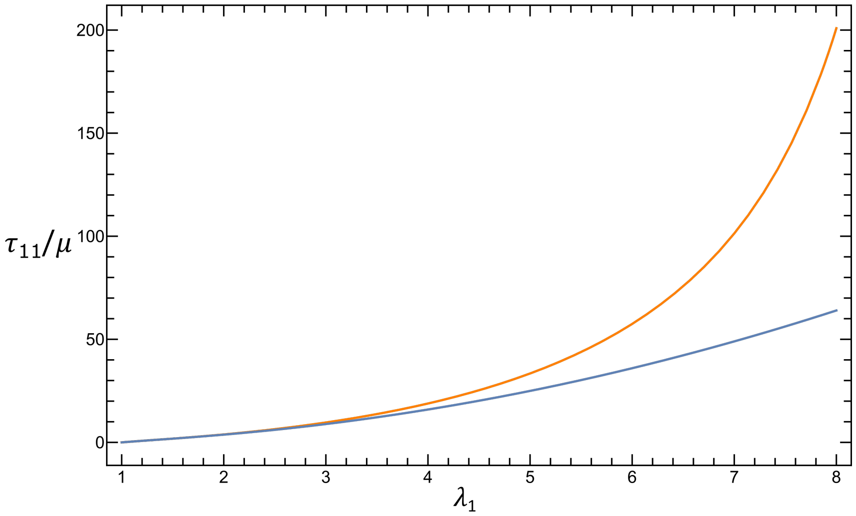

Fig. 2.3 Comparison between the neo-Hookean and Gent material models, shown in blue and orange respectively, using a material slab in plane-strain conditions. A Gent parameter of $J_m = 91$ is used.

2.2.3 Electro-elastic model

This thesis aims to investigate electro-elastic problems where the material behaves as an ideal dielectric, i.e. the permittivity of the material ε is independent of the strain. While this is not exact, as the permittivity of the material will change as it is stretched, it is a good approximation as large deformations are needed to show noticeable changes in permittivity. Kurimoto et al. [69] showed that with a uniaxial stretch ratio of 3 the permittivity decreased by 7.6% and 10.7% for an acrylic and silicone elastomer respectively with a linear trend. This behaviour can be captured by a strain-energy function depending only on the 5th invariant, of the form

$$W_{elec}(I_5) = \frac{1}{2\varepsilon} I_5, \tag{2.27}$$

where through eq. $(2.22)_2$ and eqs. (2.17), the relationship between $\boldsymbol{E}$ and $\boldsymbol{D}$ is obtained as

$$\boldsymbol{D} = \varepsilon \boldsymbol{E}, \tag{2.28}$$

with ε being constant in this model. However, for analytical reasons that will be expanded upon in a later chapter, the expression of W_{elec} proposed by Gei et al. [70] is introduced, which depends on all the three invariants I_4, I_5, I_6, namely

$$W_{elec} = \frac{1}{2\varepsilon}(\bar{\gamma}_0 I_4 + \bar{\gamma}_1 I_5 + \bar{\gamma}_2 I_6), \tag{2.29}$$

where ε is to be read as the permittivity of the material in the natural configuration and $\bar{\gamma}_i$ $(i = 0, 1, 2)$ are dimensionless constants such that $\sum_i \bar{\gamma}_i = 1$. This expression allows experimental results to be fitted by the use of the dimensionless constants to obtain a more accurate strain energy function. As $\bar{\gamma}_0, \bar{\gamma}_2 \to 0$ (and then $\bar{\gamma}_1 \to 1$), the energy function becomes that of an ideal dielectric eq. (2.27).

2.3 Incremental electro-elasticity

This section introduces the linear incremental deformation theory that allows for the study of the onset of diffuse and localised bifurcation modes, referring to Bertoldi and Gei [31], Dorfmann and Ogden [30] and Ogden [71] for more details.

The way the method works is by superimposing incremental deformations upon a given configuration, shown in figure 2.4. Let B^0 be the initial undeformed configuration. A problem such that an equilibrium configuration is reached where eqs. (2.12) and (2.16) are satisfied with the new deformed configuration denoted as B with the deformation given by $\boldsymbol{\chi}(x^0)$. It is of interest to find solutions near $\boldsymbol{\chi}$ when perturbations are applied to the problem where eqs. (2.12) and (2.16) are still satisfied. Let $\bar{\boldsymbol{\chi}}$ be a solution to the perturbed

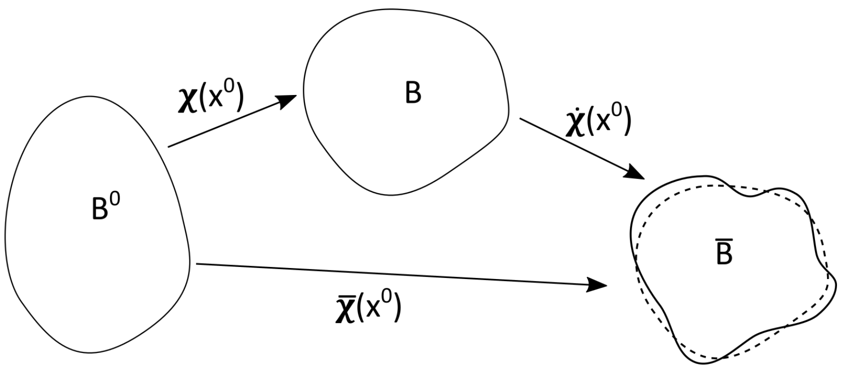

Fig. 2.4 Incremental deformation scheme

problem. The displacement of a material particle due to the perturbations is

$$\dot{\boldsymbol{x}} = \bar{\boldsymbol{x}} - \boldsymbol{x} = \bar{\boldsymbol{\chi}}(\boldsymbol{x}^0) - \boldsymbol{\chi}(\boldsymbol{x}^0) \equiv \dot{\boldsymbol{\chi}}(\boldsymbol{x}^0), \tag{2.30}$$

where when the displacement is small for each x^0, so that higher order terms can be neglected, then $\dot{\boldsymbol{x}}$ is referred to as a linear incremental deformation from the deformed configuration B. The operator $(\,\dot{}\,)$ thus represents the increment in the quantity concerned. The incremental deformation gradient due to the incremental deformation is defined as,

$$\dot{\boldsymbol{F}} = \mathrm{Grad}\dot{\boldsymbol{\chi}}. \tag{2.31}$$

The formulation of the incremental governing equations follows directly from that relative to the finite domain. With the usual assumption of absence volume free charges and body forces left unchanged, the eqs. (2.16) in the incremental framework turn into the following

$$\mathrm{Div}\dot{\boldsymbol{S}} = \boldsymbol{0}, \quad \mathrm{Div}\dot{\boldsymbol{D}}^0 = 0, \quad \mathrm{Curl}\dot{\boldsymbol{E}}^0 = \boldsymbol{0}. \tag{2.32}$$

A perturbation of nominal surface charges and tractions applied on the boundary of B^0, namely $\dot{\omega}^0$ and $\dot{\boldsymbol{t}}^0$, respectively, is considered such that the incremental boundary conditions, following eqs. (2.18), become

$$\llbracket \dot{\boldsymbol{x}}^0 \rrbracket = \boldsymbol{0}, \quad \boldsymbol{n}^0 \cdot \llbracket \dot{\boldsymbol{D}}^0 \rrbracket = -\dot{\omega}^0, \quad \boldsymbol{n}^0 \times \llbracket \dot{\boldsymbol{E}}^0 \rrbracket = \boldsymbol{0}, \quad \llbracket \dot{\boldsymbol{S}} \rrbracket \boldsymbol{n}^0 = \dot{\boldsymbol{t}}^0. \tag{2.33}$$

Assuming that all incremental quantities are small such that second order terms can be ignored, the constitutive eqs. (2.20) can be linearised as,

$$\begin{aligned} \dot{\mathbf{S}} &= \mathbb{C}^0\dot{\mathbf{F}} + \mathbb{B}^0\dot{\mathbf{D}}^0, \quad \dot{S}_{iJ} = C^0_{iJkL}\dot{F}_{kL} + B^0_{iJL}\dot{D}^0_L, \\ \dot{\mathbf{E}}^0 &= \mathbb{B}^{0T}\dot{\mathbf{F}} + \mathbb{A}^0\dot{\mathbf{D}}^0, \quad \dot{E}^0_M = B^0_{iJM}\dot{F}_{iJ} + A^0_{MN}\dot{D}^0_N. \end{aligned} \tag{2.34}$$

In the incompressible case (eqs. (2.22)) $\dot{\boldsymbol{S}}$ is linearised as,

$$\dot{S}_{iJ} = -\dot{p}F^{-1}_{Ji} + pF^{-1}_{Li}\dot{F}_{kL}F^{-1}_{Jk} + C^0_{iJkL}\dot{F}_{kL} + B^0_{iJM}\dot{D}^0_M, \tag{2.35}$$

where $\dot{p}$ is an unknown incremental hydrostatic pressure. The components of the relevant tensor appearing in the previous eqs. are highlighted to facilitate the understanding between the different quantities. The electro-elastic moduli tensors $\mathbb{C}^0$, $\mathbb{B}^0$, $\mathbb{A}^0$ can be expressed in terms of the strain-energy function as

$$C^0_{iJkL} = \frac{\partial^2 W}{\partial F_{iJ}\partial F_{kL}}, \quad B^0_{iJM} = \frac{\partial^2 W}{\partial F_{iJ}\partial D^0_M}, \quad A^0_{MN} = \frac{\partial^2 W}{\partial D^0_M \partial D^0_N}, \tag{2.36}$$

which imply the following symmetries

$$C^0_{iJkL} = C^0_{kLiJ}, \quad A^0_{MN} = A^0_{NM}.$$

The Lagrangian formulation implied by eqs. (2.32) can be turned into an updated Lagrangian one by using push-forward operations based on the new quantities

$$\boldsymbol{\Sigma} = \frac{1}{J}\dot{\boldsymbol{S}}\boldsymbol{F}^T, \quad \hat{\boldsymbol{D}} = \frac{1}{J}\boldsymbol{F}\dot{\boldsymbol{D}}^0, \quad \hat{\boldsymbol{E}} = \boldsymbol{F}^{-T}\dot{\boldsymbol{E}}^0. \tag{2.37}$$

As a consequence, the updated governing equations take the form

$$\mathrm{div}\boldsymbol{\Sigma} = \mathbf{0}, \quad \mathrm{div}\hat{\boldsymbol{D}} = 0, \quad \mathrm{curl}\hat{\boldsymbol{E}} = \mathbf{0}. \tag{2.38}$$

It is convenient to define $\boldsymbol{u}$ as the incremental displacement such that it is a function of $\boldsymbol{x}$ given as $\boldsymbol{u}(\boldsymbol{x}) = \dot{\boldsymbol{x}}$. The corresponding incremental boundary conditions can be derived from the boundary conditions given in eqs. (2.12). In the updated Lagrangian formulation, they are

$$[\![\boldsymbol{u}]\!] = \mathbf{0}, \quad [\![\boldsymbol{\Sigma}]\!]\boldsymbol{n}dA = \dot{\boldsymbol{t}}^0 dA^0, \quad [\![\hat{\boldsymbol{D}}]\!]\cdot\boldsymbol{n}dA = -\dot{\omega}^0 dA^0, \quad \boldsymbol{n}\times[\![\hat{\boldsymbol{E}}]\!] = \mathbf{0}\ . \tag{2.39}$$

The boundary conditions can be specialised, analogously to eqs. (2.13), when the discontinuity is adjacent to a vacuum as follows:

$$\boldsymbol{\Sigma}\boldsymbol{n}dA = \dot{\boldsymbol{t}}^0 dA^0 + \boldsymbol{\Sigma}^*\boldsymbol{n}dA, \quad \hat{\boldsymbol{D}} \cdot \boldsymbol{n}dA = -\dot{\omega}^0 dA^0 + \hat{\boldsymbol{D}}^* \cdot \boldsymbol{n}dA, \tag{2.40}$$

where the incremental quantities in a vacuum are given by

$$\boldsymbol{\Sigma}^* = \dot{\boldsymbol{T}}^* + \boldsymbol{T}^*(\mathrm{tr}[\boldsymbol{L}]\boldsymbol{I} - \boldsymbol{L}^T), \quad \hat{\boldsymbol{D}}^* = \varepsilon_0(\dot{\boldsymbol{E}}^* + (\mathrm{tr}[\boldsymbol{L}]\boldsymbol{I} - \boldsymbol{L})\boldsymbol{E}^*). \tag{2.41}$$

The linearised constitutive equations can be updated through $\boldsymbol{L} = \mathrm{grad}\boldsymbol{u}$, to yield

$$\begin{aligned} \boldsymbol{\Sigma} &= \mathbb{C}\mathbf{L} + \mathbb{B}\hat{\mathbf{D}}, \quad \Sigma_{ir} = C_{irks}L_{ks} + B_{irk}\hat{D}_k, \\ \hat{\mathbf{E}} &= \mathbb{B}^T\mathbf{L} + \mathbb{A}\hat{\mathbf{D}}, \quad \hat{E}_i = B_{kri}L_{kr} + A_{ik}\hat{D}_k. \end{aligned} \tag{2.42}$$

In the incompressible case $\boldsymbol{\Sigma}$ becomes,

$$\Sigma_{ir} = C_{irks}L_{ks} + pL_{ri} - \dot{p}\delta_{ir} + B_{irk}\hat{D}_k,$$

where δ_{ij} is the Kronecker delta and the updated electro-elastic moduli become

$$C_{irks} = \frac{1}{J}C^0_{iJkL}F_{rJ}F_{sL}, \quad B_{irk} = B^0_{iJM}F_{rJ}F^{-1}_{Mk}, \quad JA_{ik} = A^0_{JM}F^{-1}_{Ji}F^{-1}_{Mk}, \tag{2.43}$$

with symmetries applying as before.

Chapter 3

Electro-elastic boundary value problems

In this chapter a variety of elastomer devices are introduced. At first, three elastomer slab devices are described and fundamental path equations for each device are obtained. The third ‘floating’ elastomer device, which is a novel configuration is then analysed in detail to understand its deformation when actuated. In particular the onset of electro-mechanical instability and the so called ‘expansion limit’ is analysed. The ‘floating’ device is then analysed in a tubular configuration, with the problem being posed using a cylindrical coordinate system. Two boundary conditions are introduced, the first with the axial stretch fixed at a constant and the second where it is free and a function of the elastomer tube radius. These two boundary conditions are then analysed to understand how the geometry of the device impacts its deformation. The aim of this study is to obtain a more in depth understanding of the floating elastomer boundary conditions in order to facilitate potential devices using this mode of actuation. The more traditional configurations which are also introduced will be used chapter 4 for the surface instabilities analysis.

3.1 Three electro-elastic problems for a thin planar elastomer

Here three electro-elastic problems are investigated, differing from each other by the type of the imposed electric actuation. Each of these elastomer problems involves a thin slab of elastomer material being actuated through an electric field. The differences lie in the way the electric field is created and the overall configuration of the device. Each device is sketched in Fig. 3.1, which shows the three devices in the deformed configurations. In all cases, the coordinate x_1 singles out the longitudinal axis of the actuator, x_2 is directed across the thickness whereas x_3 is the out-of-plane axis. The material is an ideal dielectric and is assumed to be incompressible. Fringe effects (the non uniform fields on the electrode edges) are ignored, meaning that the elastomer is assumed to be long in comparison to its thickness, typically with a value of $L/d > 10$. The first problem (Fig. 3.1 (a)) is the classical one where two perfectly compliant electrodes are attached to the two opposite sides of the membrane [21]. In the second one, Fig. 3.1 (b), charges are applied directly (typically sprayed) and constrained on the surfaces of the material without the use of electrodes [41], a method that was first studied experimentally by Röntgen in 1880 [20]. The surrounding is assumed to be a vacuum B^*. The third and final problem, Fig. 3.1 (c), consists of the elastomer deforming (and *floating*) in vacuum between two electrodes held at a fixed distance L, as first studied by Diaz-Calleja et al. [42] (the vacuum can be also substituted by an ideal fluid by adjusting the permittivity of the surrounding space). Su et al. [43] also examined the instability of a dielectric slab floating in a conductive fluid undergoing equi-biaxial deformation.

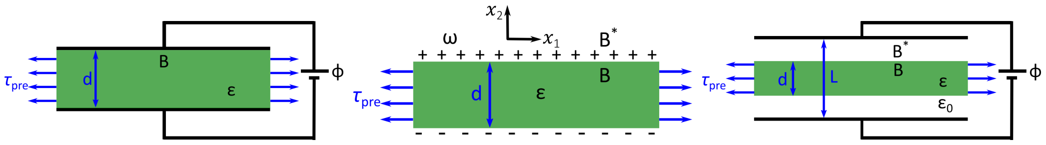

(a) Compliant Electrodes (b) Charge-Controlled (c) ‘Floating’ Elastomer

Fig. 3.1 Diagram of the three electro-elastic devices analysed using various actuation mechanisms. d is the thickness of the deformed elastomer, ε the permittivity of the material, L the distance between electrodes and ε_0 the permittivity of the vacuum. The signs in b) indicate the type of charges applied directly to the surface of the elastomer for the charge-controlled case. A pre-stress τ_{pre} is possibly applied to the elastomer.

In all cases, the elastomer is deformed homogeneously in plane-strain conditions and the material is assumed to be incompressible such that $\lambda_2\lambda_1 = 1$ and $\lambda_3 = 1$, where λ_i are the stretch ratios in the three coordinates $i = \{1, 2, 3\}$. The undeformed and deformed thickness is denoted as d_0 to d respectively, giving the relationship

$$d = \lambda_2 d_0 = \lambda_1^{-1} d_0. \tag{3.1}$$

The electric field has only the transverse component, therefore the electric field vector is given as $\boldsymbol{E} = [0, E_2, 0]$. A relationship between the potential difference Φ across the device and E_2 can be derived from the fact that in piecewise problems, like those addressed here, the latter is the change in voltage over a given distance. In addition, a (current) pre-stress τ_{pre} could be applied on the deformed configuration along axis x_1. The finite electro-elastic actuation laws of the three problems are summarised below for the neo-Hookean strain-energy given by eq. (2.25). It is understood that a similar procedure can be followed for the Gent material eq. (2.26). The elastomer material is assumed to behave as an ideal dielectric and as such the electric part of the strain-energy function is given by eq. (2.27).

3.1.1 Voltage controlled actuation

In the first problem, where the elastomer is sandwiched between compliant electrodes, the electric field outside the electrodes vanishes as the contributions from each electrode cancel each other out. The potential difference across the electrodes is given only by the thickness of the elastomer as

$$\Phi = E_2 d, \tag{3.2}$$

or, in terms of d_0 (eq. (3.1)), and knowing that $D_2 = \varepsilon E_2$ (eq. (2.28)),

$$\Phi = \frac{d_0 D_2}{\varepsilon \lambda_1}. \tag{3.3}$$

Under the assumption of an incompressible neo-Hookean material, the first Piola-Kirchhoff stress is obtained from the strain-energy function using eqs. (2.22). The total stress $\boldsymbol{\tau}$ can then be obtained with the push-forward operation given by eq. (2.15) with the deformation gradient $\boldsymbol{F}$ for plane-strain condition being,

$$\boldsymbol{F} = \begin{pmatrix} \lambda_1 & 0 & 0 \\ 0 & \frac{1}{\lambda_1} & 0 \\ 0 & 0 & 1 \end{pmatrix}. \tag{3.4}$$

The boundary conditions eqs. (2.12) are specialised for the case where no electric field is present on the two outer sides of the film. At first $\tau_{22} = 0$, coming from the jump conditions eq. $(2.12)_3$, is used to solve the pressure term p giving,

$$p = \frac{D_2^2}{\varepsilon} + \frac{\mu}{\lambda_1^2}. \tag{3.5}$$

Then the condition $\tau_{11} = \tau_{pre}$ is employed with the previous pressure term to obtain the variable D_2. We can hence use eq. (3.3) to obtain the relation for Φ

in terms of λ_1 given as

$$\Phi = \frac{d_0\sqrt{\varepsilon^{-1}\left((\lambda_1^4 - 1)\mu - \tau_{pre}\lambda_1^2\right)}}{\lambda_1^2}. \tag{3.6}$$

3.1.2 Charge-controlled actuation

In the second problem, the actuation is controlled by the amount of surface charges, whose nominal density is denoted by $\pm\omega_0$. As previously a neo-Hookean incompressible elastomer slab is used. The boundary conditions eqs. (2.12) are now specialised as previously with the added requirement that eq. $(2.12)_1$, specialises now to $D_2 = \omega$. Following the previous procedure, the pressure term is given by,

$$p = \frac{\omega^2}{\varepsilon} + \frac{\mu}{\lambda_1^2}, \tag{3.7}$$

and a relation for ω in terms of λ_1 is obtained as

$$\omega = \sqrt{\varepsilon\left((\lambda_1^2 - \lambda_1^{-2})\mu - \tau_{pre}\right)}. \tag{3.8}$$

It is worth pointing out that due to the connection between the electric and electric displacement fields, the relationship between Φ and λ_1 for the charge-controlled problem coincides with that of the attached electrodes in eq. (3.6).

3.1.3 ‘Floating’ elastomer in vacuum

In the third problem, where the elastomer is floating between two electrodes at a fixed distance, the potential difference is given by the sum of the contributions from the electric field in the surrounding space and inside the elastomer. In a vacuum where L is the fixed distance between the electrodes and d is the current thickness of the elastomer this becomes,

$$\Phi = E_2^*(L - d) + E_2 d, \tag{3.9}$$

where E_2^* is the only non-vanishing component of the electric field in the vacuum. As the interface between vacuum and elastomer is free from surface charges, from eq. (2.12) we know that $\boldsymbol{D}$ is continuous across this interface and hence $D_2^* = D_2$, revealing that the electric displacement field is constant in the space between electrodes. This leads to the equality $\varepsilon_0 E_2^* = \varepsilon E_2$, which helps to achieve an expression for Φ in terms of E_2 as follows,

$$\Phi = \frac{E_2}{\varepsilon_0}\Big((L-d)\varepsilon + d\varepsilon_0\Big) = \frac{E_2}{\varepsilon_0}\left((L-d_0\lambda_1^{-1})\varepsilon + d_0\lambda_1^{-1}\varepsilon_0\right), \tag{3.10}$$

where d_0 is obtained using eq. (3.1). Equivalently, using the ideal dielectric relationship eq. (2.28), eq. $(3.10)_2$ can be expressed in terms of electric displacement D_2, i.e.

$$\Phi = \frac{D_2}{\varepsilon_0\varepsilon}\left((L-d_0\lambda_1^{-1})\varepsilon + d_0\lambda_1^{-1}\varepsilon_0\right). \tag{3.11}$$

As before, the neo-Hookean strain energy with the assumption of incompressibility is used in eqs. (2.22) and (2.15) to obtain the total stress $\boldsymbol{\tau}$. The boundary conditions are specialised for the case where a vacuum is in the surrounding space and the Maxwell stress is present; This gives the condition that $\tau_{22} = T^*_{22}$, with T^* obtained from eq. (2.9), which is used to solve the pressure term p as,

$$p = D_2^2\Big(\frac{1}{\varepsilon} - \frac{1}{2\varepsilon_0}\Big) + \frac{\mu}{\lambda_1^2}. \tag{3.12}$$

The other boundary condition is $\tau_{11} = \tau_{pre} + T^*_{11}$ which yields the electric displacement field D_2. We can hence obtain the relation for Φ in terms of λ_1 given as

$$\Phi = \frac{(d_0(\varepsilon_0-\varepsilon) + L\varepsilon\lambda_1)\sqrt{(\lambda_1^4-1)\mu - \tau_{pre}\lambda_1^2}}{\lambda_1^2\sqrt{\varepsilon\varepsilon_0^2 - \varepsilon^2\varepsilon_0}}. \tag{3.13}$$

An equation for the electro-mechanical instability can be obtained by setting $d\Phi/d\lambda_1 = 0$. This gives the following polynomial

$$L\varepsilon\lambda_1\mu(1+\lambda_1^4) - d_0(\varepsilon-\varepsilon_0)(\tau_{pre}\lambda_1^2 + 2\mu) = 0, \tag{3.14}$$

where the positive real root corresponds to the onset of electro-mechanical instability.

3.1.4 Analysis of the electro-elastic response of the actuated 'floating' elastomer in vacuum

The first two actuation problems are well known. The plane-strain loading paths for the voltage and charge controlled are plotted in Fig. 3.2 for reference, obtained from eqs. (3.6) and (3.8). The non-dimensional potential difference $\bar{V} = (\Phi/d_0)\sqrt{\varepsilon/\mu}$ and surface charges $\bar{\omega} = \omega/\sqrt{\mu\varepsilon}$ are reported against λ_1. A neo-Hookean strain energy is used and curves show various values of pre-stress with τ_{pre}/μ starting from 0 with increments of 0.5.

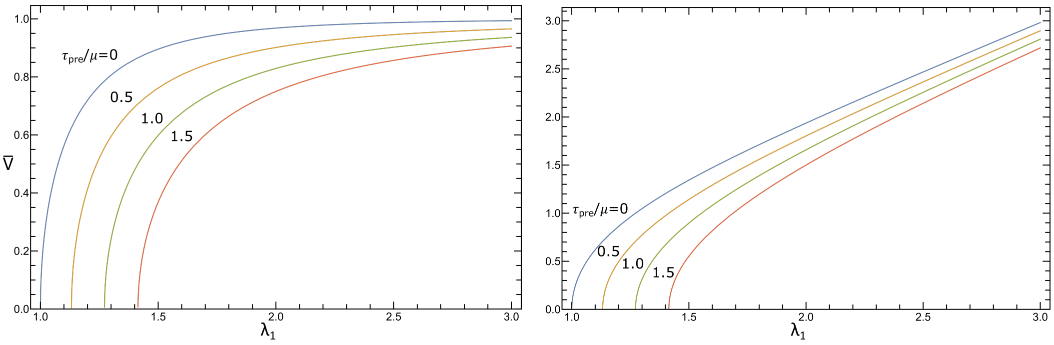

(a) Voltage controlled (b) Charge-controlled

Fig. 3.2 Fundamental loading paths for the voltage controlled and charge-controlled actuation problems, (a) and (b) respectively (neo-Hookean strain energy). λ_1 varies with the non-dimensional electric potential jump $\bar{V}$ (a) and surface charges $\bar{\omega}$ (b). Curves with various pre-stress are shown with τ_{pre}/μ starting from 0 with increments of 0.5

While the fundamental paths for these two described problems are well known, the floating elastomer problem required a deeper analysis which is presented in this section. The problem is specialised here for the case with a surrounding vacuum, however, a fluid could be used by adjusting the permittivity of the vacuum to that of the fluid. The fundamental path of the actuated 'floating' elastomer depends on the geometry of the device in the initial configuration. Therefore, the geometrical ratio d_0/L is defined whereby changing it we can obtain different electro-mechanical loading curves. In general the floating elastomer configuration is novel, as opposed to the charge-controlled and attached compliant electrodes configurations, in that the elastomer contracts longitudinally and expands transversely, attracted towards the fixed electrodes.

Figure 3.3 shows the loading paths for a neo-Hookean strain energy with an incompressible elastomer under no pre-stress, $\tau_{pre} = 0$. In the figure the dimensionless electric potential difference $\bar{V} = (\Phi/L)\sqrt{(\varepsilon/\mu)}$ is reported against the longitudinal stretch λ_1. As the elastomer expands transversely, the elastomer expands more than the distance L between the electrodes. This point will be hereafter called the *expansion limit* and is denoted by black dots on the figure. The black crosses show where electro-mechanical instability triggers which in this problem causes catastrophic thickening of the elastomer. For large values of d_0/L (e.g. 0.9 in the figure), the elastomer does not exhibit electro-mechanical instability before reaching the 'expansion limit'. In contrast,

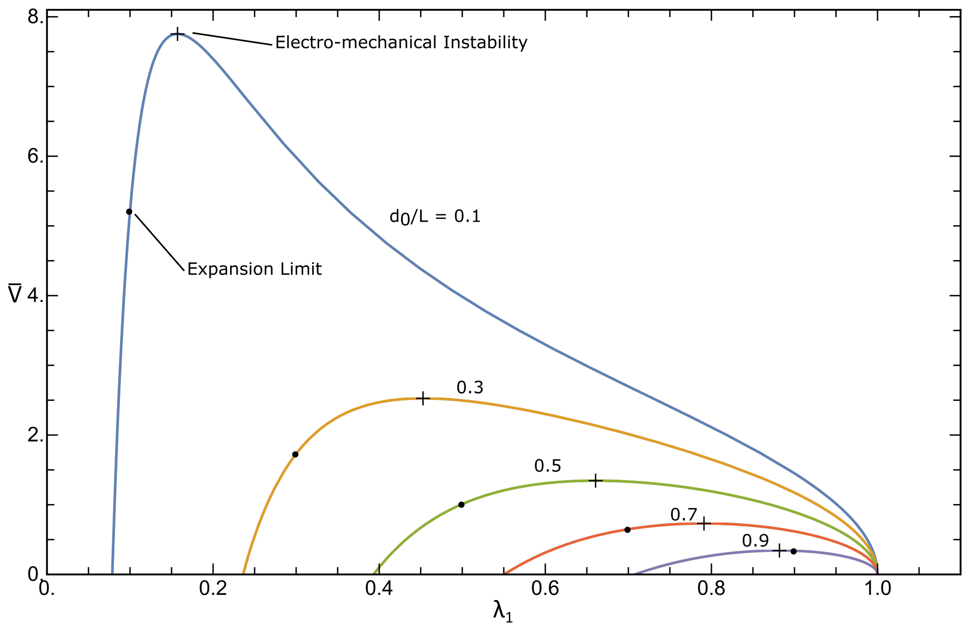

Fig. 3.3 Fundamental loading paths for the actuated ‘floating’ elastomer in vacuum (neo-Hookean strain energy) with no pre-stress (various values of the geometric ratio d_0/L are considered). λ_1 varies with the non-dimensional electric potential jump $\bar{V}$. Dots mark the expansion limit, while crosses indicate the onset of the electro-mechanical instability.

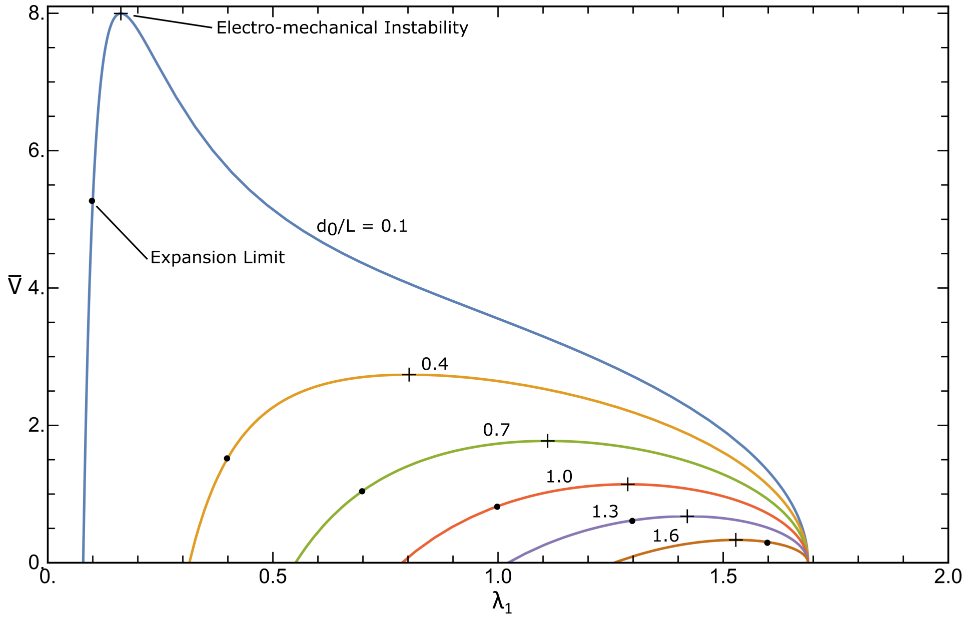

Fig. 3.4 Fundamental loading paths for the actuated ‘floating’ elastomer in vacuum (neo-Hookean strain energy) with non-dimensional pre-stress $\tau_{pre}/\mu = 2.5$ (various values of the geometric ratio d_0/L are considered). λ_1 varies with the non-dimensional electric potential jump $\bar{V}$. Dots mark the expansion limit, while crosses indicate the onset of the electro-mechanical instability.

for $d_0/L \lessapprox 0.8$ the elastomer has enough space to expand and the electro-mechanical instability, analytically predicted by a positive real solution of eq. (3.14), becomes critical. The condition $\Phi = 0$ provides the points where the electro-elastic curve intersects the horizontal axis. Equation (3.11) yields two solutions, namely

$$D_2 = 0, \quad \frac{d}{L} = \frac{\varepsilon/\varepsilon_0}{\varepsilon/\varepsilon_0 - 1}. \tag{3.15}$$

The former is a trivial solution, i.e. null electric actuation; the latter denotes a configuration not physically meaningful, as the left-hand side must be less than one (equal to one at the expansion limit), while the right-hand side has to be greater than one, as any material will always have a permittivity higher than that of the surrounding vacuum.

Figure 3.4 show's the same problem but the elastomer is now experiencing a pre-stress such that $\tau_{pre}/\mu = 2.5$. Using such a setup, an elastomer with a $d_0/L > 1$ is pre-stressed, causing a transversal contraction and allowing the elastomer to be placed between the fixed electrodes. As can be seen, the expansion limit occurs much later along the curve for the same thickness. Where previously the electro-mechanical instability happened past the expansion limit (0.9 in Fig. 3.3), it now occurs before. This causes the peak of the electro-elastic response to appear at larger d_0/L ratios.

Figure 3.5 shows the loading paths using the Gent strain energy for an ideal dielectric material eqs. (2.27) and (2.26). Under plane-strain conditions λ_{lim} is defined from eq. (2.26) as the limiting stretch. In this case I_1^{lim} can be specialised to obtain that

$$\lambda_{lim}^2 + \lambda_{lim}^{-2} - 2 = J_m. \tag{3.16}$$

The adopted Gent parameter was $J_m = 91$, corresponding to $\lambda_{lim} \approx 0.1037$. To note that in literature λ_{lim} is usually calculated in tension which comes out to $1/\lambda_{lim} \approx 9.6$ for the plane-strain problem. This value means that at λ_{lim} the potential difference tends to ∞. Changing the Gent parameter will cause the asymptote to move left or right but keeps the general pattern of the figure the same. In this case, the asymptotic effect is seen for low values of d_0/L, with the transition occurring at $d_0/L \approx 0.13$. Actually, just below that threshold, the electro-mechanical instability becomes less pronounced until it quickly disappears (the curve for $d_0/L = 0.12$ is monotonic). This is caused by the stretch limit preventing further material expansion. As previously mentioned this model is much more accurate in the large stretch range, implying that an

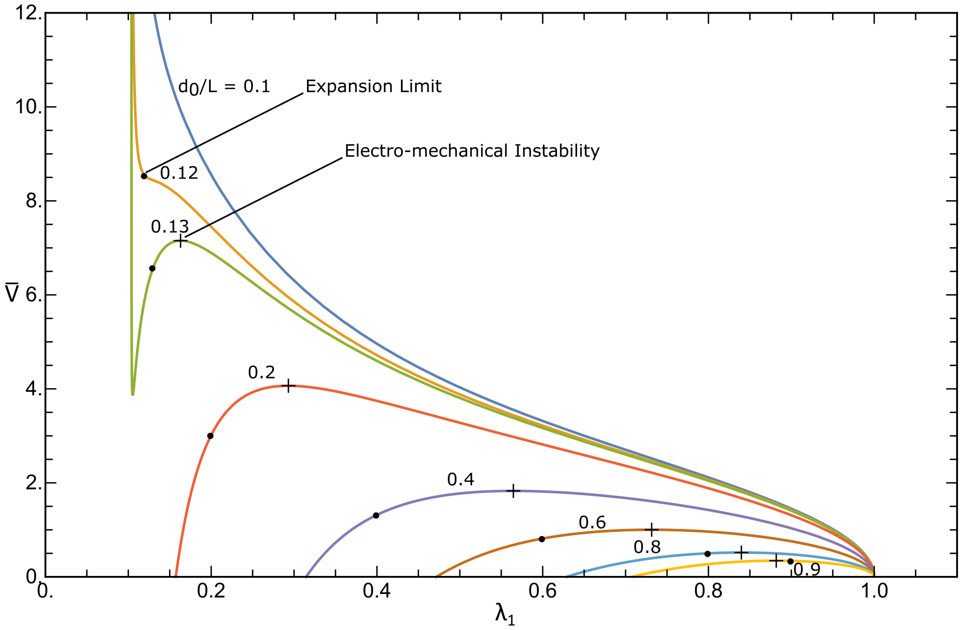

Fig. 3.5 Fundamental loading paths for the actuated ‘floating’ elastomer in vacuum (Gent strain energy with $J_m = 91$, various values of the geometric ratio d_0/L are considered). λ_1 varies with the non-dimensional electric potential jump $\bar{V}$. Dots mark the expansion limit while crosses indicate the onset of the electro-mechanical instability.

elastomer slab could be optimised with its thickness and material properties such that it never experiences and electro-mechanical instability.

Figure 3.6 shows all the fundamental paths starting from the natural configuration for both strain-energy functions and a pre-stressed neo-Hookean function represented on an electric displacement curve. The normalised electric displacement $\bar{D} = D_2/\sqrt{\mu\varepsilon}$ is plotted against λ_1. The electric displacement curve does not depend on the geometry and as such encapsulates all fundamental paths. The black markers represent the expansion limit for each curve. As the d_0/L parameter decreases, a higher electric displacement can be reached before encountering the expansion limit. The Gent curve is steeper as it reaches asymptotically the extension limit of the polymer chains λ_{lim}. It can also be clearly seen how the pre-stress allows higher electric displacement values to be reached at high d_0/L ratios.

3.2 The floating tubular elastomer

In this section the previous floating elastomer slab configuration is considered as a tubular form. The general formulation in polar coordinates will be defined

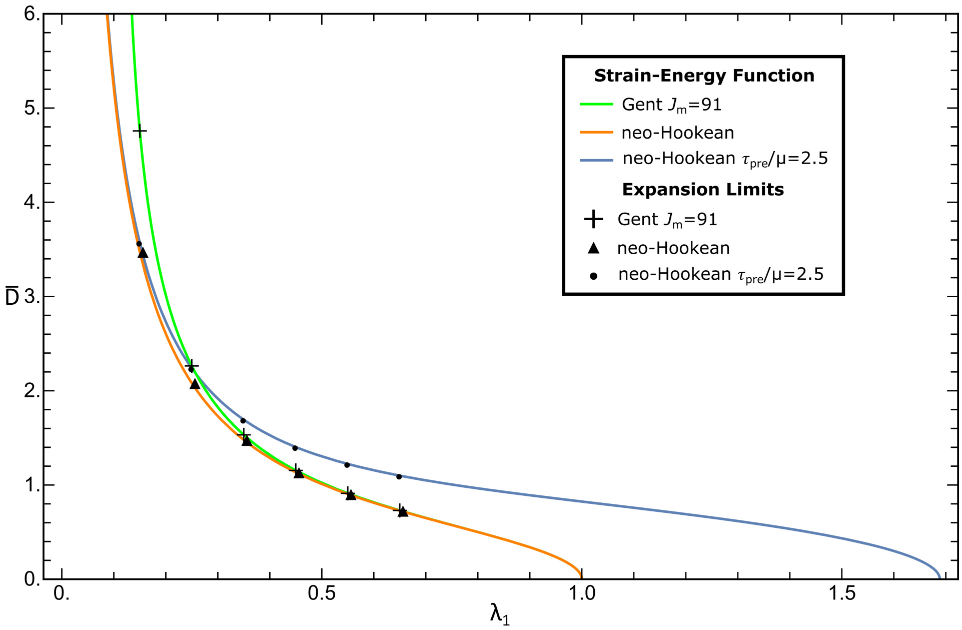

Fig. 3.6 Fundamental loading paths for the actuated 'floating' elastomer in vacuum (for both neo-Hookean and Gent strain energies). λ_1 varies with the non-dimensional electric displacement $\bar{D}$. Black markers mark the expansion limit for each curve; ratio d_0/L is varied from 0.15 to 0.65 in increments of 0.10.

together with the appropriate boundary conditions for the problem. Two cases will be presented with different boundary conditions; The first where the length of the elastomer remains fixed and the second where it is allowed to freely move during actuation. A numerical analysis will then be undertaken to obtain fundamental loading paths for this floating tubular configuration. This will be used to characterise the deformation and to investigate the differences between the two cases.

3.2.1 Configuration of the tubular elastomer

The geometry considered is shown in Fig. 3.7, showing the cross-sectional and top down views of the undeformed B^0 and deformed B configuration. The two electrodes are placed and kept at a fixed distance in space, represented by the radii from the tube centreline a and b. A tubular elastomer is placed inside this gap with the internal and external undeformed radii denoted by c_0 and d_0 and its length L_0. The elastomer is suspended inside a vacuum such that B^{sur} is specialised to B^* with ε_0 representing the permittivity of the vacuum. Due to the implicit symmetry of the tube the problem is solved in radial coordinates, (r, θ, z) with the radial, hoop, and longitudinal stretches being represented as $(\lambda_r, \lambda_\theta, \lambda_z)$. Two different boundary condition cases were solved. The first condition is characterised by the transverse stretch, λ_z, being held constant throughout the deformation such that

$$\lambda_z = \frac{L}{L_0} = k_L, \tag{3.17}$$

where k_L represents the chosen constant. In the second problem, the elastomer is free to deform transversely such that the transverse stretch is a function of the radius,

$$\lambda_z(r) = \frac{L(r)}{L_0}, \tag{3.18}$$

where the radius r is bounded by the inner and outer boundary of the elastomer c and d. In both cases the initial configuration is assumed to have a constant length with the radius. The elastomer is taken to be incompressible so that the volume remains constant, i.e. $\lambda_r\lambda_\theta\lambda_z = 1$.

3.2.2 Electro-mechanics of the system

Using the continuity of volume of the elastomer tube, from the assumption of incompressibility, a volume of a shell bounded by the radius c_0 and an arbitrary radius r_0 in the undeformed configuration is given in the deformed state c and r as,

$$(r_0^2 - c_0^2) = \lambda_z(r^2 - c^2), \tag{3.19}$$

with c_0 being a fixed quantity once the elastomer tube is fabricated. Using this condition over the whole volume of the tubular elastomer, a geometrical expression for the outer radius d in the deformed configuration with respect to the undeformed radii and the transversal stretch is given as,

$$d = \sqrt{c^2 + (d_0^2 - c_0^2)\lambda_z^{-1}}. \tag{3.20}$$

The hoop (tangential) stretch is defined as $\lambda_\theta = r/R$. Using eq. (3.19) a relation for the hoop stretch in terms of r is obtained,

$$\lambda_\theta(r) = \frac{r}{\sqrt{c_0^2 + (r^2 - c^2)\lambda_z}} \tag{3.21}$$

It is also important to note that due to incompressibility the radial stretch can be given by the other two stretches as $\lambda_r = (\lambda_z\lambda_\theta)^{-1}$ and using the previous

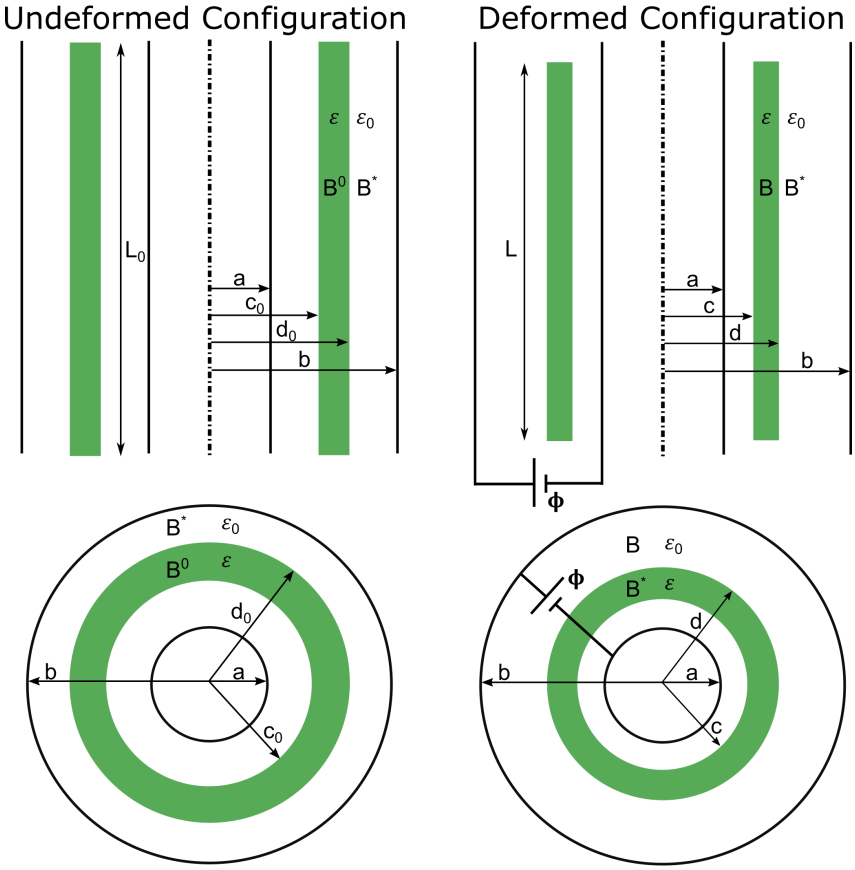

Fig. 3.7 Diagram of dross-section and top down views of a floating elastomer slab with a tubular shape, with the undeformed and deformed configuration on the left and right respectively. The letters a b c and d are the various radii from the centreline of the tube with L being the length in the deformed configuration. The permittivity of the elastomer and vacuum is given by ε and ε_0 respectively.

equation is obtained as,

$$\lambda_r(r) = \frac{\sqrt{c_0^2 + (r^2 - c^2)\lambda_z}}{r\lambda_z}. \tag{3.22}$$

In the deformed configuration, the equilibrium of the elastomer is governed, in terms of the total stress $\boldsymbol{\tau}$, by the differential equation,

$$\frac{d\tau_r}{dr} + \frac{\tau_r - \tau_\theta}{r} = 0 \tag{3.23}$$

where $\tau_r, \tau_\theta, \tau_z$ are the stress components in the three radial coordinates.

The actuation of the elastomer is induced by applying a potential difference, Φ, across the electrodes, as shown in the deformed configuration of Fig. 3.7. This causes an electric field to exist only in the radial direction and be a function of the radius such that the electric field vector is given as $\boldsymbol{E} = [E_r(r), 0, 0]$. The radial component can be obtained using the expression

$$E_r(r) = -\mathrm{d}\Phi/\mathrm{d}r. \tag{3.24}$$

It is, however, easier to work in terms of the electric displacement $\boldsymbol{D}$, because as seen in the jump conditions eqs. (2.12), the electric displacement is continuous through a jump. The application of Gauss' law at the inner electrode $(r = a)$ gives a relation between the electric displacement and the amount of charge ω stored on the electrode,

$$D_r(a) = \frac{\omega}{2\pi a L}. \tag{3.25}$$

Gauss' law also gives that the electric displacement at a radius r is given by $D_r(r) = D_r(a)a/r$. This can be used, with the assumption of an ideal dielectric, to obtain a relationship between the electric displacement and electric field at a given radius as,

$$\begin{aligned} \varepsilon_0 k E_r(a) &= D_r(a), \\ \varepsilon_0 k E_r(r) &= \frac{D_r(a)a}{r} = \frac{\omega}{2\pi r L}, \end{aligned} \tag{3.26}$$

where k is the permittivity constant of the medium at the radius, with $k = 1$ in a vacuum. The total potential difference applied to the electrodes is given as $\Phi = \phi(b) - \phi(a)$. Using eqs. (3.24) and (3.26) the various components of Φ in the device can be integrated and then added together to obtain a relation between the potential difference and the electric displacement,

$$\begin{aligned} \Phi_1 = \phi(c) - \phi(a) &= \int_a^c D_r(a)\frac{a}{r}\frac{1}{\epsilon_0}dr = D_r(a)\frac{a}{\epsilon_0}\ln(\frac{c}{a}), \\ \Phi_2 = \phi(b) - \phi(d) &= \int_d^b D_r(a)\frac{a}{r}\frac{1}{\epsilon_0}dr = D_r(a)\frac{a}{\epsilon_0}\ln(\frac{b}{d}), \\ \Phi_3 = \phi(d) - \phi(c) &= \int_c^d D_r(a)\frac{a}{r}\frac{1}{\epsilon_0 k_s}dr = D_r(a)\frac{a}{\epsilon_0 k_s}\ln(\frac{d}{c}), \\ \Phi = \Phi_1 + \Phi_2 + \Phi_3 &= D_r(a)\frac{a}{\epsilon_0}\left[\ln(\frac{c}{a}) + \ln(\frac{b}{d})\right] + D_r(a)\frac{a}{\epsilon_0 k_s}\ln(\frac{d}{c}), \end{aligned} \tag{3.27}$$

with k_s being specialised as the permittivity constant of the elastomer material used in the device such that $\varepsilon_0 k_s = \varepsilon$. The electric field in the dielectric material is defined as,

$$E_r(r) = D_r(a)\frac{a}{r\varepsilon}, \quad (c < r < d) \tag{3.28}$$

which when used in the previous equation allows us to obtain a relation between the electric field inside the elastomer and the applied potential difference as,

$$\begin{aligned} \Phi &= E_r(r)r\Big[\frac{\varepsilon}{\varepsilon_0}\ln(\frac{cb}{ad}) + \ln(\frac{d}{c})\Big] \\ E_r(r) &= \frac{\Phi\varepsilon_0}{r\Big[\varepsilon\ln(\frac{cb}{ad}) + \varepsilon_0\ln(\frac{d}{c})\Big]}. \end{aligned} \tag{3.29}$$

As in the previous three devices, a simple neo-Hookean material is chosen, with the assumption of incompressibility and an ideal dielectric such that the strain energy function $W(\boldsymbol{F}, \boldsymbol{D}^0)$ of the material is given by eqs. (2.25) and (2.27). The total stress $\boldsymbol{\tau}$ can then be obtained with the push-forward operation following eq. $(2.15)_2$ with the deformation gradient $\boldsymbol{F}$ in radial coordinates given as,

$$\boldsymbol{F} = \begin{pmatrix} \lambda_r & 0 & 0 \\ 0 & \lambda_\theta & 0 \\ 0 & 0 & \lambda_z \end{pmatrix}. \tag{3.30}$$

We can thus obtain $\tau_\theta - \tau_r$ and $\tau_z - \tau_r$ as follows,

$$\begin{aligned} \tau_\theta - \tau_r &= \lambda_\theta\frac{\partial W}{\partial\lambda_\theta} - \lambda_r\frac{\partial W}{\partial\lambda_r} - \frac{D_r^2}{\varepsilon}, \\ &= \mu(\lambda_\theta^2 - \lambda_\theta^{-2}\lambda_z^{-2}) - \varepsilon E_r^2, \end{aligned} \tag{3.31}$$

$$\begin{aligned} \tau_z - \tau_r &= \lambda_z\frac{\partial W}{\partial\lambda_z} - \lambda_r\frac{\partial W}{\partial\lambda_r} - \frac{D_r^2}{\varepsilon}, \\ &= \mu(\lambda_z^2 - \lambda_\theta^{-2}\lambda_z^{-2}) - \varepsilon E_r^2. \end{aligned} \tag{3.32}$$

The eqs. (3.23), (3.31) and (3.32) make up a differential-algebraic system of equations (DAE) which can be solved for a given potential difference Φ instead of the electric field using eq. (3.29). The problem is non-linear but solutions are studied for increasing Φ starting from the natural configuration.

3.2.3 Boundary conditions of the problem

The specification of the boundary conditions is needed in order to solve the DAE for the two previously mentioned cases. Similar to the floating elastomer slab device the electric field outside of the material is not null, and Maxwell's stress needs to be taken into account as it acts upon the elastomer. Under the assumption of a surrounding vacuum, the Maxwell stress tensor can be obtained using eq. (2.9). Using the expression from the jump conditions, $\varepsilon_0\boldsymbol{E}^* = \varepsilon\boldsymbol{E}$, the Maxwell stress tensor is given in radial co-ordinates as,

$$\boldsymbol{T}^* = \begin{pmatrix} \frac{(\varepsilon E_r(r))^2}{2\varepsilon_0} & 0 & 0 \\ 0 & -\frac{(\varepsilon E_r(r))^2}{2\varepsilon_0} & 0 \\ 0 & 0 & -\frac{(\varepsilon E_r(r))^2}{2\varepsilon_0} \end{pmatrix}. \tag{3.33}$$

The two cases of interest are when λ_z is held constant throughout the deformation and when the elastomer is free to deform and $\lambda_z(r)$ becomes a function of the radius.

Case with λ_z constant

In the first case the elastomer tube is stretched transversely and held throughout the deformation such that λ_z becomes a constant geometrical parameter of the problem. The hoop stretch $\lambda_\theta(r)$ is obtained from eq. (3.21) with the only unknown being the internal deformed radius c. The potential difference applied across the electrodes is fixed with eq. (3.29) giving the appropriate electric field and eq. (3.20) allowing the unknown deformed outer radius d to be expressed in terms of the unknown c. The Maxwell boundary conditions at both boundaries of the deformed elastomer need to be satisfied such that

$$\tau_r(c) = \frac{(\varepsilon E_r(c))^2}{2\varepsilon_0}, \quad \tau_r(d) = \frac{(\varepsilon E_r(d))^2}{2\varepsilon_0}. \tag{3.34}$$

Together with the continuity of volume due to the incompressibility of the material, $(d_0^2 - c_0^2) = \lambda_z(d^2 - c^2)$, the DAE is able to be solved for the fixed λ_z case.

Case with $\lambda_z(r)$ as a function of the radius

In the second case the elastomer is allowed to deform freely such that $\lambda_z(r)$ becomes a function of the radius. This gives a new unknown to be solved in the DAE and as such a new equation is needed. The procedure remains similar to the previous case, however, in eqs. (3.21) and (3.20) $\lambda_z(r)$ becomes another unknown. The new equation will be given by the Maxwell boundary conditions in the transversal direction, such that

$$\tau_z = -\frac{(\varepsilon E_r(r))^2}{2\varepsilon_0}. \tag{3.35}$$

Using this condition in eq. (3.32) the missing equation of the DAE to solve the function $\lambda_z(r)$ is obtained as,

$$\frac{-(\varepsilon E_r(r))^2}{2\varepsilon_0} = \mu\left(\lambda_z(r)^2 - \lambda_\theta(r)^{-2}\lambda_z(r)^{-2}\right) - \varepsilon E_r(r)^2 + \tau_r. \tag{3.36}$$

To check the continuity of volume due to the incompressibility condition, $\lambda_z(r)$ must be integrated over the radial thickness of the deformed elastomer tube such that,

$$(c_0^2 - d_0^2) = 2\int_c^d \lambda_z(r) r \mathrm{d}r. \tag{3.37}$$

3.2.4 Analysis of the electro-elastic response of the actuated 'floating' tubular elastomer in vacuum

To solve the DAE an iterative approach is used, in both cases, to make sure the boundary conditions are met, detailed in Appendix A. The results of this numerical analysis are shown, to better understand the fundamental path of the actuated floating elastomer tube. When the elastomer tube is actuated it deforms towards the inner electrode a. All plotted curves show the elastomer actuated until it deforms up to the inner electrode ($c = a$), hereafter called the *contraction limit.*

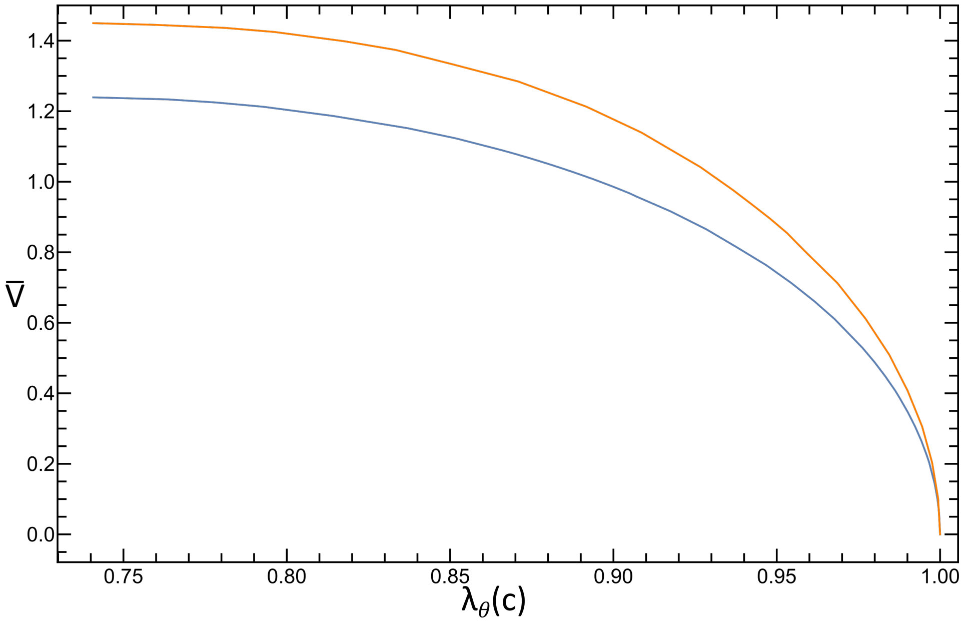

Fig. 3.8 Fundamental loading paths for the actuated 'floating' elastomer tube in vacuum (neo-Hookean strain energy). $\lambda_\theta(c)$ varies with the dimensionless voltage $\bar{V}$. Blue and orange curves show the solutions with a fixed $\lambda_z = 1$, and when $\lambda_z(r)$ is a function of the radius respectively.

Figure 3.8 shows the same elastomer with the two different solutions with a fixed $\lambda_z = 1$ in blue and a varying $\lambda_z(r)$ in orange. The dimensionless electric potential $\bar{V} = (\Phi/(b-a))\sqrt{\varepsilon/\mu}$ is reported against the angular stretch at the inner elastomer radius $\lambda_\theta(c)$. This corresponds to the dimensionless inner radius as $\lambda_\theta(c) = c/c_0$. When the elastomer is constrained with a constant λ_z larger radial deformations can be achieved with the same voltage. When the elastomer deforms freely it also contracts transversely which causes these higher voltages for the same radial deformation.

Figure 3.9 shows two solutions with a fixed $\lambda_z = 1$ and $\lambda_z = 1.5$ in blue and orange respectively. Again the dimensionless electric potential $\bar{V}$ is plotted against the angular stretch at the inner elastomer radius $\lambda_\theta(c)$. The orange curve starts at a lower value $\lambda_\theta(c)$ due to the stretch caused by the higher fixed λ_z value causing the elastomer tube to thin and contract. Overall the elastomer tube with the higher longitudinal stretch experiences bigger contractions when actuated with the same voltage, however, reaches the contraction limit sooner. This is caused by a combination of the elastomer being closer to the inner electrode, and as such experiencing a greater attraction force and the elastomer being thinner. For both of these boundary conditions the elastomer reaches the contraction limit, before the onset of electro-mechanical instability.

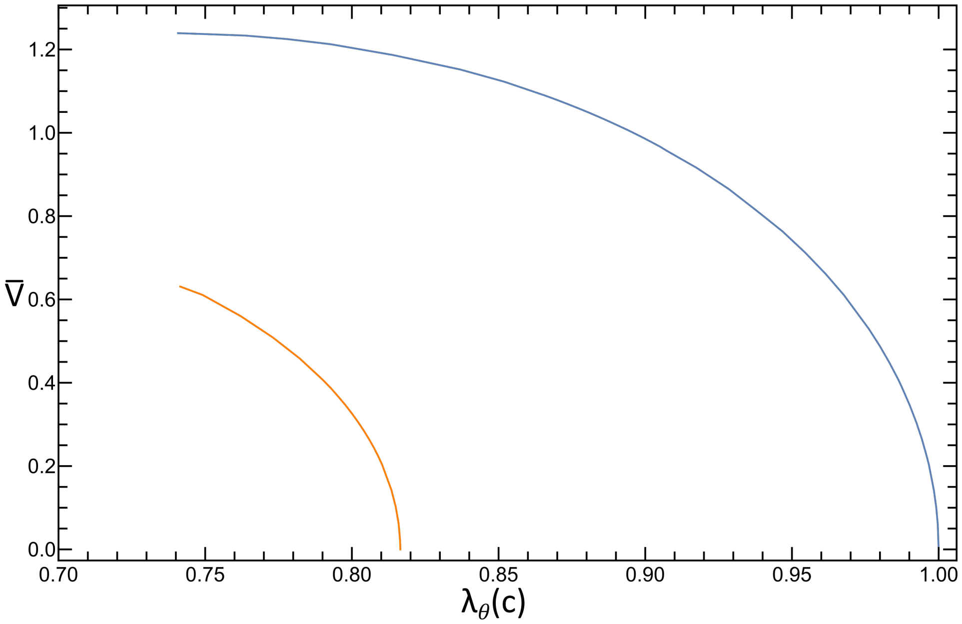

Fig. 3.9 Fundamental loading paths for the actuated ‘floating’ elastomer tube in vacuum (neo-Hookean strain energy). $\lambda_\theta(c)$ varies with the dimensionless voltage $\bar{V}$. Blue and orange curves show the solutions when λ_z is fixed at 1 and 1.5 respectively.

Figure 3.10 shows λ_z at mid radius against the dimensionless potential difference $\bar{V}$ in the case where the longitudinal stretch is not fixed. The geometrical parameters are non-dimensionalised using the inner radius a, such that $\bar{r} = r/a$. Various geometries are considered using the geometrical ratio $\bar{c}_0$, meaning the higher the ratio the further away the undeformed elastomer is from the inner electrode. The same elastomer thickness is used in all three cases. The onset of electro-mechanical instability is seen for the first time in the case with $\bar{c}_0 = 1.6$. The onset appears in this case because the elastomer tube starts with the largest radius from the inner electrode c_0. It is thus able to undergo larger deformations before reaching the contraction limit, causing the onset of electro-mechanical instability to appear which snaps the elastomer into the inner electrode. Overall when λ_z is free, the elastomer shortens when it is actuated, with bigger contractions for the same voltage when $\bar{c}_0$ is lower. This again is caused by the elastomer starting closer to the inner electrode. However, when the ratio is increased, the elastomer is able to achieve bigger overall deformations as it has more room to deform before reaching the contraction limit.

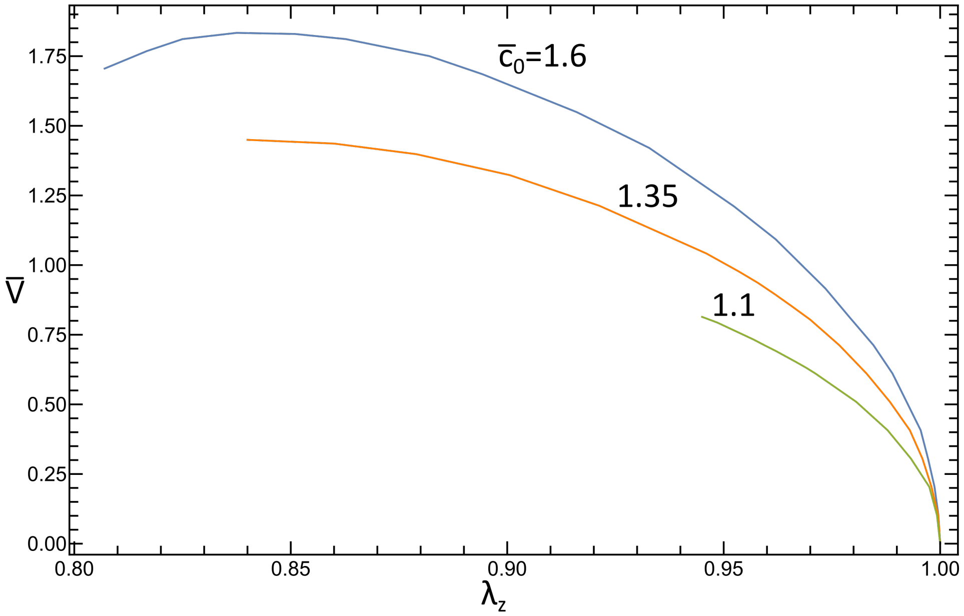

Fig. 3.10 Fundamental loading paths for the actuated ‘floating’ elastomer tube in vacuum (neo-Hookean strain energy). $\lambda_z(r)$ at mid radius is plotted with the dimensionless voltage $\bar{V}$. Various values of the geometric ratio $\bar{c}_0$ are considered with the same elastomer thickness.

In Fig. 3.11 the previous case with $\bar{c}_0 = 1.6$ is taken to examine $\lambda_\theta(r)$ and $\lambda_z(r)$ throughout the loading path and in particular as the onset of electro-mechanical instability is reached. The analysed geometry is defined by the parameters $\bar{c}_0 = 1.6$, $\bar{d}_0 = 1.9$, and $\bar{b} = 2$. Figure 3.11 (a) shows the elastomer tube actuated with $\bar{V} = 0.61$, showing the deformation type in the initial phase of the fundamental path. Up until this potential difference the thickness of the elastomer tube remains almost unchanged to the undeformed configuration ($\bar{d}_0 - \bar{c}_0 = 0.3$) and the two stretches show a homogeneous deformation. The stretches are small and the curves both have a positive gradient showing how the stretches are larger the closer you get to the inner electrode. As the potential difference is increased further, $\bar{V} = 1.42$ in Fig. 3.11 (b), λ_θ starts to deviate from λ_z caused by the elastomer thickening. As the electro-mechanical instability onset is reached (Fig. 3.11 (c)) the elastomer thickens and contracts at faster rates until the snap-through instability forces the tube to contract against the inner electrode (Fig. 3.11 (d)).

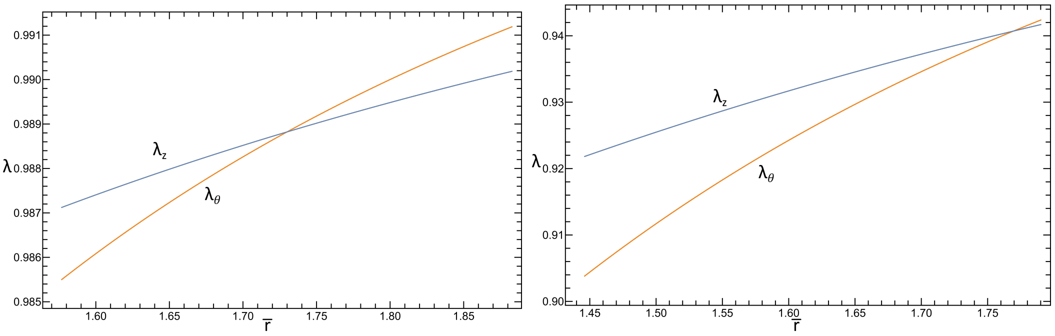

(a) $\bar{V}$ of 0.61 (b) $\bar{V}$ of 1.42

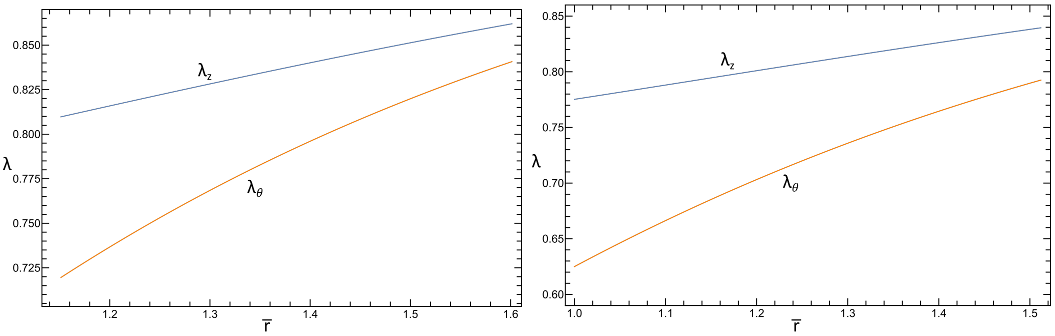

(c) $\bar{V}$ of 1.83 (d) $\bar{V}$ of 1.71

Fig. 3.11 Fundamental loading paths for the actuated 'floating' elastomer tube in vacuum ($\bar{c}_0 = 1.6$). The stretches $\lambda_z(r)$ and $\lambda_\theta(r)$ are displayed as they vary throughout the thickness at different dimensionless voltage $\bar{V}$. Note that the scales of the vertical axes of the four panels are not comparable.

Chapter 4

Electro-elastic surface instabilities

In this chapter, the incremental theory introduced in section 2.3 is specialised to identify electro-elastic surface instabilities on a pre-stressed elastomer half-space under plane-strain conditions. These instabilities, called surface instabilities in the case of a half-space, may be detected by investigating the propagation of perturbations of an arbitrary wavelength superimposed on the current state of deformation. Incremental boundary conditions are introduced suitable for the three electro-elastic problems using a thin planar elastomer introduced in section 3.1. The numerical results, highlighting the onset of surface instabilities for the three cases are then discussed. The theory is further enriched by introducing the surface-coating theory, to take into account the effect of the stiffness of the electrode on the surface instability of a substrate, following the path described in section 3.1.1. The of this work is to achieve a deeper understanding of the operating regime of these dielectric elastomer devices. Surface instability provides a good starting point to understand the range where the device will fail as it is obtained from the limit as the wavelength tends to infinity. The analysis of electrode stiffness effects is also meant to understand the domain in which the assumption of compliant electrode is valid.

4.1 Governing Equations

The electro-elastic modelling framework is specialised to seek bifurcation with a possible presence of an external electric field normal to its boundary. The substrate, as previously introduced and shown in figure 4.1, is possibly pre-stressed along the x_1 direction ($\tau_{pre} \neq 0$) and is subjected to a plane incremental

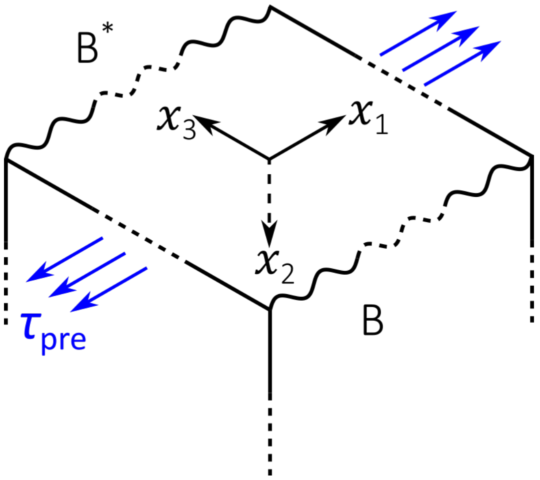

Fig. 4.1 Diagram showing surface instabilities on a pre-stressed elastomer half-space subjected to a plane incremental deformation ($u_3 = 0$).

deformation. In turn, this means that the out-of-plane component of the displacement is null, i.e. $u_3 = 0$, and $\boldsymbol{u}$ depends only on coordinates x_1 and x_2, i.e. $u_i = u_i(x_1, x_2)$ $(i = 1, 2)$. Similarly, it is also assumed that $\hat{D}_3 = 0$, $\hat{D}_i = \hat{D}_i(x_1, x_2)$ $(i = 1, 2)$ and $\dot{p} = \dot{p}(x_1, x_2)$. By adopting the updated Lagrangian formulation, the governing eqs. (2.38) can be written in component form as

$$\begin{aligned} \Sigma_{11,1} + \Sigma_{12,2} = 0, \qquad \Sigma_{21,1} + \Sigma_{22,2} = 0, \\ \hat{D}_{1,1} + \hat{D}_{2,2} = 0, \qquad \hat{E}_{1,2} - \hat{E}_{2,1} = 0, \end{aligned} \tag{4.1}$$

where a comma represents partial differentiation. Field eqs. (4.1) are satisfied by a small amplitude solution of the form (the domain is the half-space $x_2 \geq 0$)

$$\begin{aligned} u_i(x_1, x_2) &= v_i(x_2)\text{exp}(ikx_1), \\ \hat{D}_i(x_1, x_2) &= \Delta_i(x_2)\text{exp}(ikx_1), \\ \dot{p}(x_1, x_2) &= q(x_2)\text{exp}(ikx_1), \end{aligned} \tag{4.2}$$

with k being the wave-number of the perturbation. It is expected that the electro-elastic surface instability is independent of k. The incompressibility constraint $u_{1,1} + u_{2,2} = 0$ imposes to eqs. (4.2) that

$$ikv_1(x_2) + v_2'(x_2) = 0; \tag{4.3}$$

similarly, eq. $(4.1)_3$ dictates

$$ik\Delta_1(x_2) + \Delta_2'(x_2) = 0. \tag{4.4}$$

Bifurcation modes must decay deep in the half-space, as $x_2 \to \infty$, therefore an admissible general form of v_2, Δ_2 and q is

$$\begin{aligned} v_2(x_2) &= U\exp(skx_2), \\ \Delta_2(x_2) &= W\exp(skx_2), \\ q(x_2) &= Q\exp(skx_2), \end{aligned} \tag{4.5}$$

where $s < 0$ to ensure that displacement decays away from the boundary as x_2 increases. Then using eqs. (4.3), (4.4), eqs. (4.5) become

$$\begin{aligned} v_1(x_2) &= iUs\exp(sk_1x_2), \\ \Delta_1(x_2) &= iWs\exp(sk_1x_2). \end{aligned} \tag{4.6}$$

By substituting these into eqs. (4.1), a system of equations for the three unknowns U, W and Q is obtained. A non-trivial solution requires that the determinant of the coefficients vanishes, leading to a polynomial equation (of the 6th order) in s. However, the only admissible solutions are the three negative roots of s, namely $s_j < 0$ $(j = 1, 2, 3)$. Therefore, the general expressions for the bifurcation fields are

$$\begin{aligned} v_2(x_2) &= \sum_{j=1}^{3} U_j\exp(s_jkx_2), \\ \Delta_2(x_2) &= \sum_{j=1}^{3} W_j\exp(s_jkx_2), \\ q(x_2) &= \sum_{j=1}^{3} Q_j\exp(s_jkx_2). \end{aligned} \tag{4.7}$$

The coefficients appearing in (4.7) are not independent and eqs. (4.2) can be employed to find their connection. In particular, Q_j and W_j can be expressed in terms of U_j $(j = 1, 2, 3)$.

Incremental equations in vacuum. In some of the analysed problems, it is mandatory to deal with the external incremental fields in vacuum B^*, where Maxwell's equations hold for $\boldsymbol{D}^*$ and $\boldsymbol{E}^*$. In those cases, there exists an electric potential $\phi^*(x_1, x_2)$, such that

$$\begin{aligned} &\dot{E}^*_1 = -\phi^*_{,1}, \quad \dot{E}^*_2 = -\phi^*_{,2}, \quad \dot{E}^*_3 = 0, \\ &\dot{D}^*_1 = -\varepsilon_0\phi^*_{,1}, \quad \dot{D}^*_2 = -\varepsilon_0\phi^*_{,2}, \quad \dot{D}^*_3 = 0, \end{aligned} \tag{4.8}$$

which satisfies the Laplace's equation

$$\phi^*_{,11} + \phi^*_{,22} = 0, \tag{4.9}$$

as $\mathrm{div}\boldsymbol{D}^* = 0$. A solution compatible with the decaying of effects as $x_2 \to -\infty$ is

$$\phi^*(x_1, x_2) = \phi_c \exp(kx_2)\exp(ikx_1), \tag{4.10}$$

where ϕ_c is the amplitude. It may be useful to recall that, as a function of ϕ^*, the incremental Maxwell stress tensor has the following non-zero components

$$\begin{aligned} &\dot{T}^*_{11} = \dot{T}^*_{33} = -\dot{T}^*_{22} = \varepsilon_0 E^*_2 \phi^*_{,2}, \\ &\dot{T}^*_{12} = \dot{T}^*_{21} = -\varepsilon_0 E^*_2 \phi^*_{,1}. \end{aligned} \tag{4.11}$$

Incremental boundary conditions and bifurcation equation. The incremental boundary conditions specialised for a discontinuity between the elastomer surface and an adjacent vacuum are recalled from eqs. (2.40) and (2.41). For relevant practical applications, both the surface tractions and the surface charges are independent of deformation and as such $\dot{\boldsymbol{t}}^0 = \mathbf{0}$ and $\dot{\omega}^0 = 0$. On $x_2 = 0$, eq. $(2.41)_1$ reduces to the following scalar equations

$$\begin{aligned} &\Sigma_{21} + T^*_{11} u_{2,1} + T^*_{21} u_{2,2} - \dot{T}^*_{21} = 0, \\ &\Sigma_{22} + T^*_{22} u_{2,2} + T^*_{21} u_{2,1} - \dot{T}^*_{22} = 0. \end{aligned} \tag{4.12}$$

Similarly, for eq. $(2.41)_2$ on $x_2 = 0$, it turns out

$$\begin{aligned} &\hat{D}_2 + D^*_1 u_{2,1} + D^*_2 u_{2,2} - \dot{D}^*_2 = 0, \\ &\hat{E}_1 - E^*_1 u_{1,1} - E^*_2 u_{2,1} - \dot{E}^*_1 = 0. \end{aligned} \tag{4.13}$$

This provides a system of four homogeneous equations. For a non-trivial solution of the bifurcation problem, the determinant of the coefficients U_j ($j = 1, 2, 3$) and ϕ_c must vanish yielding the *bifurcation equation.* It is worth mentioning that an alternative way to study bifurcation is to use the fields (4.7), (4.2) and (4.10) into the integral formulation obtained by Gei et al. [70]

and applied by Siboni et al. [72]. The fields can also be adapted to be used in the Stroh formulation [73].

Specialised boundary conditions for the three electro-elastic problems. The general theory is adapted to the three fundamental loading paths for an elastomer slab, introduced in section 3.1, to study the onset of surface instabilities for each type of actuation. To solve the incremental equation system, eqs. (4.12) and (4.13), boundary conditions need to be specified for the three cases. Just as a reminder, for all three configurations the electric actuation is assumed along the thickness of the elastomer, therefore

$$D_1^* = E_1^* = 0, \quad D_1 = E_1 = 0. \tag{4.14}$$

The elastomer may be subjected to a (current) pre-stress τ_{pre} along x_1. As such, the stress boundary conditions (2.7) specialise in

$$\tau_{22} = T_{22}^*, \quad \tau_{pre} = \tau_{11} - T_{11}^*. \tag{4.15}$$

In both the non floating cases detailed in section 3.1.1 and 3.1.2, there is no external electric field, namely

$$D_2^* = E_2^* = 0 \tag{4.16}$$

and, as a consequence, the Maxwell stress tensor vanishes, $\boldsymbol{T}^* = \boldsymbol{0}$. Conversely, for the elastomer 'floating' between electrodes (section 3.1.3), its components are obtained from eq. (2.9) and are given as follows,

$$\boldsymbol{T}^* = \begin{pmatrix} -\frac{(\varepsilon_0 E_1^*)^2}{2\varepsilon_0} & 0 \\ 0 & \frac{(\varepsilon_0 E_2^*)^2}{2\varepsilon_0} \end{pmatrix} = \begin{pmatrix} -\frac{(D_1^*)^2}{2\varepsilon_0} & 0 \\ 0 & \frac{(D_2^*)^2}{2\varepsilon_0} \end{pmatrix}. \tag{4.17}$$

Only two components are shown, as the problem at hand is a two-dimensional plane-strain case where the elastomer remains undeformed out-of-plane. The incremental boundary conditions may also be specialised to the three configurations. Likewise the finite-strain counterparts, for attached compliant electrodes and charged-controlled configurations, the incremental Maxwell stress tensor is null, $\dot{\boldsymbol{T}}^* = \boldsymbol{0}$. However, in the former case there are no fields in the vacuum and there the incremental electric field is also null, $\dot{D}_2^* = \dot{E}_2^* = 0$, differently from charge-controlled actuation where the charges are constrained on the surface of the substrate causing incremental fields to exist in the adjacent vacuum. The incremental boundary conditions are summarised in Table 4.1.

Table 4.1 Summary of incremental boundary conditions for the three elastomer slab devices

Device	D_2^*, E_2^*	$\dot{D}_2^*$, $\dot{E}_2^*$	$\boldsymbol{T}^*$	$\dot{\boldsymbol{T}}^*$
Compliant electrodes	$\varnothing$	$\varnothing$	$\varnothing$	$\varnothing$
Charge controlled	$\varnothing$	$\dot{D}_2^*$, $\dot{E}_2^*$	$\varnothing$	$\varnothing$
‘Floating’ elastomer	D_2^*, E_2^*	$\dot{D}_2^*$, $\dot{E}_2^*$	$\boldsymbol{T}^*$	$\dot{\boldsymbol{T}}^*$

4.2 Surface instabilities in three elastomer devices

The bifurcation equation was obtained as previously explained and solutions sought for the three different electro-elastic actuation paths, introduced in section 3.1, were plotted using the specialised boundary conditions in the previous section. In order to obtain the bifurcation equation, the expression of W_{elec} presented in eq. (2.29) was used to avoid double multiplicity of roots s occurring when the ideal dielectric strain-energy equation is adopted. However, to make sure that the ideal dielectric behaviour was maintained, it was verified that the limit $\bar{\gamma}_0$, $\bar{\gamma}_2 \to 0$, $\bar{\gamma}_1 \to 1$ converges in the solutions.

Figure 4.2 shows the limit of the stability domains for the half-space with attached compliant electrodes and charge-controlled actuation in blue and orange, respectively. They are plotted together with the fundamental loading paths, shown by the dotted lines, obtained from eq. (3.6). The pre-stress τ_{pre}/μ is varied, starting from 0 to 2.5, increasing in increments of 0.5. In Fig. 4.2 (a) the normalised electric displacement $\bar{D}$ is reported in the ordinate, whereas in (b) the normalised voltage $\bar{V}$ is selected. For the attached compliant electrodes and charge-controlled configurations, the voltage is normalised using the initial thickness as $\bar{V} = (\Phi/d_0)\sqrt{(\varepsilon/\mu)}$, where for the floating elastomer it is as before. Surface instabilities occur at lower values of the electric actuation over the whole domain for the finite deformation induced by attached compliant electrodes. This shows that the presence of the incremental outer electric field causes a stabilising effect delaying the onset of surface instabilities, as $\dot{D}_2^*$ and $\dot{E}_2^*$ are not null for the charge-controlled actuation. For both actuation cases the onset of instability could theoretically be delayed to reach higher values of $\bar{D}$ or $\bar{V}$, by

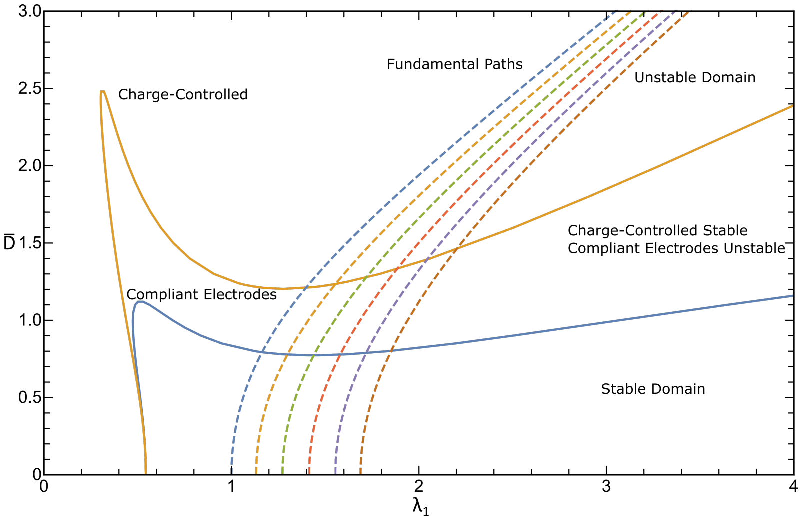

(a) Electric Displacement

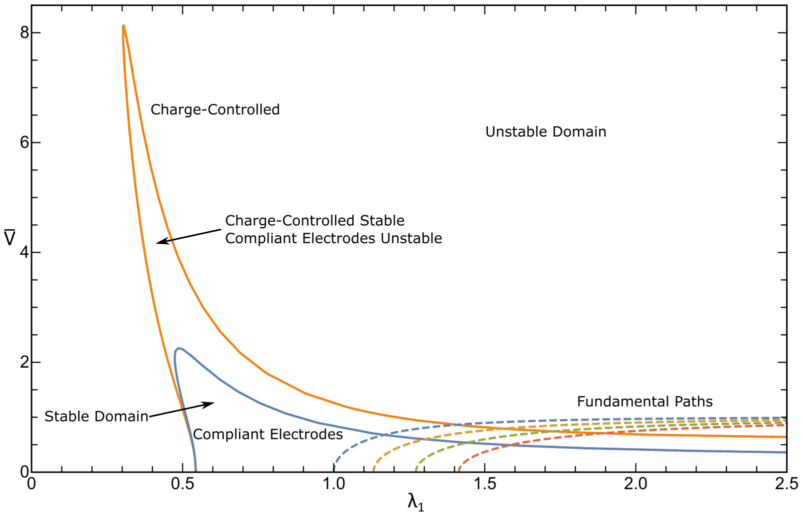

(b) Voltage

Fig. 4.2 Limit of the stability domains for a neo-Hookean substrate with either attached compliant electrodes or charge-controlled boundary condition. Dotted lines represent loading paths with τ_{pre}/μ starting from 0 with increments of 0.5. Figures (a) and (b) represent the same results, but with a different non-dimensional electric variable on the ordinate.

controlling the loading path to make the stable path to reach the local maxima evident in the bifurcation domains. This peak is more pronounced in the charge-controlled actuation compared to the attached compliant electrodes and can be seen even more marked when the voltage is represented allowing theoretically much higher voltages to be reached. Given the almost flat trend of the curves limiting the stability domains between $1 < \lambda_1 < 2$, the pre-stress does not have much influence on the onset of surface instabilities. A very high pre-stress would be needed to significantly delay the onset of surface instabilities. To highlight the magnitude of voltages at bifurcation, an elastomer with thickness $d_0 = 700$ μm, and material parameters set as $\varepsilon = 4.68\,\varepsilon_0$ and $\mu = 100$ kPa is considered, which model well PDMS/silicone-based dielectric elastomers [74]. Following the fundamental loading curve for $\tau_{pre} = 0$, the onset of surface instability occurs at approximately 23.4 kV and 29.7 kV for compliant attached electrodes and charge-controlled configurations, respectively, showing an increase of $> 20\%$ with the stabilising outer incremental electric field.

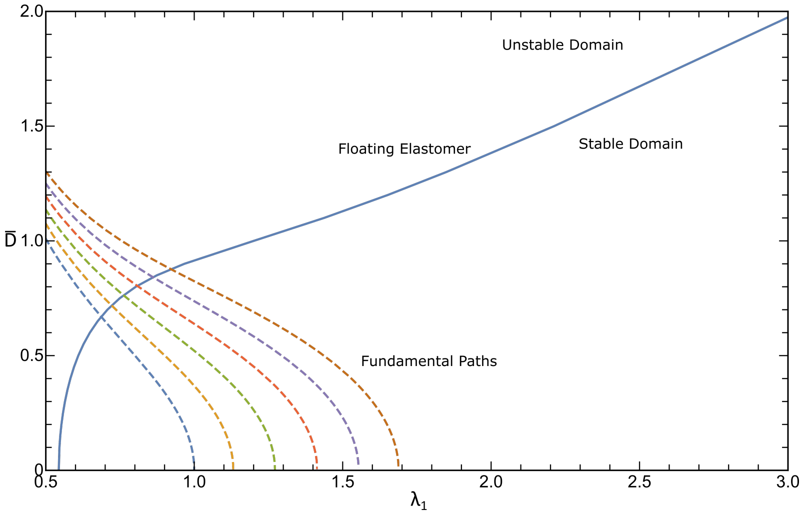

Fig. 4.3 Limit of the stability domain for a neo-Hookean substrate actuated as a ‘floating’ elastomer in vacuum. Dotted lines represent loading paths with τ_{pre}/μ going from 0 to 2.5 in increments of 0.5. Actuation is represented by the non-dimensional electric displacement $\bar{D}$.

Figure 4.3 shows the stability domain for the ‘floating’ elastomer configuration plotted as a λ vs. $\bar{D}$ diagram. The electric displacement is instrumentally used, as it is independent of the aspect ratio d_0/L of the film, thus representing the critical states of all possible geometries. Again, the dotted lines show the fundamental loading path from eq. (3.13) with a pre-stress τ_{pre}/μ going from 0 to 2.5 in increments of 0.5. Differently from the previous cases, the bifurcation curve does not show a local maximum. Now a tensile pre-stress is more influential as it allows the elastomer to experience higher values of $\bar{D}$ in a stable configuration. Continuing the comparison with the two previous actuation methods, for the ‘floating’ elastomer case surface instabilites occur at a lower value of $\bar{D}$. Specific geometries for the specimen were then analysed using the non-dimensionalised voltage $\bar{V}$. Figure 4.4 shows two characteristic loading paths (in blue) combined with bifurcation curves (in orange) for two extreme values of d_0/L (the expansion limit is represented by a black dot along the curve). When the elastomer is very thick compared to the gap between

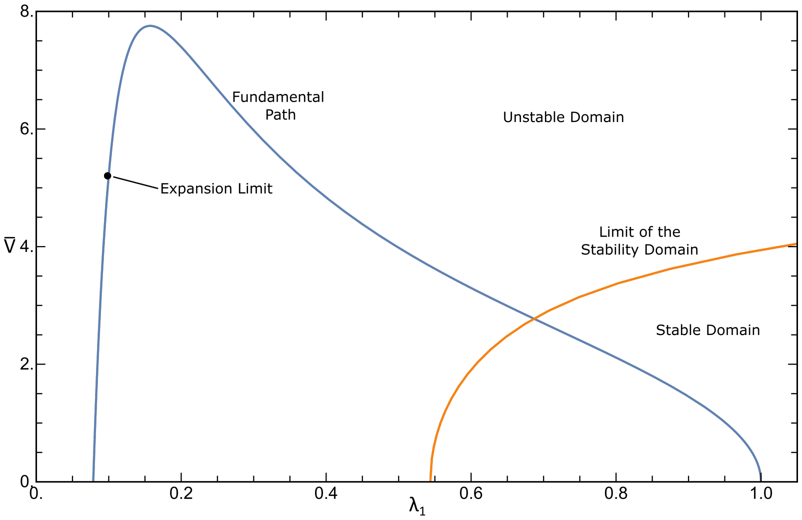

(a) d_0/L of 0.1

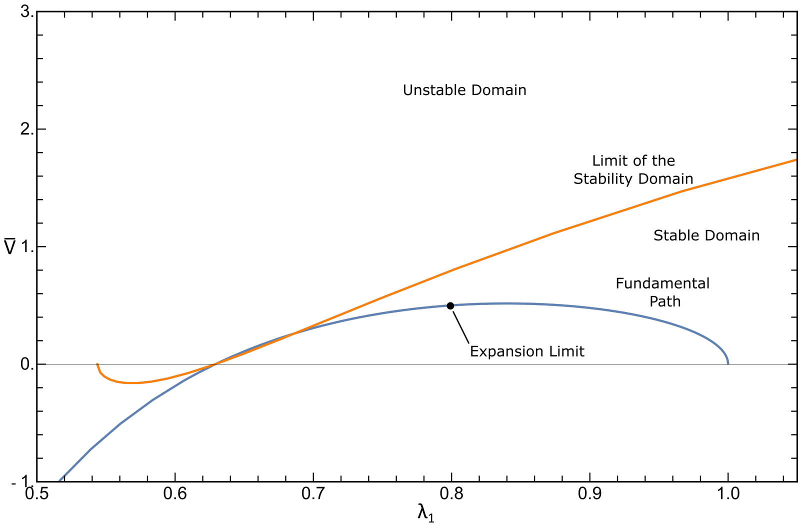

(b) d_0/L of 0.8

Fig. 4.4 Fundamental path for a neo-Hookean substrate actuated as a 'floating' elastomer (blue) and the limit of the stability domain (orange) for $d_0/L = 0.1$ (a) and $d_0/L = 0.8$ (b). Dots mark the expansion limit in each case. λ_1 varies with the non-dimensional electric potential jump $\bar{V}$.

the electrodes, as in Fig. 4.4 (b), the elastomer hits the expansion limit before the onset of surface instabilities. With low values d_0/L (Fig. 4.4 (a)), the elastomer expands a lot more and intersects the bifurcation curve before it reaches that limit, implying that surface instabilities are mainly present in thinner elastomers. In the thicker elastomer the expansion limit and electro-mechanical instabilities appear before the onset of surface instabilities. A thinner elastomer is also able to reach much higher values of $\bar{V}$ and larger stretches before the onset of surface instabilities.

To better understand the characteristics of the surface instability, incremental fields at the onset of bifurcation were studied. The simple loading path with no pre-stress was chosen, at the point of intersection with the bifurcation curve. Coefficients U_j $(j = 1, 2, 3)$ and ϕ_c were solved for the specific case. They were normalised such that the displacement u_2 at the surface $(x_2 \to 0)$ was 5% of the wavelength of the deformation. Figure 4.5 displays the plot of this quantity into the thickness of the elastomer normalised with the wavelength $x_2k/(2\pi)$ (k selected as a unitary value). Reported curves show that the attached compliant electrodes and the charge-controlled cases exhibit a near identical incremental deformation. They decay a lot faster into the thickness, within one wavelength, compared to the actuated 'floating' elastomer counterpart. In addition, in the latter mode, the elastomer exhibits a maximum expansion just under the surface before decaying. Figure 4.6 demonstrates how the boundary conditions influence the component parallel to the surface, of the normalised incremental electric field $\bar{E}_1 = \hat{E}_1/\sqrt{\mu/\varepsilon}$. Following our specialised incremental boundary conditions, as expected it can be noted that for the attached compliant electrodes (in orange) $\bar{E}_1$ is null, whereas that is not the case for the other two configurations. For the first analysed fundamental path, $\bar{E}_1$ increases significantly into the depth of the elastomer before decaying again. For the other two actuation cases this does not occur. The difference between the charged-controlled and floating configurations is that the former shows the longitudinal incremental electric field decaying slower even though it has a lower maximum value. This correlates to the incremental displacement field plots in Fig. 4.5.

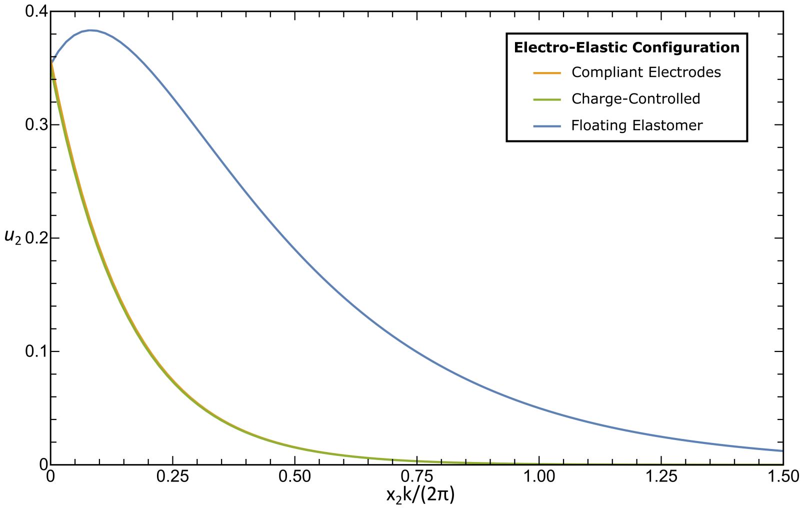

Fig. 4.5 Incremental displacement u_2 into the elastomer thickness normalised with the wavelength $(x_2k/(2\pi))$ for the three analysed electro-elastic problems.

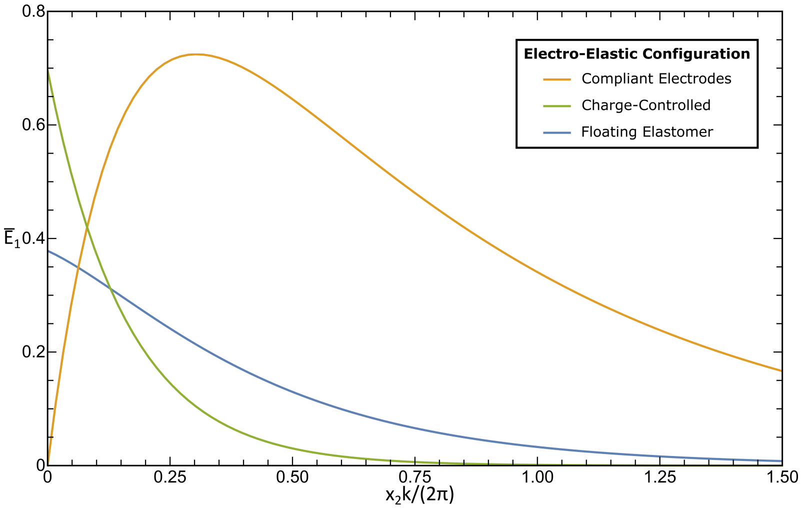

Fig. 4.6 Normalised incremental longitudinal electric field $\bar{E}_1$ into the elastomer thickness normalised with the wavelength $(x_2k/(2\pi))$ for the three analysed electro-elastic problems.

4.3 Surface coating theory for stiff electrodes

The effect of the stiffness of the electrode on surface instabilities can be analysed by using the theory of surface coating to obtain boundary conditions for the electro-elastic substrate. This follows the work done by Steigmann and Ogden [54, 55], who explored bifurcation of and wave propagation on an elastic half-space with a thin coating on its plane boundary. In this section, the basic notions of the surface-coating theory suitable for incremental fields are recalled.

The electrode film is assumed to be fully compliant to the elastomer such that, in the pre-bifurcation state, the stretch $\boldsymbol{\lambda}$ is the same in both elements. As shown in Fig. 4.7, $\boldsymbol{\nu_1}(S)$ is the unit tangent to the surface that is described by an arc length S. Vectors $\boldsymbol{e}_1$ and $\boldsymbol{e}_2$ form the orthonormal unit basis associated with x_1^0 and x_2^0. The leftward unit normal is defined by $\boldsymbol{\nu_2}(S) = \boldsymbol{k} \times \boldsymbol{\nu_1}(S)$, where $\boldsymbol{k} = \boldsymbol{e}_1 \times \boldsymbol{e}_2$. If $\theta(S)$ is the counter-clockwise angle between $\boldsymbol{\nu_1}$ and $\boldsymbol{e}_1$, differentiation with respect to S yields

$$\boldsymbol{\nu}_1'(S) = \kappa(S)\boldsymbol{\nu_2}(S), \quad \kappa(S) = \theta'(S), \tag{4.18}$$

where $()' = d/dS$ and $\kappa(S)$ is the nominal curvature of the film. The unit tangent to the surface can also be decomposed into the directions from the orthonormal unit basis as,

$$\boldsymbol{\nu}_1 = \cos(\theta(S))\boldsymbol{e}_1 + \sin(\theta(S))\boldsymbol{e}_2. \tag{4.19}$$

The coating is assumed to be hyperelastic and is characterised by the elastic strain energy per unit length $U(\Lambda, \kappa)$, where the first argument is the current axial stretch of the electrode. Axial force and bending moment can be obtained by partial differentiation, namely,

$$F = U_{,\Lambda} \quad \text{and} \quad M = U_{,\kappa}. \tag{4.20}$$

In addition to the axial component, the total force at a generic point of the surface has a normal component, say G, such that the force can be decomposed as

$$\boldsymbol{f} = F\boldsymbol{\nu_1} + G\boldsymbol{\nu_2}. \tag{4.21}$$

G is not obtained by a constitutive equation as the thin film is assumed to have vanishing thickness: it is an unknown of the problem. In this plane strain model of the electrode the response is determined solely by the curvature of the electrode. Following [54, 55], linear momentum and moment-of-momentum balances in a static problem for the film give the local equations

$$\boldsymbol{f}' = \boldsymbol{S}\boldsymbol{n}^0, \quad M' + \Lambda G = 0. \tag{4.22}$$

The first equation couples the behaviour of the elastomer and the electrode coating while the latter is the required condition to determine G, so that the force, eq. (4.21), is fully determined.

The incremental boundary conditions are required to add to the bifurcation problem. Recalling notation from section 2.3, and the governing equations applying as before, the increment of eqs. (4.22) is taken and they are updated from S to current arc length s, given that $\Lambda = \mathrm{d}s/\mathrm{d}S$, yielding

$$\dot{\boldsymbol{f}}'(s) = \boldsymbol{\Sigma}\boldsymbol{n}, \quad \dot{M}'(s) + \Lambda^{-1}\dot{\Lambda}G + \dot{G} = 0, \tag{4.23}$$

where the derivative is now taken in terms of s, $()' = d/dS$. The incremental counterpart of eq. (4.21) gives

$$\dot{\boldsymbol{f}} = \dot{F}\boldsymbol{\nu_1} + \dot{G}\boldsymbol{\nu_2} + F\dot{\boldsymbol{\nu}}_\mathbf{1} + G\dot{\boldsymbol{\nu}}_\mathbf{2}, \tag{4.24}$$

where $\dot{F}$ is given by

$$\dot{F} = F_{,\Lambda}\dot{\Lambda} + F_{,\kappa}\dot{\kappa}. \tag{4.25}$$

By knowing that $\dot{\boldsymbol{\nu}}_{\boldsymbol{1}} = \dot{\theta}\boldsymbol{\nu_2}$ and $\dot{\boldsymbol{\nu}}_{\boldsymbol{2}} = -\dot{\theta}\boldsymbol{\nu_1}$, with the previous equations, the following equation is achieved

$$\dot{\boldsymbol{f}} = (\dot{F} - G\dot{\theta})\boldsymbol{\nu_1} + (F\dot{\theta} + \dot{G})\boldsymbol{\nu_2}. \tag{4.26}$$

The expression for $\dot{\boldsymbol{f}}'$ can be obtained from eq. (4.26) once $\dot{G}$ and G are known. To solve the term $\dot{G}$ eq. $(4.23)_2$ is used and the term G is obtained from the updated counterpart of eq. $(4.22)_2$, namely

$$M' + G = 0. \tag{4.27}$$

The use of $\boldsymbol{\nu_1} = \theta'\boldsymbol{\nu_2} = \Lambda^{-1}\kappa\nu_2 = -\theta'\boldsymbol{\nu_1}$, $\boldsymbol{\nu_2'} = -\theta'\boldsymbol{\nu_1} = -\Lambda^{-1}\kappa\boldsymbol{\nu_1}$ and $\dot{\theta}' = \Lambda^{-1}\dot{\kappa}$ yields

$$\dot{\boldsymbol{f}}' = T\boldsymbol{\nu_1} + N\boldsymbol{\nu_2}, \tag{4.28}$$

where

$$\begin{aligned}
T &= \dot{F}' + \Lambda^{-1}\dot{\kappa}M' + M''\dot{\theta} - \Lambda^{-1}\kappa(F\dot{\theta} + M'\Lambda^{-1}\dot{\Lambda} - \dot{M}'),\\
N &= \Lambda^{-1}\dot{\kappa}F + F'\dot{\theta} + \Lambda^{-1}M'(\dot{\Lambda}' - \Lambda^{-1}\Lambda'\dot{\Lambda}) + \Lambda^{-1}\dot{\Lambda}M'' - \dot{M}'' + \Lambda^{-1}\kappa(\dot{F} + M'\dot{\theta}).
\end{aligned} \tag{4.29}$$

The following kinematic expressions are needed to solve the incremental variables:

$$\dot{\Lambda} = \Lambda\boldsymbol{\nu_1}\cdot\boldsymbol{u}',\ \dot{\kappa} = \Lambda\boldsymbol{\nu_2}\cdot\boldsymbol{u}'' - \kappa\boldsymbol{\nu_1}\cdot\boldsymbol{u}',\ \dot{\theta} = \boldsymbol{\nu_2}\cdot\boldsymbol{u}', \tag{4.30}$$

where $\boldsymbol{u}$ is the incremental displacement field at the boundary of the half-space defined in previous sections.

The Cartesian coordinate system specific to the problem at hand and indicated in Fig. 4.7 is aligned with the basis such that $\boldsymbol{\nu_1} = \boldsymbol{e}_1$, $\boldsymbol{\nu_2} = \boldsymbol{e}_2$, $\boldsymbol{n} = -\boldsymbol{e}_2$ and $\kappa = M' = G = 0$. The problem is also specialised to the previously introduced dielectric body problem by noting that $\Lambda = \lambda$, as the electrode deforms with the elastomer homogeneously. Therefore, with the help of eqs. (4.30), eqs. (4.29) are simplified and the results inserted into eq. (4.23) to obtain the boundary conditions for the incremental problem, i.e.

$$\Sigma_{12} = -U_{\lambda\lambda}\lambda u_1'' - U_{\lambda\kappa}\lambda u_2''', \quad \Sigma_{22} = U_{\kappa\kappa}\lambda u_2'''' + U_{\kappa\lambda}\lambda u_1''' - U_{\lambda}u_2''. \tag{4.31}$$

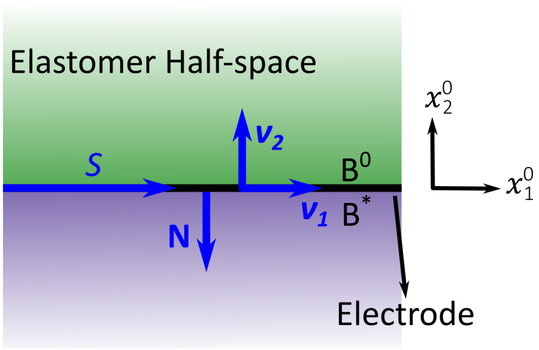

Fig. 4.7 Sketch of the electro-elastic half-space in the reference configuration (B^0) coated by a 'stiff' electrode. B^* represents the surrounding vacuum.

A simple elastic strain-energy function for the electrodes can be chosen [55] as

$$U(\lambda,\kappa) = \frac{1}{2}m(\lambda-1)^2 + \frac{1}{2}n\kappa^2, \tag{4.32}$$

which is an expression analogous to that of structural plates with stretching and bending. As such, it can be deduced that the parameters m and n may be interpreted as

$$m = \frac{E_c h}{1-\nu_c^2}, \quad n = \frac{E_c h^3}{12(1-\nu_c^2)}, \tag{4.33}$$

where E_c and ν_c are the Young's modulus and Poisson's ratio for the coating material, respectively, and h is the film thickness. Additional terms could be added to $U(\lambda,\kappa)$ to take residual stresses into account, but are assumed to be null in this investigation.

4.4 Effect of the stiffness of the electrode on surface instabilities

In this section three different types of electrodes are examined to show a range of materials that might be typically encountered, and the bifurcation equations for each are obtained to analyse electro-elastic surface instabilities.

The previously described generic boundary conditions were obtained from eqs. (4.12) and (4.13). These conditions are specialised as seen in Table 4.1 for the attached compliant electrodes case, which is the pertinent case when wanting to include electrode stiffness effects. To take the stiffness of the electrodes into account, the boundary conditions are derived and given by eqs. (4.31) are used, acting on the incremental stress terms. Using these new conditions and the strain-energy function for the electrode eq. (4.32), the bifurcation equation was obtained using the same method as before. It is important to note that the introduction of the electrode stiffness causes the bifurcation equation to be dependent on the wavenumber, in particular, due to the fourth-order derivative in eq. $(4.31)_2$, it is a quartic in k. As such, a complex set of solutions depending on the wavenumber are expected, as also discussed by Ogden and Steigmann [55] and Gei [75]. It is worth mentioning that the model was verified by obtaining the elastic results presented in [55], where the electric field is absent, by setting the electric actuation to null.

Material properties for the electrodes are needed to obtain the material parameters m and n in eqs. (4.33), namely, Young's modulus and Poisson's ratio. The material properties m and n have dimensions of *length*×*pressure* and *length*^{3}× *pressure*, respectively. As such $(n/m)^{1/2}$ can be used as a length scale to normalise the wavenumber as $\bar{k} = k(n/m)^{1/2}$. To compare the three electrode materials, m and n are also normalised such that $\bar{m} = \bar{n} = (m/\mu)(m/n)^{1/2}$; in addition, they are assumed as incompressible. All the chosen materials may undergo large strains as they are highly stretchable and offer good conductivity. They are also common materials currently being used or researched for use as electrodes in elastomer devices.

The first chosen material consists of a PDMS matrix combined with conductive materials such as graphene or carbon black. A typical value for Young's modulus is shown to be 0.9 MPa with an electrode thickness of $h = 30$ μm [76, 77], giving $m = 35.5$ Pa m, $n = 2.66 \times 10^{-9}$ Pa m^3 and $\bar{m} = 41.57$. The second material shares the matrix with the first one, but the reinforcement is composed of metal ions, such as gold or titanium, that are implanted into the PDMS matrix. Information on the manufacturing process and their material parameters were shown by Niklaus and Shea [78] and Shea [79], which measured a Young's modulus of 2 MPa and an electrode thickness of $h = 50$ nm. This provides $m = 0.13$ Pa m, $n = 2.74 \times 10^{-17}$ Pa m^3, and $\bar{m} = 91.17$. Alternative electrode materials are ionogels which consist of an ionic liquid immobilised in a polymer matrix. Material values were taken by Ji et al. [80], with a Young's modulus of 192 kPa and an electrode thickness of $h = 750$ nm, yielding $m = 0.19$ Pa m, $n = 8.88 \times 10^{-15}$ Pa m^3 and $\bar{m} = 8.75$. Table 4.2 summarises the material parameters and as can be seen, a wide range of $\bar{m}$ values is obtained with the chosen materials allowing a good analysis of any electrode material in between.

As the bifurcation diagrams are similar for the three electrode materials, the graphene-implanted electrode is presented for analysis for which the dimensionless stiffness $\bar{m} = 41.57$ is the median one among the three materials.

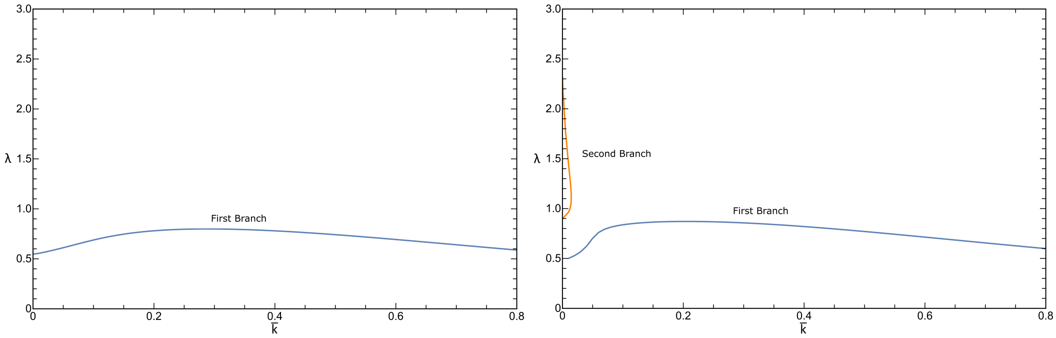

(a) $\bar{D}$ of 0.01 (b) $\bar{D}$ of 0.87

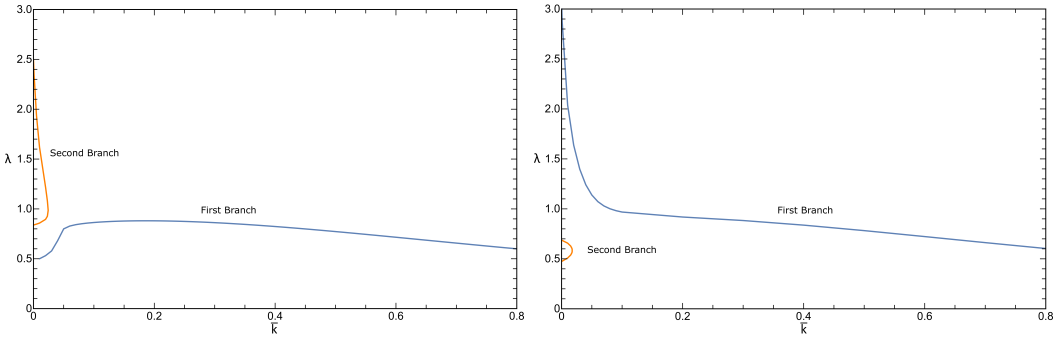

(c) $\bar{D}$ of 0.90 (d) $\bar{D}$ of 1.00

Fig. 4.8 Bifurcation diagram for an actuated neo-Hookean elastomer coated with a 'stiff' electrode. The material parameters for a graphene implanted electrode were used, i.e. $\bar{m} = 41.57$. λ_1 is plotted against the normalised wavenumber $\bar{k}$ and various values of $\bar{D}$ are considered in the different plots. Blue and orange represent two different branches of the solution to the bifurcation equation.

Figure 4.8 shows the bifurcation diagrams where λ is plotted against $\bar{k}$ for an increasing $\bar{D}$. For low values of the electric displacement, Fig. 4.8 (a) where $\bar{D} = 0.01$, there is only one solution of the bifurcation equation, like in the case of the ideal electrode seen in the previous section. The critical λ in this case is the maxima of the curve (i.e., $\bar{k} = 0.290$, $\lambda = 0.799$). It is of note that, as $\bar{k} \to 0$, the solution for negligible electrode stiffness (i.e., uncoated half-space) is obtained for all values of electric displacement. For $\bar{D} > 0.773$, a new branch emerges (see Fig. 4.8 (b)). This provides two additional solutions, which correspond to the minimum and maximum λ values of that branch and

Table 4.2 Material properties for chosen electrode materials

Material	$Young's$	h	m/Pa m	n/Pa m^3	$\bar{m}$
Ion implanted	2 MPa	50 nm	0.13	2.74×10^{-17}	91.17
Graphene implanted	0.9 MPa	30 μm	35.5	2.66×10^{-9}	41.57
Ionogels	192 kPa	750 nm	0.19	8.88×10^{-15}	8.75

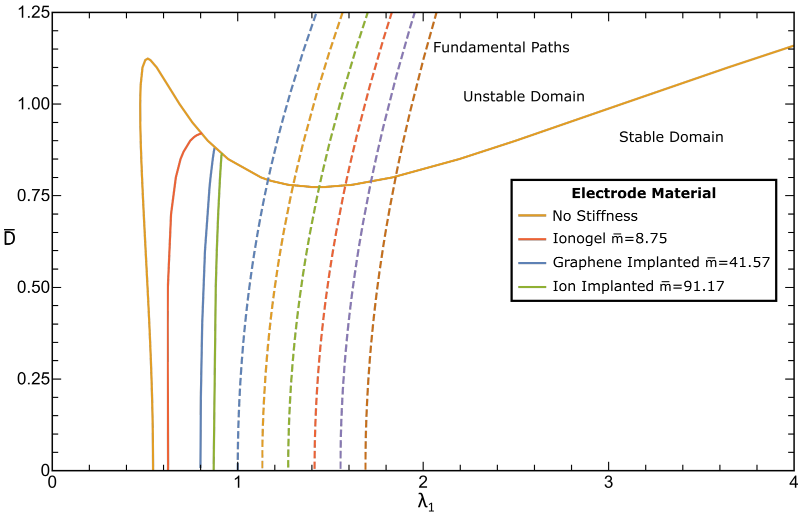

Fig. 4.9 Limit of the stability domain for a neo-Hookean elastomer shown as various electrode materials with varying stiffness are assumed (varying $\bar{m}$). Dotted lines represent loading paths of a dielectric elastomer with τ_{pre}/μ going from 0 to 2.5 in increments of 0.5. Actuation is described by the non-dimensional electric displacement $\bar{D}$.

occur as $\bar{k} \to 0$. As $\bar{D}$ is increased further, the maxima from the first branch has a higher critical λ than the lowest solution of the new second branch (Fig. 4.8 (c)). This causes the overall bifurcation curve (displayed in Fig. 4.9) to have only one solution which is the one with the highest λ. At this point, as the solution occurs as $\bar{k} \to 0$, the instability curve is following the one for the ideal electrode meaning the stiffness of the electrode no longer has an effect. The solution then switches form and the two branches merge into one (Fig. 4.8 (d)). The highest λ as $\bar{k} \to 0$ continues to be the dominant critical stretch as the maxima from the first branch disappears.

These instability curves for the various electrodes are plotted in Fig. 4.9. These are obtained by carefully checking the critical λ_{crit} (more than one solution may exist) on the bifurcation diagram analysed in Fig. 4.8 at a given $\bar{D}$. The curves pertain to ionogel (red), graphene-implanted (blue) and ion-implanted (green) electrodes, together with the solution where electrode stiffness is disregarded (orange) obtained in the previous section. The dotted lines represent the loading paths of a dielectric elastomer (attached compliant electrode) with various states of pre-stress. Taking into account the stiffness of the electrodes causes the bifurcation curve to start at higher critical stretches for low $\bar{D}$, though always for $\lambda_1 < 1$. The curves then go up much more linearly with a high slope until they reach that for a fully compliant electrode, which then takes over. Compared to the uncoated case, the peak that was present

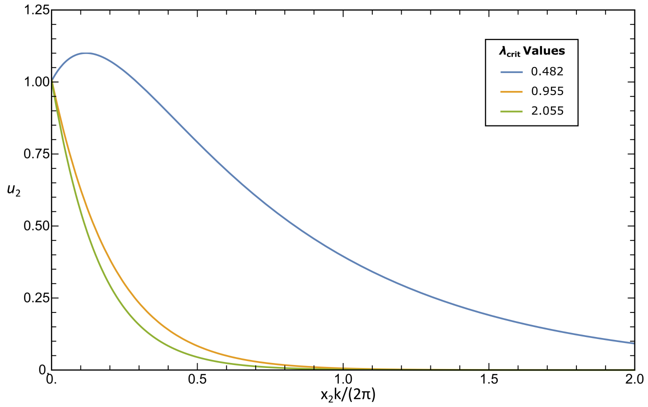

(a) u_2

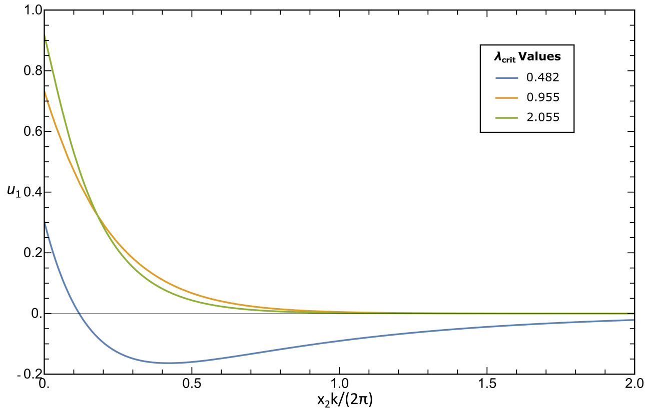

(b) u_1

Fig. 4.10 Incremental displacement fields u_2 and u_1, into the thickness x_2 of a neo-Hookean elastomer, normalised with the wavelength $2\pi/k$. The actuation case is that of an attached compliant electrodes with the stiffness taken into account. The material parameters for a graphene implanted electrode was used with $\bar{m} = 41.57$. Curves represent the three solutions when $\bar{k} = 0.001$ and $\bar{D} = 0.85$, with varying λ_{crit} values.

vanishes in all three cases. As $\bar{m}$ increases the bifurcation curve becomes more vertical and the critical lambda at $\bar{D} = 0$ also increases. However, following the fundamental paths considered in this investigation, this effect is not actually seen as the original curve takes over at a critical λ_{crit} lower than the intersection of the fundamental paths. This implies that for typical applications it is valid to assume that the electrodes are fully compliant.

To analyse the features of the bifurcation modes for the various branches described earlier, let us consider the parameter $\bar{D} = 0.85$, $\bar{k} = 0.001$, a case similar to that displayed in Fig. 4.8 (b). Again, the graphene-implanted electrode case is adopted ($\bar{m} = 41.57$). The three critical values of λ for the given $\bar{k}$ are equal to 0.482, 0.955 and 2.055. These values were used to calculate

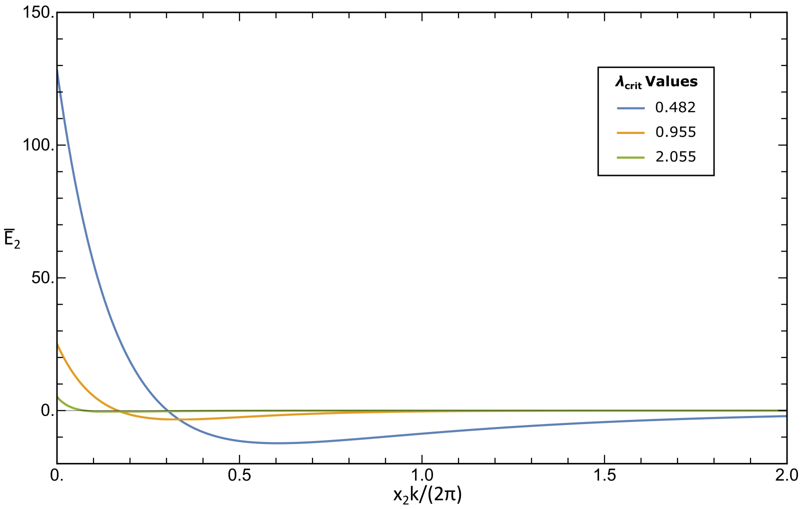

Fig. 4.11 The normalised transverse incremental electric field $\hat{E}_2$, is shown into the thickness x_2 of a neo-Hookean elastomer, normalised with the wavelength $2\pi/k$. The actuation case is that of an attached compliant electrodes with the stiffness taken into account. The material parameters for a graphene implanted electrodes were used with $\bar{m} = 41.57$. Curves represent the solutions when $\bar{k} = 0.001$ and $\bar{D} = 0.85$, with varying λ_{crit} values.

the eigensystem of the three coefficients (U_1, U_2, U_3, cf. eq. (4.7)), and the modes were normalised such that the incremental displacement $u_2 = 1$ at the surface of the half-space. The incremental displacement fields are displayed in Fig. 4.10. Functions u_2 and u_1 are plotted into the thickness of the elastomer x_2 normalised with the wavelength $2\pi/k$. The orange and green curves correspond to the solutions appearing only at a higher $\bar{D}$ corresponding to the orange branch in Fig. 4.8 (b), and are similar in nature. The blue curve, corresponding to the first branch with the lowest λ_{crit}, has a peak just inside the surface for the displacement u_2 and an inversion in u_1. In general, the two solutions from the second branch are more localised to the surface of the half-space, a finding similar to those observed in [55, 75] in analogous purely-elastic problems. This is also the case for the normalised transverse component of the incremental electric field, $\bar{E}_2$ in Fig. 4.11. For the incremental electric fields, the general shape of the curve is very similar. However, with lower λ_{crit} values, the incremental electric field is much higher (over five times more) meaning an instability mode where the electric field plays a bigger role. It is also interesting to note that with the largest solution $\lambda_{crit} = 2.055$ there is a difference in the component $\bar{E}_1$ that distinguishes it from the other two solutions. While they all start off as $\bar{E}_1 = 0$ on the surface due to the electric boundary conditions, for this particular solution there is a peak just inside the thickness of the elastomer of a value around 10% the maximum $\bar{E}_2$. For the other solutions $\bar{E}_1$ is of several orders of magnitudes lower.

The incremental von Mises stress is defined as

$$\Sigma_v = \sqrt{\frac{1}{2}\left[(\Sigma_{11}-\Sigma_{22})^2+(\Sigma_{22}-\Sigma_{33})^2+(\Sigma_{33}-\Sigma_{11})^2\right]+3(\Sigma_{12}^2+\Sigma_{23}^2+\Sigma_{31}^2)}. \tag{4.34}$$

In Fig. 4.12, the contour plots of incremental von Mises stress are plotted for the three values λ_{crit}. Here again the big difference in decay into the thickness of the half-space with a lower λ_{crit} is evident. It can also be observed that in Fig. 4.12 (a) there is a significant inversion just inside the thickness of the elastomer implying an instability mode that has large varying stresses just under the surface. In Fig. 4.12 (b) the inversion is still present, but it appears when the incremental stress has already decayed and is almost null whereas in Fig. 4.12 (c) the plotted quantity decays monotonically with depth.

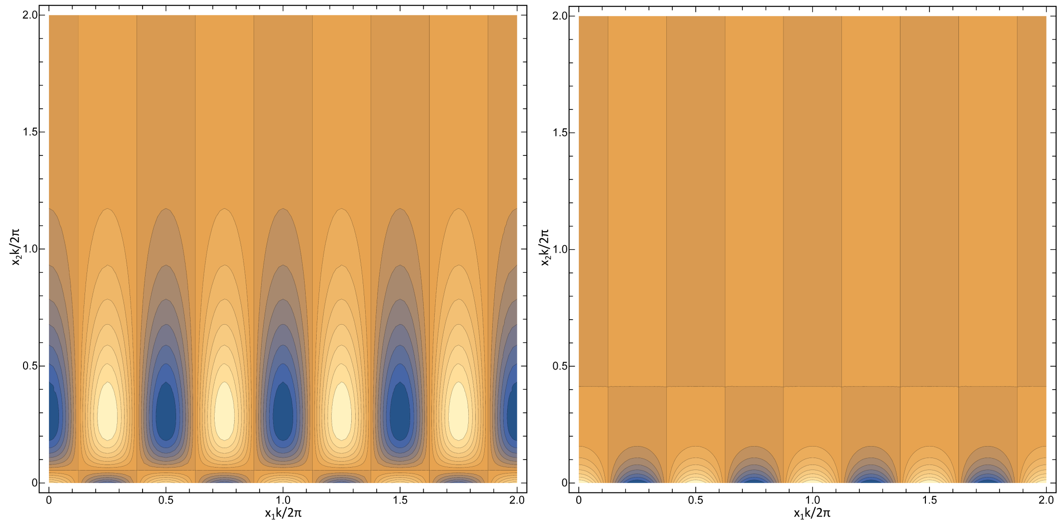

(a) λ_{crit} of 0.482 (b) λ_{crit} of 0.955

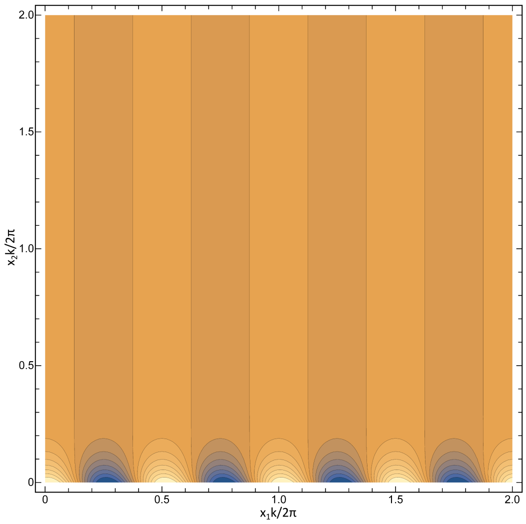

(c) λ_{crit} of 2.055

Fig. 4.12 Contour plots of the incremental von Mises stress at the onset of instability for a neo-Hookean elastomer with a stiff electrode ($\bar{m} = 41.57$). The domain has been normalised with the wavelength $2\pi/k$. The three solutions correspond to $\bar{k} = 0.001$ when $\bar{D} = 0.85$, with varying values of λ_{crit} plotted separately.

Chapter 5

Small strain actuation of electro-elastic laminates

Composite elastomers are used to enhance characteristics of the elastomer deformation when actuated. In this chapter the standard device with compliant electrodes is investigated with a laminate composite elastomer sandwiched in between. These composite materials can exhibit an inversion of actuation, switching from longitudinal expansion of the elastomer (the ‘conventional’ deformation for a homogeneous material) to contraction, when the right geometrical and material parameters are picked. This research aims to analyse these hierarchical laminated composites to understand the conditions which cause the onset of this new actuation mode. The presence of this inversion is shown in both rank–1 and rank–2 laminate composites. First the rank–1 laminate onset of inversion is examined, looking at the geometrical and material criteria with different boundary conditions. It is analysed in depth to understand how each composite phase deforms before, during and after the onset of inversion. The rank–2 composite is then compared to the rank–1 solution to show how a rank–2 is able to enhance this mode of actuation further. As a rank–2 has a lot more parameters, a guideline is provided on how to optimise them to obtain the desired actuation. The analysis is carried out assuming plane-strain conditions. Some 3D solutions were analysed which showed results almost identical to the simpler plane-strain problem, and as such plane-strain is assumed throughout.

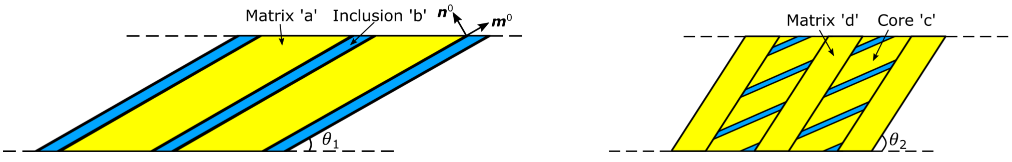

(a) Rank–1 (b) Rank–2

Fig. 5.1 Figure of a rank–1 (a) and rank–2 (b) laminated composite.

5.1 Plane-strain actuation of rank–1 laminates

5.1.1 Small deformation linear electro-elasticity

To study the behaviour of hierarchical composite laminates the theory of small electroelastic deformations is used throughout this chapter. The deformations are linearised causing the Lagrangian and Eulerian representations to be approximately the same. The general theory remains similar to previous chapters, however, the notation is unique to this chapter. At first a rank–1 layered composite elastomer slab is investigated, which is obtained by repeating a unit cell consisting of two compressible dielectric materials as shown in Figure 5.1 (a). The two materials in the composite, the first a soft matrix material and the second a stiffer inclusion material, are denoted as 'a' and 'b' respectively. The composite is defined by a generic rank-1 lamination angle θ_1 and the volume fraction of each material c^a and c^b where $c^a + c^b = 1$. The vectors defining the interface between the two materials in the reference configuration, are $\boldsymbol{n}^0$ and $\boldsymbol{m}^0$, in the normal direction and along the interface respectively. In component form these are,

$$\boldsymbol{n}^0 = \Big(-\sin\theta_1, \cos\theta_1\Big), \quad \boldsymbol{m}^0 = \Big(\cos\theta_1, \sin\theta_1\Big). \tag{5.1}$$

In the small deformation framework, the composite is actuated as before by an electric field $\boldsymbol{E}$ with a corresponding electric displacement $\boldsymbol{D}$, with the total stress generated indicated by $\boldsymbol{S}$. With the assumption of the absence of both volume charges and body forces, the governing equations resemble eqs. (2.7) and (2.16) and are,

$$\mathrm{div}\boldsymbol{S} = \boldsymbol{0}, \quad \mathrm{div}\boldsymbol{D} = 0, \quad \mathrm{curl}\boldsymbol{E} = \boldsymbol{0}. \tag{5.2}$$

Both the composite materials follow the relationship of an ideal dielectric $\boldsymbol{D} = \varepsilon\boldsymbol{E}$ where ε is the permittivity of the material that is independent of deformation. Continuity on the interfaces between the two materials can be enforced by imposing the following jump conditions

$$\boldsymbol{n}^0 \cdot [\![\boldsymbol{D}]\!] = 0, \quad \boldsymbol{n}^0 \times [\![\boldsymbol{E}]\!] = \boldsymbol{0}, \quad [\![\boldsymbol{S}]\!]\boldsymbol{n}^0 = \boldsymbol{0}, \quad \boldsymbol{m}^0 \cdot ([\![\boldsymbol{e}]\!]\boldsymbol{m}^0) = 0, \tag{5.3}$$

where $\boldsymbol{e}$ denotes the strain tensor. The brackets $[\![\cdot]\!]$ indicate the jump across the interfaces in the composite defined as $[\![f]\!] = f^a - f^b$.

Under the assumption of a homogeneous response, the average quantities are defined in the whole composite as a sum of the quantities in each phase. The average quantities are thus given as

$$\boldsymbol{E}^{av} = c^a\boldsymbol{E}^a + c^b\boldsymbol{E}^b, \quad \boldsymbol{S}^{av} = c^a\boldsymbol{S}^a + c^b\boldsymbol{S}^b, \quad \boldsymbol{e}^{av} = c^a\boldsymbol{e}^a + c^b\boldsymbol{e}^b. \tag{5.4}$$

The jump conditions eq. $(5.3)_2$ can be expressed in an alternate form

$$\boldsymbol{E}^a - \boldsymbol{E}^b = \beta\boldsymbol{n}^0, \tag{5.5}$$

where β is a real parameter. This is substituted into eq. $(5.4)_1$ to obtain an expression that relates the singular phases to the average quantity,

$$\boldsymbol{E}^a = \boldsymbol{E}^{av} + c^b\beta\boldsymbol{n}^0, \quad \boldsymbol{E}^b = \boldsymbol{E}^{av} - c^a\beta\boldsymbol{n}^0. \tag{5.6}$$

An analogous procedure is followed for the mechanical problem giving us the expressions

$$\begin{aligned} \boldsymbol{e}^a &= \boldsymbol{e}^{av} - \omega_1 c^b(\boldsymbol{m}^0 \otimes \boldsymbol{n}^0 + \boldsymbol{n}^0 \otimes \boldsymbol{m}^0) - \omega_2 c^b(\boldsymbol{n}^0 \otimes \boldsymbol{n}^0), \\ \boldsymbol{e}^b &= \boldsymbol{e}^{av} + \omega_1 c^a(\boldsymbol{m}^0 \otimes \boldsymbol{n}^0 + \boldsymbol{n}^0 \otimes \boldsymbol{m}^0) + \omega_2 c^a(\boldsymbol{n}^0 \otimes \boldsymbol{n}^0), \end{aligned} \tag{5.7}$$

where ω_1 and ω_2 are real parameters.

With the small-strain limitations and following McMeeking and Landis [34] the stress tensor for a linear isotropic material is given, in each material phase, by

$$\begin{aligned} S^a_{ij} &= 2G^a e^a_{ij} + (B^a - \frac{2G^a}{3})e^a_{kk}\delta_{ij} + \varepsilon^a E^a_i E^a_j - \frac{\varepsilon^a}{2}E^a_k E^a_k \delta_{ij} \\ S^b_{ij} &= 2G^b e^b_{ij} + (B^b - \frac{2G^b}{3})e^b_{kk}\delta_{ij} + \varepsilon^b E^b_i E^b_j - \frac{\varepsilon^b}{2}E^b_k E^b_k \delta_{ij}, \end{aligned} \tag{5.8}$$

where G and B are the shear and bulk moduli of the relevant phase material, respectively, and δ_{ij} represents the Kronecker delta. Note that the above expressions can be split into the elastic and electrostatic stresses which are independent of each other.

Two boundary problems are considered, namely ‘aligned loading’ and macroscopic stress-free conditions. In both cases the composite elastomer is considered actuated in the compliant electrode configuration such that the electric actuation is across its thickness and the normal stresses are null, giving the following boundary conditions

$$E_1^{av} = 0, \quad S_{11}^{av} = S_{22}^{av} = 0. \tag{5.9}$$

For the ‘aligned loading’ problem these are further specified for a configuration which is limited such that there is no shear strain on the composite. In this case extra boundary conditions appear in the overall strain, namely

$$\boldsymbol{e}^{av} = \begin{bmatrix} e_{11}^{av} & 0 \\ 0 & e_{22}^{av} \end{bmatrix}. \tag{5.10}$$

In the macroscopic stress-free conditions there are no boundary conditions on the overall strain. However, the surface of the elastomer is traction free such that,

$$\boldsymbol{S}^{av} = \boldsymbol{0}. \tag{5.11}$$

5.1.2 Actuation under ‘aligned’ loading

An analysis was undertaken to understand how the material and geometrical parameters of the composite affect whether elongation or contraction will occur along the longitudinal axis when actuated by an electric field across the thickness. The former being referred hereafter as the ‘*conventional response*’ and the latter as the ‘*unconventional response*’. At first the more restrictive aligned loading actuation case was studied, obtained by using the boundary conditions given by eqs. (5.9) and (5.10).

Assuming an ideal dielectric, the parameter β is obtained using the jump conditions in $\boldsymbol{D}$ (eq. $(5.3)_1$), and eq. (5.5). In a similar manner, the parameters ω_1 and ω_2 are obtained using the jump conditions in $\boldsymbol{S}$ (eq. $(5.3)_3$), with the stress in each phase given by eqs. (5.8). Once these parameters are obtained, the average strain $\boldsymbol{e}^{av}$ is obtained using the boundary conditions eqs. (5.9) where $\boldsymbol{S}^{av}$ is given by eqs. $(5.4)_2$ and the contribution of each material phase is given by the constitutive eqs. (5.8).

To obtain the actuation response, the material parameters for the two phases need to be set. To this end the bulk modulus is replaced with Poisson’s ratio ν and shear modulus G using the well-known relationship

$$B = \frac{2G(1+\nu)}{3(1-2\nu)}. \tag{5.12}$$

As elastomer materials are typically close to being incompressible, a high Poisson's ratio was chosen for both phases, i.e. $\nu^a = \nu^b = 0.495$. To analyse the response to actuation the material parameters for the soft matrix were fixed to previously used typical values of $G^a = 100$ kPa and $\varepsilon^a = 4.68\,\varepsilon_0$. The stiffer material then has its parameters defined as a function of the softer material, by using $\varepsilon^b = k_1\varepsilon^a$ and $G^b = k_2 G^a$, where k_1 and k_2 are dimensionless constants. Figure 5.2 shows the domains where the actuation behaviour of the laminate transitions from a conventional response, i.e. elongation, to the unconventional response, i.e. contraction: with the curves showing the absence of longitudinal strain, $e_{11}^{av} = 0$, as the elastomer is actuated. In the figure the response is plotted as k_1 varies with the lamination angle θ_1 and the two curves show different shear moduli ratios of $k_2 = 10$ and 100. In both cases the volume fraction of the composite corresponds to $c^a = 0.8$. The ideal lamination angle, which enhances the unconventional behaviour, is approximately 30° for both curves. The curves share an asymptote at $\theta_1 \approx 45°$, meaning that a larger lamination angle would only exhibit a conventional response when actuated. Both curves are very close, meaning that the leading material parameter in determining the actuation transition is the ratio of permittivities k_1, with k_1 being approximately 50-60 when the lamination angle is close to ideal.

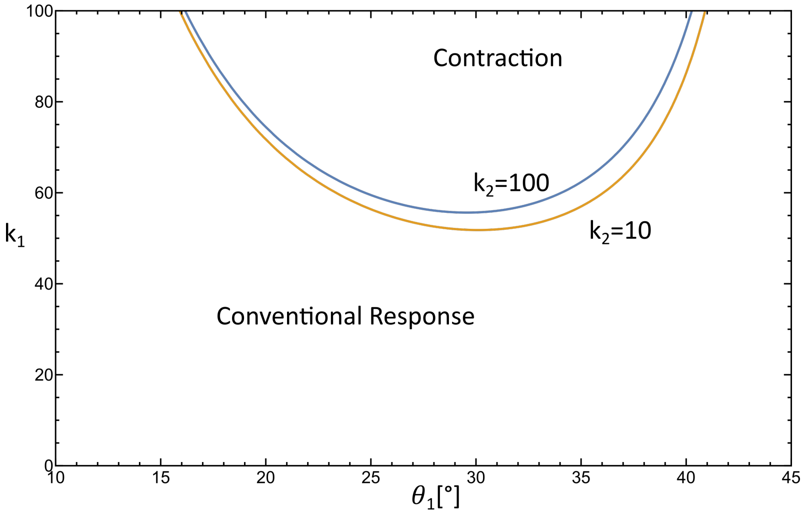

Fig. 5.2 Domains showing inversion of actuation behaviour as k_1 and θ_1 are varied. Orange and blue curves show responses for $k_2 = 10$ and $k_2 = 100$ respectively. Both composites have a volume fraction of $c^a = 0.8$.

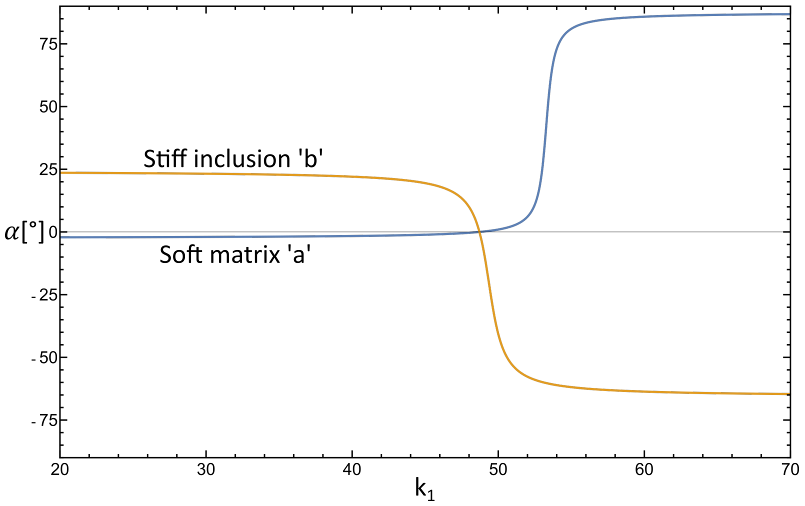

Fig. 5.3 Principal strain orientation angles of the two phases as k_1 is varied. Blue and Orange curves represent the soft and stiff phase respectively. Parameters of $\theta_1 = 30°$ and $k_2 = 10$ are used to achieve a response. A volume fraction of $c^a = 0.8$ is used and the elastomer is actuated at a fixed $E_2^{av} = 100\text{MV/m}$.

To better understand how the transition between elongation and contraction occurs, the rotation and stretch in each material phase are analysed. To get a sense of the deformation in each phase of the composite as the permittivity ratio k_1 is increased, a case with material and geometric parameters of $\theta_1 = 30°$, $k_2 = 10$ and $c^a = 0.8$ is picked. The angle of 30° is chosen as it enhances the unconventional behaviour. The strains in each phase are obtained using eqs. (5.7), which are used to calculate the principal strains $\hat{\boldsymbol{e}}$ and the angle α w.r.t. the longitudinal axis where the principal directions of strain occur. These are obtained by the following equations,

$$\tan(2\alpha) = \frac{2e_{12}}{e_{11} - e_{22}},$$
$$\hat{\boldsymbol{e}} = \boldsymbol{Q}\boldsymbol{e}\boldsymbol{Q}^T, \quad \text{where} \quad \boldsymbol{Q} = \begin{bmatrix} \cos\alpha & \sin\alpha \\ -\sin\alpha & \cos\alpha \end{bmatrix}. \tag{5.13}$$

The elastomer is actuated at a given external macroscopic electric field $E_2^{av} = 100$ MV/m. Figure 5.3 shows how the orientation angle in each phase varies with k_1, and similarly Figure 5.4 shows the principal longitudinal and transverse strain in each phase. It is to note that for that chosen parameters the transition between responses occurs at a value of $k_1 \approx 51.812$. The figures show that in both materials the angle of the principal strain direction exhibits a sudden change as k_1 is increased around the transition value. This is coupled with the principal strains reaching their minimum values. As k_1 moves away

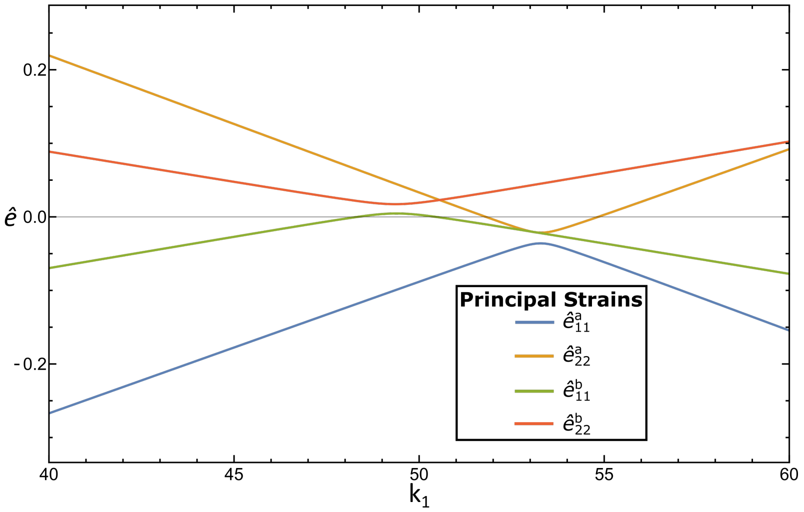

Fig. 5.4 Principal strains of the two phases as k_1 is varied. Curves represent the various principal strains in the two phases. Parameters of $\theta_1 = 30°$ and $k_2 = 10$ are used to achieve a response. A volume fraction of $c^a = 0.8$ is used and the elastomer is actuated at a fixed $E_2^{av} = 100\text{MV/m}$.

from the transition value each material in the composite tends to stabilise in its response, showing linear deformations and constant orientation angles.

To better illustrate what is happening Figure 5.5 shows how a unit cell deforms at various intervals as k_1 is increased. At low values of k_1 the conventional response appears clearly, with both phases elongating longitudinally. The matrix material experiences almost no rotation and the stiff inclusion is angled at around 24°. As the permittivity ratio is increased, the inclusion starts to rotate clockwise until it stabilises an angle of around -65°, with the matrix material rotating counter-clockwise up to an angle of around 87°. During this rotation the strains are small and the leading cause of the transition to the unconventional response is the rotation. When looking at a high value of $k_1 = 70$, both phases are clearly rotated in such a way that the elongation occurs transversally. Around the transition value of $k_1 \approx 51.812$ large changes in rotation occur at very small increases of k_1 in both materials, with the stiff inclusion leading the matrix. Of interest is also the value of $k_1 \approx 48.7113$, where because of the no shear strain boundary conditions, there is a moment in which both orientation angles are null and aligned with the composite material and as a consequence no shear strain is present in each material phase.

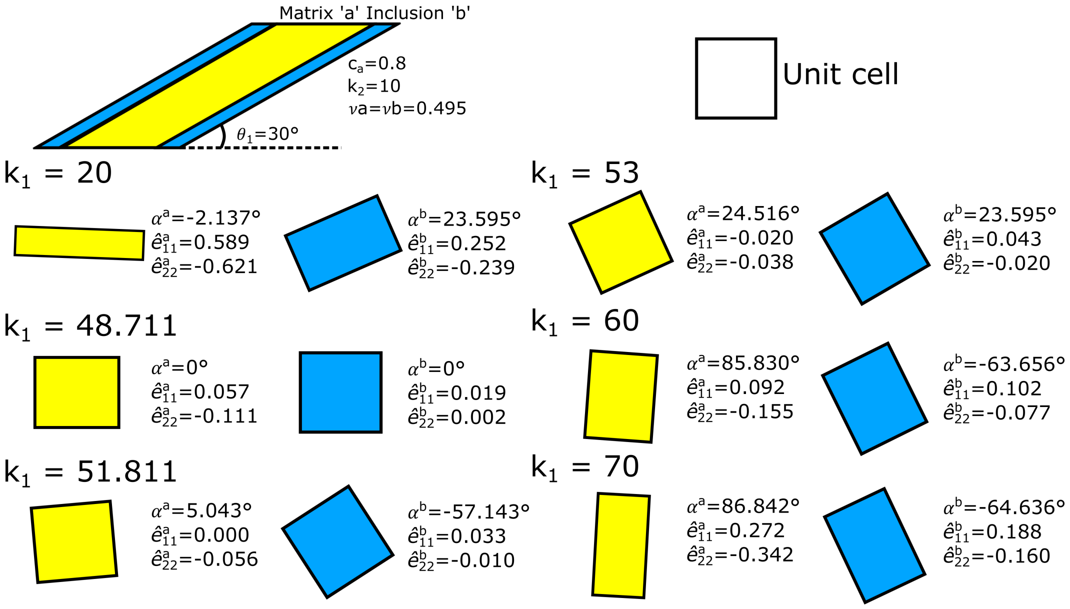

Fig. 5.5 Rank-1 actuation under aligned loading. Diagram showing how a unit cell of each material phase is deformed and rotated as k_1 is varied. Parameters of $\theta_1 = 30°$ and $k_2 = 10$ are used to achieve a response. A volume fraction of $c^a = 0.8$ is used and the elastomer is actuated at a fixed $E_2^{av} = 100$ MV/m.

5.1.3 Actuation under macroscopic stress-free conditions

Next the boundary conditions where shear strains are not limited are examined. The analysis follows the previous one with the key difference being that no boundary conditions are specified on the average strain and eqs. (5.9) and (5.11) are used, which is a more realistic scenario. The same material and geometrical parameters are used and similar figures are plotted, showing the values of principal strains and orientation of the principal directions of strain. In this case, the transition parameter to note is almost doubled, at $k_1 = 99.617$. Figure 5.6 shows, as opposed to the previous case, that as k_2 is increased a much higher value of k_1 is needed for the unconventional response, coupled with the optimal lamination angle decreasing. At small values (e.g. $k_2 = 1$), the optimal angle is approximately 30° same as the no shear strain case. As k_2 increases the optimal angle decreases, with $k_2 = 100$ having an optimal angle of approximately 18°. This implies that ideally to enhance the unconventional response, a material is needed that has an increased permittivity without a substantial increase in shear modulus. The k_1 values needed are in general much larger than the previous case, with the only similar value being with the case of $k_2 = 1$. In the case of $k_2 = 100$ a value of $k_1 \approx 518$ is required for the response transition when an optimal angle is used. As before there is an asymptotic behaviour at $\theta_1 \approx 45°$ which stops the unconventional response from being obtained.

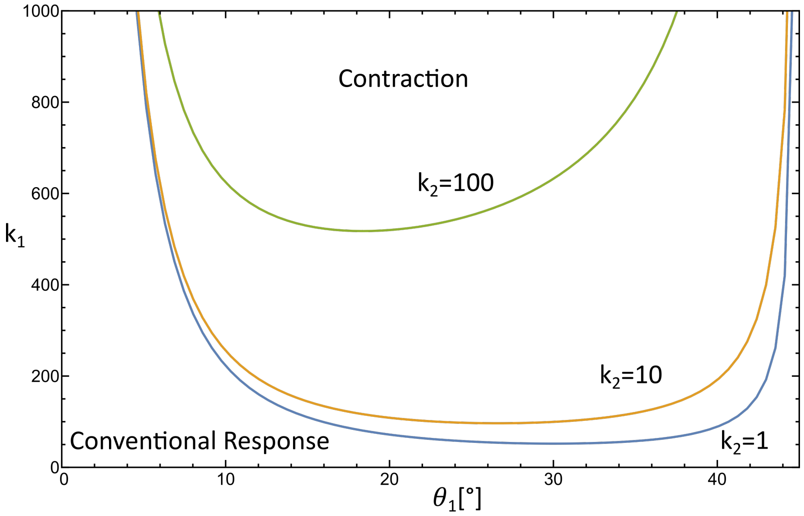

Fig. 5.6 Domains showing inversion of actuation behaviour as k_1 and θ_1 are varied. Orange and blue curves show responses for $k_2 = 10$ and $k_2 = 100$ respectively. Both composites have a volume fraction of $c^a = 0.8$.

Figures 5.7 and 5.8 show the orientation angles and principal strains as k_1 is varied, with the elastomer being actuated at a given external macroscopic electric field $E_2^{av} = 100$ MV/m. Given the fewer boundary restraints, around the transition period there is no large rotation or strains to be seen in the material phases. From the orientation angles it can be seen that, unlike before, both material phases rotate clockwise, with the stiff inclusion rotating right from the start with a steep slope and the soft material phase undergoing a much longer drawn out rotation as k_1 increases. The two angles intersect at a value of $k_1 = 14.155$, however this happens at an angle of $-14.64°$, unlike previously where they both aligned at 0°. Looking at the principal strains does not provide much insight into the occurrence of the response transition. The strains in the stiff inclusion seem to have a minimum at $k_1 = 14.214$, around the value where the orientation angles intercept. However, this is far from the transition value, where the strain curves show a linear caused by the electro-mechanical coupling effects increasing with k_1. Looking at both graphs it can be deduced that the transition occurs because of an interplay between the slowly rotating soft bulk material coupled with the material experiencing increasingly higher strains. The overall transition seems much more gradual than the one with the extra boundary conditions. There are also some behaviours to note that are not highlighted in the figures. When the shear strain is not limited, the composite experiences high negative values of shear strain, which makes it the dominant deformation. In both of the cases with and without shear strain, because of the slight compressibility of the material, the transition in the response in the longitudinal axis occurs before that in the transversal direction.

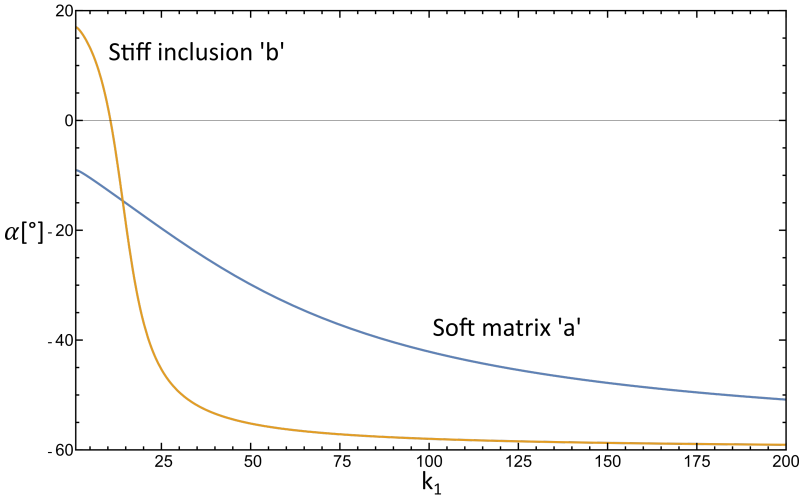

Fig. 5.7 Principal strains orientation angles of the two phases as k_1 is varied. Blue and Orange curves represent the soft and stiff phase respectively. Parameters of $\theta_1 = 30°$ and $k_2 = 10$ are used to achieve a response. A volume fraction of $c^a = 0.8$ is used and the elastomer is actuated at a fixed $E_2^{av} = 100\text{MV/m}$.

5.2 Plane-strain actuation of rank–2 laminates

5.2.1 Homogenisation of rank–2 laminates

The next topic of interest is to assess if a rank–2 laminate can i) confirm and –possibly– ii) enhance the behaviour of the previously discussed rank–1 composite. Because of the electro-elastic small-strain setting, the work done by Tian et al. [60] and Tevet-Deree [57] is followed, which introduced an iterative procedure to compute the effective response of a laminate with a generic rank.

Figure 5.1 (b) shows a sketch of a rank–2 laminate that is made up of a core phase, which is a rank–1 composite with a soft and stiffer material, and an –outer– matrix phase which consists of the same soft material. The core has a lamination angle of θ_1 which is independent of θ_2 which describes the inclination of the matrix. The field equations to be satisfied in each phase are still $(5.2)_{1,2}$, however, now it is convenient to write the constitutive equations as

$$\boldsymbol{D} = \boldsymbol{M}\boldsymbol{E}, \quad \boldsymbol{S} = \mathbb{C}\boldsymbol{e} + \mathbb{A}\boldsymbol{E} \otimes \boldsymbol{E}. \tag{5.14}$$

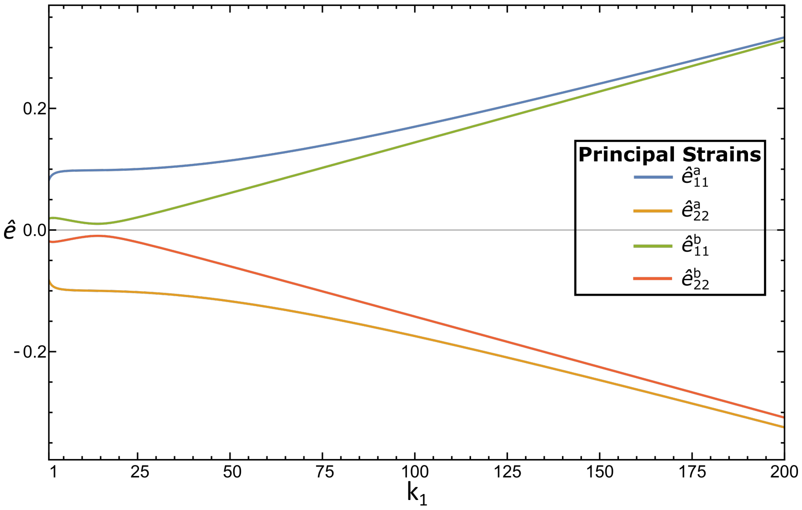

Fig. 5.8 Principal strains of the two phases as k_1 is varied. Curves represent the various principal strains in the two phases. Parameters of $\theta_1 = 30°$ and $k_2 = 10$ are used to achieve a response. A volume fraction of $c^a = 0.8$ is used and the elastomer is actuated at a fixed $E_2^{av} = 100\text{MV/m}$.

$\boldsymbol{M}$ is the second-order tensor of dielectric modulus, while $\mathbb{C}$ and $\mathbb{A}$ are the fourth-order tensors of elastic modulus and electro-mechanical coupling, respectively. For a homogeneous phase, using eqs. (5.8), the non-zero components take the form:

$$\begin{gathered}
C_{1111} = C_{2222} = B + \frac{4G}{3}, \quad C_{1122} = C_{2211} = B - \frac{4G}{3}, \\
C_{1212} = C_{1221} = C_{2112} = C_{2121} = G, \\
A_{1111} = A_{2222} = \frac{\varepsilon}{2}, \quad A_{1122} = A_{2211} = -\frac{\varepsilon}{2}, \\
A_{1212} = A_{1221} = A_{2112} = A_{2121} = \frac{\varepsilon}{2}, \\
M_{11} = M_{22} = \varepsilon. \qquad (5.15)
\end{gathered}$$

To deal with homogenisation of sub-rank laminates, the electrostatic and elastic concentration tensors are introduced, $\boldsymbol{g}$ and $\mathbb{G}$, respectively, relating the fields in each phase to the average fields in the composite, componentwise

$$E_i = g_{ij} E_j^{av}, \quad e_{ij} = G_{ijkl} e_{kl}^{av}. \qquad (5.16)$$

It has been shown in [60] that the effective coupling and elastic moduli tensors for a rank–N material can be obtained using the expressions

$$A^{av}_{ijkl} = \sum_{r=1}^{N} c^{(r)} A^{(r)}_{mnpq} G^{(r)}_{mnij} g^{(r)}_{pk} g^{(r)}_{ql}, \quad C^{av}_{ijkl} = \sum_{r=1}^{N} c^{(r)} C^{(r)}_{ijpq} G^{(r)}_{pqkl}. \tag{5.17}$$

These effective coupling tensors allow the effective macroscopic strain tensor to be calculated. By using eq. $(5.14)_2$ and the governing equation in $\boldsymbol{S}$, eq. $(5.2)_2$, the expression

$$e^{av}_{ij} = C^{av^{-1}}_{abij} (A^{av}_{abkl} E^{av}_{k} E^{av}_{l}) \tag{5.18}$$

is obtained, which allows the average strain to be calculated knowing just the elastic modulus and coupling tensor. As $\mathbb{C}^{-1}$ may be hard to calculate, in Appendix B a method to solve this equation is provided, which also has the benefit of not requiring $\mathbb{G}$ to be calculated. It may also be useful to calculate the effective dielectric modulus, given by

$$\boldsymbol{M}^{av} = \sum_{r=1}^{N} c^{(r)} \boldsymbol{M}^{(r)} \boldsymbol{g}^{(r)}. \tag{5.19}$$

5.2.2 In-plane contraction of rank–2 laminates

A rank–2 composite is analysed where the matrix is the same as the soft material in the core. The equivalent properties of the core will be denoted by subscript c whereas the matrix of the rank–2 will be denoted by subscript d. In the current composite, the volume fraction of the core c_c and the volume fraction of the matrix c_d are related by the expression $c_c + c_d = 1$. To compare the performance of a rank–2 to that of a rank–1, an equivalent volume fraction c_{eq} is defined, which would be the equivalent rank–1 volume fraction $c^{(1)}_a$ to achieve the same overall % of soft to stiff material in the two composites. The rank–2 composite volume fractions relate to the rank–1 equivalent volume fraction by

$$(1 - c^{(2)}_a)(1 - c_d) = 1 - c_{eq}, \tag{5.20}$$

where $c^{(2)}_a$ refers to the volume fraction c_a in the rank–2 composite. By fixing one of the two volume fractions of the soft material the other can be obtained using this equation. To obtain a solution for the rank–2 strain, at first the rank–1 procedure is followed, explained in section 5.1.2, to obtain the β, ω_1 and ω_2 parameters. For the rank–2 analysis, the boundary conditions allow for shear strains and as such the rank–1 results from section 5.1.3 are used to compare the rank–2 to. The various tensors $\boldsymbol{g}$, $\mathbb{C}$, $\mathbb{G}$ and $\mathbb{A}$ are obtained from eqs. (5.8) and (5.6) for each material phase of the rank–1, with the dielectric modulus $\boldsymbol{M}$ being the permittivity tensor of each phase given as in eqs. (5.15). These are then used in eqs. (5.17) and (5.19) to obtain the effective coupling and modulus tensors for the overall rank–1 material. The results were checked using eq. (5.18) to give identical strains to the previously obtained effective rank–1 strains. For all the analyses, the previously defined material parameters were used with $G^a = G^d = 100$ kPa and $\varepsilon^a = \varepsilon^d = 4.68\,\varepsilon_0$. The stiff material is again defined by the k_1 and k_2 constants relating as before. When comparing rank–1 and rank–2 strains, picking for example values of $k_1 = k_2 = 10$ similar results shown by various articles [52, 59, 50, 60] were obtained, where the rank–2 exhibits overall larger achievable strains. When the angles and volume fractions were picked to produce the highest strains, the rank–2 composite showed around 5% larger deformations than an equivalent rank–1 composite.

In this section it is of particular interest whether the rank–2 composite can enhance the transition from the conventional response to the unconventional response. In a rank–2 composite there are multiple parameters which can be varied to change the response to actuation. In this section an ‘optimal’ rank–2 is defined as having the various parameters optimised to enhance the transition between the conventional and unconventional response. To compare the rank–2 response an equivalent optimal rank–1 composite is needed. The rank–1 composite lamination angle can be optimised for a given k_2, shown previously in Fig. 5.6. In this case it was chosen to optimise for a low k_2 hence picking a θ_1 of 30°. The combination of lamination angles in a rank–2 composite greatly affects the transition between the two responses.

Figure 5.9 and 5.10 illustrate how the angles affect the inversion of actuation domains for the rank–2 composite. Both of these figures show a rank–2 composite curve (in orange) with an equivalent volume fraction of $c_{eq} = 0.5$ and are compared to the optimal rank–1 composite curve (in blue) with $c_a^{(1)} = 0.5$. Figure 5.10 shows a response for a rank–2 composite with ‘optimal’ parameters. It can be seen that the curve is almost flat and has a horizontal asymptote as k_2 increases. The parameters were optimised to lower this asymptote such that the inversion of actuation appears with as low a k_1 as possible. The parameters shown to achieve this were a volume fraction of $c_d = 0.1$ and lamination angles of $\theta_1 = 48°$ and $\theta_2 = 93°$. Figure 5.9 keeps the same volume fraction but the angles are changed to demonstrate a suboptimal parameter choice with a $\theta_1 = 30°$ and $\theta_2 = 25°$. These two figures show that when optimal parameters are picked the rank–2 shows an inversion of actuation with a lower k_1 across almost the whole domain except for very low values of k_2. However, when suboptimal lamination angles are picked, the rank–1 composite exhibits the inversion at lower k_1 values over the whole domain. In Fig. 5.9 it is also evident that for certain suboptimal parameters the domain of inversion of actuation is enclosed within the curve and there is no inversion of actuation appearing with larger values of k_2. The general trend is that when $\theta_1 > \theta_2$, the domain is enclosed by the curve; The optimal response for a rank–2 is obtained when $\theta_2 > \theta_1$. When the two lamination angles in the rank–2 composite are equal, the matrix and core align with each other creating a composite equivalent to the rank–1 composite and as such the rank–1 response is obtained as expected.

Figure 5.11 shows the same domain of inversion of actuation with optimal parameters chosen. In this figure, the volume fractions were changed to $c_{eq} = 0.84$ and a $c_d = 0.17$ and the rank–2 curve is plotted with the appropriate equivalent rank–1. The angles used were $\theta_1 = 50°$ and $\theta_2 = 95°$ for the rank–2 composite and the usual $\theta_1 = 30°$ for the rank–1. The optimal response can be seen to be almost identical to the one previously shown with a higher percentage of stiff material, as the graph is only shifted upwards.

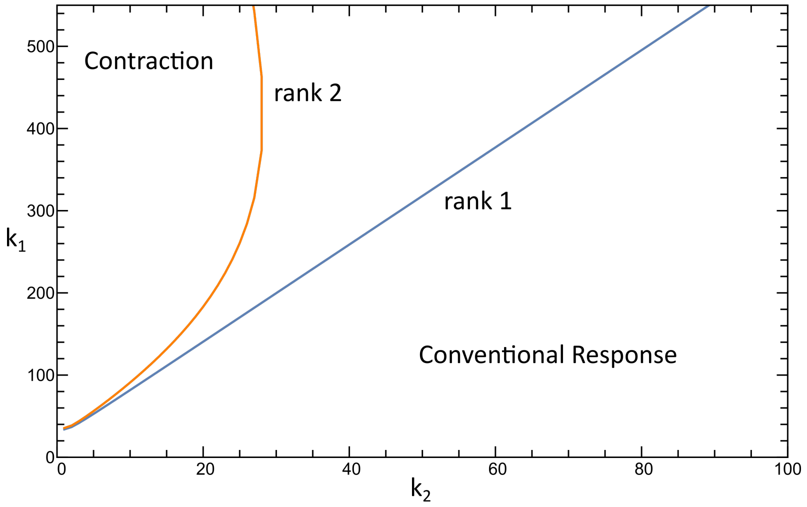

Fig. 5.9 Domains showing inversion of actuation for rank–1 and 2 composites with optimal and suboptimal parameters respectively. The volume fractions used are $c_a^{(1)} = 0.5$ the rank–1 and the rank–2 having a $c_{eq} = 0.5$ and $c_d = 0.1$. The angles used are $\theta_1 = 30°$ for the rank–1 composite and $\theta_1 = 30°$ and $\theta_2 = 25°$ for the rank–2 composite.

Figure 5.12 shows how the volume fraction c_d of the rank–2 composite, with a given equivalent fraction, relates to the value of k_1 needed for the inversion of actuation. In this analysis a $k_2 = 100$ was used, as this approaches the horizontal asymptote displayed when using optimal parameters. For each value of c_d the lamination angles needed to be optimised to give the lowest possible

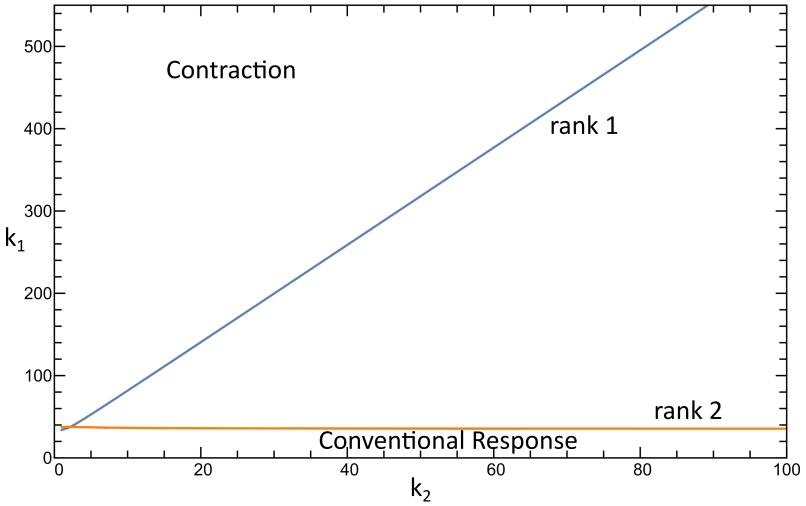

Fig. 5.10 Domains showing inversion of actuation for rank–1 and 2 composites with optimal parameters for both. The volume fractions used are $c_a^{(1)} = 0.5$ the rank–1 and the rank–2 having a $c_{eq} = 0.5$ and $c_d = 0.1$. The angles used are $\theta_1 = 30°$ for the rank–1 composite and $\theta_1 = 48°$ and $\theta_2 = 93°$ for the rank–2 composite.

k_1 value, and each dot represents every case for which this optimisation was undertaken. When $c_d \to 0$ and $c_d \to c_{eq}$ the rank–2 composite exhibits a rank–1 composite response. This is expected as either the matrix vanishes or the core has to be made up of only the stiff material for the two respective cases. The figure shows that for all the volume fractions in between these two values the rank–2 composite with ideal parameters exhibits the inversion of actuation for lower values of k_1 as compared to an optimal rank–1 composite. The optimal matrix volume fraction c_d is shown to be 0.1 and 0.17 for an equivalent fraction c_{eq} of 0.5 and 0.84 respectively. Overall this analysis shows that to create a rank–2 composite capable of enhancing the unconventional response, optimal parameters to start with are a volume fraction for the rank–2 matrix of around 10-20% and lamination angles of $\theta_1 \approx 50°$ and $\theta_2 \approx 95°$.

Next the longitudinal and shear strains in a rank–1 and rank–2 composite are analysed to better understand the performance of each. The effective ('average') strain in the rank–1 and rank–2 is defined as $\boldsymbol{e}^1$ and $\boldsymbol{e}^2$ respectively. To analyse the strains the optimal rank–2 composite from Fig. 5.11 is used with a $c_{eq} = 0.84$. A fixed value of k_2 is chosen and k_1 is varied, actuating both rank–2 and rank–1 composites with a fixed electric field of $E_2^{av} = 10$ MV/m. Figure 5.13 illustrates these results with (a) and (b) having a fixed k_2 of 5 and 20 respectively. The main difference between the rank–1 and rank–2 composite is that for both the shear and longitudinal strain the rank–2 composite exhibits horizontal asymptotes as k_1 increases whereas the rank–1 composite increases linearly. It can be seen that this asymptote helps to limit shearing of the composite with low values of k_1. Both rank–1 and 2 composites exhibit very similar shear strains, until the asymptote occurs, which then limits shearing in the rank–2 composite. In terms of longitudinal strain, after the occurrence of the inversion of actuation, the rank–2 composite exhibits bigger deformations until the curve intersects with that of the rank–1 composite, due to the asymptote. For lower values of k_2 (e.g. (a)) this occurs quite quickly, at around $k_1 \approx 250$, and the two composites perform similarly. However, as k_2 is increased (e.g. (b)) the rank–2 composite exhibits higher deformations and the intersection point happens at a much higher value of around $k_1 \approx 800$. As k_2 is increased further the rank–2 composite outperforms the rank–1 in any physically meaningful domain as the intersection points quickly moves further away. This analysis shows that the rank–2 composite with optimal parameters can be used to not only outperform the rank–1 composite in terms of larger deformations but also limit the shear strain which, in a rank–1 composite, is higher than the longitudinal strain over the whole unconventional response domain. It is also to note that the 'optimal' parameters used throughout this chapter have been defined with the goal of optimising the material parameters and geometrical parameters to hasten the occurrence of the actuation inversion. It is also possible, if for example the material parameters are predefined, to optimise the rank–2 geometric parameters such that the rank–2 experiences its largest negative strains with the given materials. In such a case the angles and volume fractions would be different to the ones used. An example of this can be seen by the dotted lines in (b), where the rank–2 composite has been optimised such that the maximum negative strain is achieved when $k_2 \approx 20$ and $k_1 \approx 400$. The parameters used to obtain this curve were $c_d = 0.05$, $\theta_1 = 56.1°$ and $\theta_2 = 95.4°$. It can be seen that even though the inversion of actuation happens at a larger value of k_1 when $k_1 = 400$ the longitudinal strain is 2.6x larger compared to the 'optimal' rank–2 and 5.6x larger compared to the rank–1. Although the shear strains are larger as well, it is still not the leading deformation as would be the case in the rank–1 composite, because of the previously discussed asymptote.

Figures 5.14 are 3D plots of the longitudinal strain against the two lamination angles for a rank–2 composite. To note that when $\theta_1 = \theta_2$ the rank–1 behaviour is obtained, highlighted in the plots with a blue line. The minima are marked with green and blue dots, for the rank–2 and rank–1 respectively. The volume parameters are of $c_d = 0.17$ with an equivalent volume fraction of $c_{eq} = 0.84$. The two figures have different material ratios with (a) having $k_1 = 300$ and $k_2 = 20$ and (b) having $k_1 = 300$ and $k_2 = 300$. The composite is actuated at a fixed $E_2^{av} = 10$MV/m. The values chosen are not the optimal volume fractions, which can be further optimised, but they do show the general trends. Figure 5.14 (a) highlights that when k_2 is smaller than k_1 a rank–1 composite will always perform better in the traditional deformation mode (longitudinal expansion) no matter what lamination angles for the rank–2 are chosen. In Figure 5.14 (b), when the same material parameters are picked, $k_1 = k_2 = 300$ the rank–2 performs better in both positive and negative strains given optimal lamination angles. The rank–1 exhibits no inversion, with the minima occurring when the rank–1 lamination angle $\theta = 0$ and the actuation strain being close to null. The figures show that a rank–2 configuration can always be optimised to achieve larger negative strains as compared to the rank–1 composite. Overall the rank–2 composite can outperform the rank–1, but a careful study of the geometry and material parameters needs to be undertaken as the results vary greatly with small parameter changes. It is also to note that the typically studied case is when the material constants k_1 and k_2 are equal which allows the rank–2 to enhance the traditional deformation mode; However, if they are not the same it is erroneous to assume that the rank–2 will always outperform a rank–1 composite and care is needed when picking the design based on the requirements.

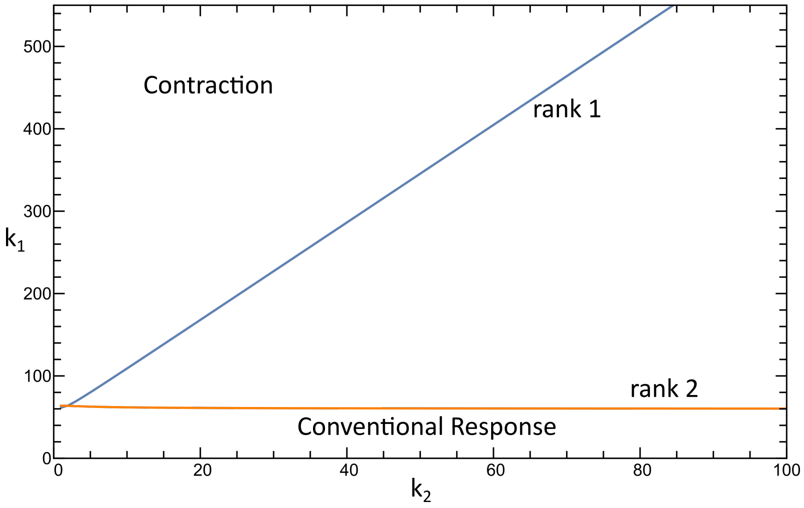

Fig. 5.11 Domains showing inversion of actuation for rank–1 and 2 composites with optimal parameters for both. The volume fractions used are $c_a^{(1)} = 0.84$ the rank–1 and the rank–2 having a $c_{eq} = 0.84$ and $c_d = 0.17$. The angles used are $\theta_1 = 30°$ for the rank–1 composite and $\theta_1 = 50°$ and $\theta_2 = 95°$ for the rank–2 composite.

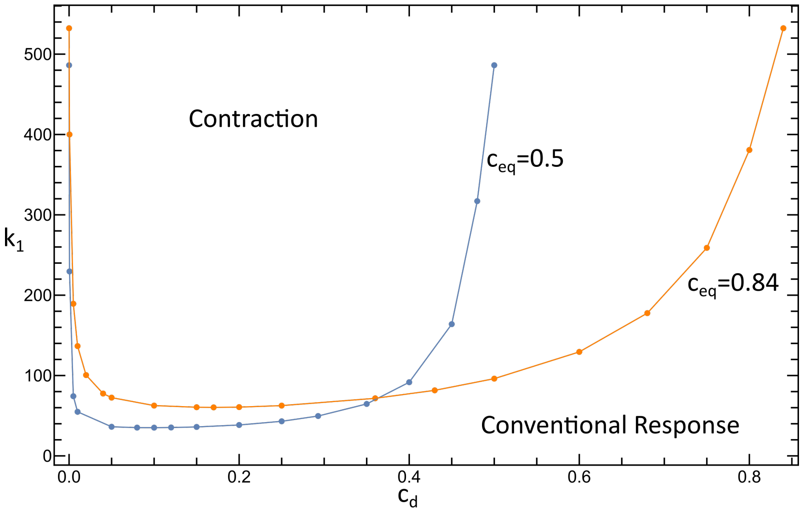

Fig. 5.12 Domain showing inversion of actuation for rank–1 and 2 composites with optimal parameters as c_d is varied against k_1. A value of $k_2 = 100$ is used and lamination angles are optimised for each dot.

5.3 Viability given currently available materials

In the previous sections an analysis was undertaken by changing the material parameters k_1 and k_2 to show the whole range of responses. However, it is also important to know what materials are currently available to be used, to understand the viability of such composite devices with inverse actuation mode. This section offers a brief view of materials that have been studied which could potentially be used in a composite device.

Following the above analysis, a pair of materials is required, one soft and with low dielectric permittivity and another which is stiffer and has a much higher dielectric permittivity. Ideally only the permittivity ratio k_1 is increased in the second stiffer material. However, an increase in permittivity is usually achieved by implanting some filler material in a soft elastomer matrix which in turn also causes an increase in stiffness. For the soft material a material without any filler is generally recommended either made from silicon or acrylic. It is currently accepted that acrylic elastomer tends to be the picked material for large strain applications, as shown by Michel et al. [81]. The most commonly used commercially available elastomer seems to be VHB™ 4910, with other common commercial brands being THERABAND™, OPPO BAND™ among others. Custom synthetic elastomers can also be used and in general these materials exhibit similar properties. Various researchers have categorised these

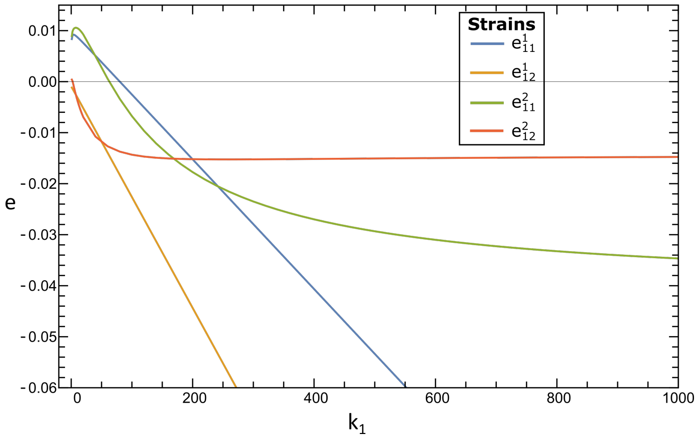

(a) $k_2 = 5$

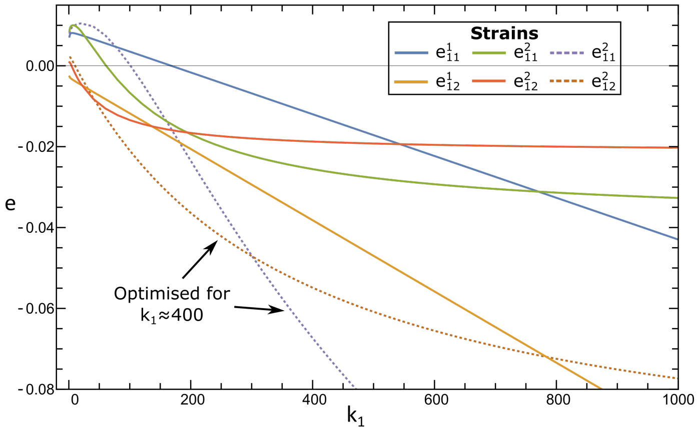

(b) $k_2 = 20$

Fig. 5.13 The longitudinal and shear strains are shown against a varying k_1 of a rank–1 and rank–2 composite, actuated at a fixed $E_2^{av} = 10\text{MV/m}$. Optimal parameters are used with an equivalent volume fraction of $c_{eq} = 0.84$ and figures (a) and (b) having a fixed k_2 of 5 and 20 respectively.

materials showing that generally they exhibit a dielectric permittivity constant ε between 2-10 and a shear modulus μ between 50kPa and 1MPa [82–86]. Overall the material parameters used throughout this thesis of $\mu = 100\text{kPa}$ and $\varepsilon = 4.68$ represent a good approximation for a generic acrylic elastomer to be used as a soft phase material.

It was shown how in the rank–1, with the more realistic stress-free configuration, the k_2 needs to be kept low for realistic values of k_1. In the rank–2 configuration this requirement is nullified as shown in Fig. 5.11, which makes the rank–2 composite a much more viable configuration to achieve the inverse deformation mode. When looking for a suitable stiff material the threshold for the rank–2 composite requires a $k_1 > 40$. Two strategies have been developed to improve the dielectric constant of elastomers [87]. The first is blending the elastomer material with a highly polarizable ceramic such as barium titanate [88, 89], titanium dioxide [90], or calcium copper titanate [91]. This method does not seem to provide very high permittivities, with most of these materials having a $k_1 < 5$. The second method consists of improving the permittivity by the addition of conductive fillers into the matrix, such as carbon nanotubes [92–94] and graphene sheets [95–97], to form conductive filler/polymer composites. These materials seem much more suitable, with permittivity ratios reaching the hundreds. Two examples of these are shown with Tian et al. [95] proposed graphene filler material with a $k_1 = 400$ and a $k_2 = 65$, and George et al. [92] proposed a carbon nanotube composite with a $k_1 = 170$ and a $k_2 = 12$. Both of these materials would be suitable in a rank–2 composite to achieve the unconventional response with the first of these just about being able to achieve the inversion of actuation in a rank–1 stress-free composite. Overall it can be seen that the rank–2 composite is much more realistic in providing the studied inverse actuation. New materials, studied with a focus on high permittivities, could in the future allow a rank–1 composite with inverse actuation to also be viable.

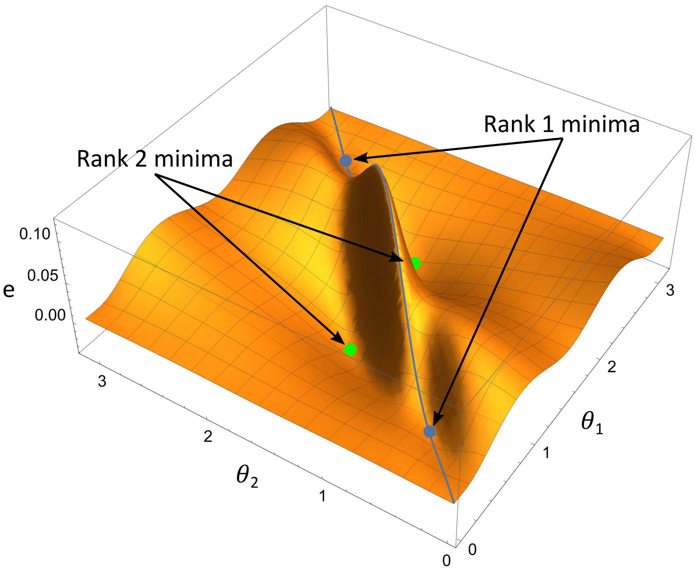

(a) $k_1 = 300, k_2 = 20$

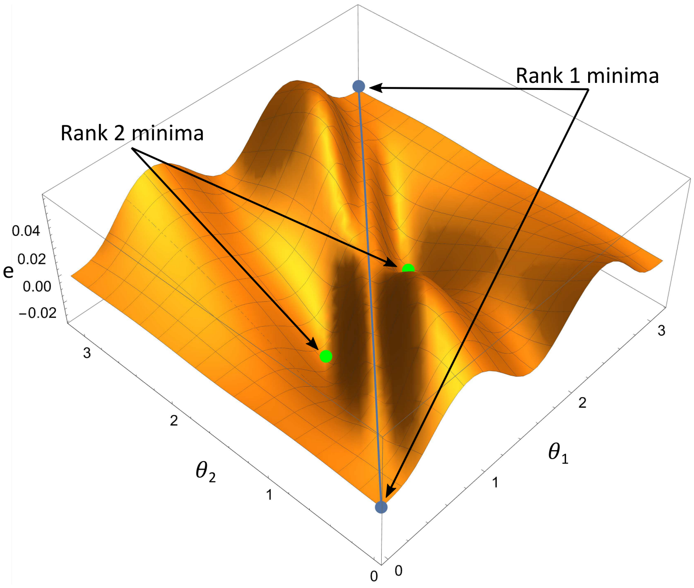

(b) $k_1 = k_2 = 300$

Fig. 5.14 3D plot of the longitudinal strain as θ_1 and θ_2 are varied. The blue line shows the loading path for a rank–1 composite with the dots showing the minimum strains. The two figures have different k_1 and k_2 values. A parameter of c_d=0.17 is used with an equivalent volume fraction of $c_{eq} = 0.84$. The composite is actuated at a fixed $E_2^{av} = 10\text{MV/m}$.

Chapter 6

Concluding Remarks

This thesis aids the design of DE devices by improving the overall understanding of actuation and stability of various configurations. To reach this goal three ways to actuate an elastomer slab devices were introduced (possibly pre-stressed), namely, actuation by means of (i) attached compliant electrodes, (ii) sprayed charges onto the opposite surfaces and (iii) fixed electrodes between which the device 'floats' in vacuum and expands transversally. A tubular 'floating' elastomer configuration was also introduced. Particular attention was taken in analysing the fundamental paths of the more novel 'floating' configurations. The results showed how the elastomer contracts longitudinally and radially in the slab and tubular configuration respectively, as opposed to expanding which appears in the classical configurations. An analysis of the onset of electro-mechanical instability and the approach to the 'expansion limit' was undertaken for both floating geometries, showing how the various geometrical parameters can affect the fundamental loading paths and the onset of instabilities. Experimental results would be needed to confirm this onset of electro-mechanical instability. These have been done for the traditional compliant electrode configuration but up to date no experiments have been done for a floating configuration.

In coupled mechanics, the investigation of surface instabilities is an important step toward the complete understanding of the type of bifurcations occurring in a homogeneous body when subjected to external stimuli. This thesis assesses plane-strain electro-elastic surface instabilities and, in particular, with the aim of assessing the onset of surface instabilities in the 'floating' elastomer configuration and the effect of the stiffness of electrodes in the compliant electrode configuration on the stability domain. Surface instability is tackled for the three actuation modes by specialising the relevant incremental theory, where linearised fields are superimposed on the finite-strain path. The stability domains are obtained in the plane 'longitudinal stretch–dielectric displacement (or voltage jump)'. A first conclusion is that among the three modes, it was shown that the instability is more sensible to pre-stress for specimens in the 'floating' configuration, while a half-space deformed by sprayed charges is more stable than the same actuated by voltage. Surface-coating models can be profitably adopted to investigate the effects of electrodes on surface instabilities. Electrodes composed of three different materials, currently employed in DE devices, were considered and picked to show a wide range of possible stiffnesses. Their implementation in the model considerably changes the stability domain which is significantly reduced when the half-space contracts (a longitudinal stretch of less than one). New bifurcation modes come into play in this enriched approach and each one has been studied and characterised by analysing various incremental fields obtained solving the eigensystem governing the problem.

Composite elastomers are of particular interest in designing DE devices as they are able to enhance the characteristics of the deformation when actuated. It has been previously shown that laminated composites can exhibit improvements in the actuation strain of more than an order of magnitude. This thesis showed that with the right geometrical and material parameters a laminated composite can also exhibit an inversion of actuation, where the elastomer, in a compliant electrode configuration, expands perpendicularly to the electric field as opposed to the typical contraction. A careful study, using a small strain model in plane-strain conditions, was undertaken to categorise the onset of this mode of actuation in regards to the geometrical and material parameters. At first a rank–1 laminate was examined using two different boundary conditions, i.e. aligned loading and macroscopic stress-free conditions. It was shown how in the aligned loading boundary conditions the stiffness ratio between the softer and stiffer materials had almost no effect and the onset of the inverse actuation mode. The onset depends largely on the ratio of permittivities between the two materials. The aligned loading boundary conditions also showed significant changes in the orientation angle of the principal strains and the principal strain trend around the onset of the inverse actuation mode. This allowed the mechanics causing the inverse actuation deformation to be quite evident. In the macroscopic stress-free boundary condition, it was shown in contrast that the stiffness ratio plays a big role in determining the onset of the inverse actuation. The mechanics causing the inverse actuation mode are not as evident and are caused by a gradual change in the strain orientation angles of each phase combined with the principal strains linearly increasing. The macroscopic stress-free condition also exhibits large macroscopic shear strains which make it the dominant deformation. The analysis of a rank–2 laminate under macroscopic stress-free boundary conditions followed, which was compared to the rank–1 results. Overall it was shown that the rank–2 laminate was able to outperform the rank–1 laminate, allowing for much lower permittivity and stiffness ratios to be used, while still obtaining the inverse actuation mode. The deformation was also analysed, showing that the rank–2 limited the shear strain and enhanced the longitudinal contraction. A careful study of the parameters is needed to obtain these results as the rank–2 laminate is very sensitive to changes in both the geometric and material parameters. As such a general guideline was provided to aid the design of rank–2 laminates with the inverse actuation mode. An analysis of currently researched materials showed that currently only one material could potentially be used to obtain the inverse actuation mode for the rank–1 laminate, with small strains when actuated. The rank–2 laminate, due to the enhanced performance, showed a much wider range of potentially viable materials. As such, with currently available material technology, a rank–2 laminate composite is required for devices trying to exploit this inverse actuation mode. Future discoveries in material science, providing materials with higher permittivities without a significant increase in stiffness, would enhance this mode of actuation further and potentially make a rank–1 laminate design viable.

References

[1] Wen-Bo Li, Wen-Ming Zhang, Hong-Xiang Zou, Zhi-Ke Peng, and Guang Meng. A fast rolling soft robot driven by dielectric elastomer. *IEEE/ASME Trans. Mechatron.*, 23(4):1630–1640, 2018.

[2] Yucheng Tang, Lei Qin, Xiaoning Li, Chee-Meng Chew, and Jian Zhu. A frog-inspired swimming robot based on dielectric elastomer actuators. In *2017 IEEE/RSJ International Conference on Intelligent Robots and Systems (IROS)*, pages 2403–2408, 2017.

[3] Igmo Koo, Kwangmok Jung, Jachoon Koo, Jea-do Nam, Youngkwan Lee, and Hyouk Ryeol Choi. Wearable fingertip tactile display. In *2006 SICE-ICASE International Joint Conference*, pages 1911–1916, 2006.

[4] 4c Engineering. Aws - technology demonstrator. https://www.4cengineering.co.uk/case-studies/aws-ocean-energy-technology-demonstrator/, Oct 2014. Accessed: 2022-12-14.

[5] Deborah M. Greaves, Martyn Hann, Adi Kurniawan, John R. Chaplin, and F. J. M. Farley. The hydrodynamics of air-filled bags for wave energy conversion. 2016.

[6] Giacomo Moretti, Gastone Pietro Rosati Papini, Luca Daniele, David Forehand, David Ingram, Rocco Vertechy, and Marco Fontana. Modelling and testing of a wave energy converter based on dielectric elastomer generators. *Proc. R. Soc. A*, 475(2222):20180566, Feb 2019.

[7] Guggi Kofod, Werner Wirges, Mika Paajanen, and Siegfried Bauer. Energy minimization for self-organized structure formation and actuation. *Appl. Phys. Lett.*, 90(8):081916, Feb 2007.

[8] Jun Shintake, Vito Cacucciolo, Herbert Shea, and Dario Floreano. Soft biomimetic fish robot made of dielectric elastomer actuators. *Soft Rob.*, 5(4):466–474, Aug 2018.

[9] Luigi Calabrese, Alice Berardo, Danilo De Rossi, Massimiliano Gei, Nicola Maria Pugno, and Gualtiero Fantoni. A soft robot structure with limbless resonant, stick and slip locomotion. *Smart Mater. Struct.*, 28(10):104005, Sep 2019.

[10] P. Dubois, S. Rosset, M. Niklaus, M. Dadras, and H. Shea. Voltage control of the resonance frequency of dielectric electroactive polymer (deap) membranes. *J. Microelectromech. Syst.*, 17(5):1072–1081, Oct 2008.

[11] Iain A. Anderson, Todd A. Gisby, Thomas G. McKay, Benjamin M. O'Brien, and Emilio P. Calius. Multi-functional dielectric elastomer artificial muscles for soft and smart machines. *J. Appl. Phys.*, 112(4):041101, Aug 2012.

[12] Chongjing Cao, Stuart Burgess, and Andrew T. Conn. Toward a dielectric elastomer resonator driven flapping wing micro air vehicle. *Front. Rob. AI*, 5, Jan 2019.

[13] Chia-Chu Chiang, Chou-Ching K. Lin, and Ming-Shuang Ju. An implantable capacitive pressure sensor for biomedical applications. *Sens. Actuators, A*, 134(2):382–388, Mar 2007.

[14] Federico Carpi, Gabriele Frediani, Carlo Gerboni, Jessica Gemignani, and Danilo De Rossi. Enabling variable-stiffness hand rehabilitation orthoses with dielectric elastomer transducers. *Med. Eng. Phys.*, 36(2):205–211, Feb 2014.

[15] Luigi Calabrese, Gabriele Frediani, Massimiliano Gei, Danilo De Rossi, and Federico Carpi. Active compression bandage made of electroactive elastomers. *IEEE/ASME Trans. Mechatron.*, 23(5):2328–2337, Oct 2018.

[16] Thomas G. McKay, Benjamin M. O'Brien, Emilio P. Calius, and Iain A. Anderson. Soft generators using dielectric elastomers. *Appl. Phys. Lett.*, 98(14):142903, Apr 2011.

[17] Roy D. Kornbluh, Ron Pelrine, Harsha Prahlad, Annjoe Wong-Foy, Brian McCoy, Susan Kim, Joseph Eckerle, and Tom Low. From boots to buoys: Promises and challenges of dielectric elastomer energy harvesting. *SPIE Proc.*, 7976:797605, Mar 2011.

[18] Eliana Bortot, Ralf Denzer, Andreas Menzel, and Massimiliano Gei. Analysis of a viscous soft dielectric elastomer generator operating in an electrical circuit. *Proc. Appl. Math. Mech.*, 14(1):511–512, Dec 2014.

[19] Tongqing Lu, Cheng Ma, and Tiejun Wang. Mechanics of dielectric elastomer structures: A review. *Extreme Mech. Lett.*, 38:100752, Jul 2020.

[20] W. C. Röntgen. Ueber die durch electricität bewirkten form- und volumenänderungen von dielectrischen körpern. *Ann. Phys.*, 247(13):771–786, 1880.

[21] Ronald E. Pelrine, Roy D. Kornbluh, and Jose P. Joseph. Electrostriction of polymer dielectrics with compliant electrodes as a means of actuation. *Sens. Actuators, A*, 64(1):77–85, Jan 1998.

[22] Ron Pelrine, Roy Kornbluh, Qibing Pei, and Jose Joseph. High-speed electrically actuated elastomers with strain greater than 100%. *Science*, 287(5454):836–839, Feb 2000.

[23] Guo-Ying Gu, Jian Zhu, Li-Min Zhu, and Xiangyang Zhu. A survey on dielectric elastomer actuators for soft robots. *Bioinspiration Biomimetics*, 12(1):011003, Jan 2017.

[24] Ujjaval Gupta, Lei Qin, Yuzhe Wang, Hareesh Godaba, and Jian Zhu. Soft robots based on dielectric elastomer actuators: A review. *Smart Mater. Struct.*, 28(10):103002, 2019.

[25] Jung-Hwan Youn, Seung Mo Jeong, Geonwoo Hwang, Hyunwoo Kim, Kyujin Hyeon, Jihwan Park, and Ki-Uk Kyung. Dielectric elastomer actuator for soft robotics applications and challenges. *Appl. Sci.*, 10(2):640, Jan 2020.

[26] R. Springhetti, E. Bortot, G. deBotton, and M. Gei. Optimal energy-harvesting cycles for load-driven dielectric generators in plane strain. *IMA J. Appl. Math.*, 79(5):929–946, Jun 2014.

[27] Giacomo Moretti, Samuel Rosset, Rocco Vertechy, Iain Anderson, and Marco Fontana. A review of dielectric elastomer generator systems. *Adv. Intell. Syst.*, 2(10):2000125, Aug 2020.

[28] Xuanhe Zhao and Zhigang Suo. Method to analyze electromechanical stability of dielectric elastomers. *Appl. Phys. Lett.*, 91(6):061921, Aug 2007.

[29] Yipin Su, Bin Wu, Weiqiu Chen, and Chaofeng Lü. Optimizing parameters to achieve giant deformation of an incompressible dielectric elastomeric plate. *Extreme Mech. Lett.*, 22:60–68, May 2018.

[30] A. Dorfmann and R.W. Ogden. Nonlinear electroelastostatics: Incremental equations and stability. *Int. J. Eng. Sci.*, 48(1):1–14, Jan 2010.

[31] Katia Bertoldi and Massimiliano Gei. Instabilities in multilayered soft dielectrics. *J. Mech. Phys. Solids*, 59(1):18–42, Jan 2011.

[32] Jiangshui Huang, Samuel Shian, Roger M. Diebold, Zhigang Suo, and David R. Clarke. The thickness and stretch dependence of the electrical breakdown strength of an acrylic dielectric elastomer. *Appl. Phys. Lett.*, 101(12):122905, Sep 2012.

[33] R. A. Toupin. The elastic dielectric. *Arch. Ration. Mech. Anal.*, 5(6):849–915, 1956.

[34] RobertM. McMeeking and ChadM. Landis. Electrostatic forces and stored energy for deformable dielectric materials. *J. Appl. Mech.*, 72(4):581–590, Jul 2005.

[35] A. Dorfmann and R. W. Ogden. Nonlinear electroelasticity. *Acta Mech.*, 174(3-4):167–183, Jan 2005.

[36] Z Suo, X Zhao, and W Greene. A nonlinear field theory of deformable dielectrics. *J. Mech. Phys. Solids*, 56(2):467–486, Feb 2008.

[37] Yuhai Xiang, Danming Zhong, Peng Wang, Tenghao Yin, Haofei Zhou, Honghui Yu, Chinmay Baliga, Shaoxing Qu, and Wei Yang. A physically based visco-hyperelastic constitutive model for soft materials. *J. Mech. Phys. Solids*, 128:208–218, Jul 2019.

[38] RobertM. McMeeking and ChadM. Landis. Electrostatic forcesand stored energy for deformable dielectricmaterials. *J. Appl. Mech.*, 72(4):581–590, Aug 2004.

[39] Xuanhe Zhao, Wei Hong, and Zhigang Suo. Electromechanical hysteresis and coexistent states in dielectric elastomers. *Phys. Rev. B: Condens. Matter*, 76(13):134113, Oct 2007.

[40] Xuanhe Zhao and Zhigang Suo. Electrostriction in elastic dielectrics undergoing large deformation. *J. Appl. Phys.*, 104(12):123530, Dec 2008.

[41] Christoph Keplinger, Martin Kaltenbrunner, Nikita Arnold, and Siegfried Bauer. Röntgen's electrode-free elastomer actuators without electromechanical pull-in instability. *PNAS*, 107(10):4505–4510, Feb 2010.

[42] R. Díaz-Calleja, M. J. Sanchis, and E. Riande. Effect of an electric field on the bifurcation of a biaxially stretched incompressible slab rubber. *Eur. Phys. J. E*, 30(4):417, Dec 2009.

[43] Yipin Su, Weiqiu Chen, Luis Dorfmann, and Michel Destrade. The effect of an exterior electric field on the instability of dielectric plates. *Proc. R. Soc. A*, 476(2239):20200267, Jun 2020.

[44] A. Dorfmann and R. W. Ogden. Nonlinear electroelastic deformations. *J. Elast.*, 82(2):99–127, Mar 2006.

[45] Jian Zhu, Hristiyan Stoyanov, Guggi Kofod, and Zhigang Suo. Large deformation and electromechanical instability of a dielectric elastomer tube actuator. *J. Appl. Phys.*, 108(7):074113, Oct 2010.

[46] Luis Dorfmann and Ray W. Ogden. Instabilities of soft dielectrics. *Philos. Trans. R. Soc. A*, 377(2144):20180077, Mar 2019.

[47] Luis Dorfmann and Ray W. Ogden. Instabilities of an electroelastic plate. *Int. J. Eng. Sci.*, 77:79–101, Apr 2014.

[48] R. Díaz-Calleja, P. Llovera-Segovia, and A. Quijano-López. Complex bifurcation maps in electroelastic elastomeric plates. *Int. J. Solids Struct.*, 113-114:70–84, May 2017.

[49] Yipin Su, Hannah Conroy Broderick, Weiqiu Chen, and Michel Destrade. Wrinkles in soft dielectric plates. *J. Mech. Phys. Solids*, 119:298–318, Oct 2018.

[50] Stephan Rudykh and Gal deBotton. Stability of anisotropic electroactive polymers with application to layered media. *Z. Angew. Math. Phys.*, 62(6):1131–1142, Jun 2011.

[51] S. Rudykh, K. Bhattacharya, and G. deBotton. Multiscale instabilities in soft heterogeneous dielectric elastomers. *Proc. R. Soc. A*, 470(2162):20130618, Feb 2014.

[52] Stephen A. Spinelli and Oscar Lopez-Pamies. Some simple explicit results for the elastic dielectric properties and stability of layered composites. *Int. J. Eng. Sci.*, 88:15–28, Mar 2015.

[53] A.I. Murdoch. The propagation of surface waves in bodies with material boundaries. *J. Mech. Phys. Solids*, 24(2-3):137–146, Jun 1976.

[54] D. J. Steigmann and R. W. Ogden. Elastic surface-substrate interactions. *Proc. R. Soc. A*, 455(1982):437–474, Feb 1999.

[55] R.W. Ogden and D.J. Steigmann. Plane strain dynamics of elastic solids with intrinsic boundary elasticity, with application to surface wave propagation. *J. Mech. Phys. Solids*, 50(9):1869–1896, Sep 2002.

[56] G. deBotton, L. Tevet-Deree, and E. A. Socolsky. Electroactive heterogeneous polymers: Analysis and applications to laminated composites. *Mech. Adv. Mater. Struct.*, 14(1):13–22, Jun 2007.

[57] Limor Tevet-Deree. *Electroactive Polymer Composites: Analysis and Simulation*. PhD thesis, Ben-Gurion University, 2008.

[58] Massimiliano Gei, Roberta Springhetti, and Eliana Bortot. Performance of soft dielectric laminated composites. *Smart Mater. Struct.*, 22(10):104014, Sep 2013.

[59] Massimiliano Gei and Kudzai C.K. Mutasa. Optimisation of hierarchical dielectric elastomer laminated composites. *Int. J. Non Linear Mech.*, 106:266–273, Nov 2018.

[60] L. Tian, L. Tevet-Deree, G. deBotton, and K. Bhattacharya. Dielectric elastomer composites. *J. Mech. Phys. Solids*, 60(1):181–198, Jan 2012.

[61] C. Truesdell, Walter Noll, and S. S. Antman. *The non-linear field theories of Mechanics*. Springer-Verlag, 2004.

[62] Morton Edward Gurtin. *An introduction to continuum mechanics*. Academic press, 1982.

[63] Gerhard A. Holzapfel. *Nonlinear solid mechanics: A continuum approach for engineering*. John Wiley & Sons, 2010.

[64] Yongquan Wang, Huanhuan Xue, Hualing Chen, and Junhua Qiang. A dynamic visco-hyperelastic model of dielectric elastomers and their energy dissipation characteristics. *Appl. Phys. A*, 112(2):339–347, May 2013.

[65] Michael Wissler and Edoardo Mazza. Mechanical behavior of an acrylic elastomer used in dielectric elastomer actuators. *Sens. Actuators, A*, 134(2):494–504, Mar 2007.

[66] M. Agoras, O. Lopez-Pamies, and P. Ponte Castañeda. A general hyperelastic model for incompressible fiber-reinforced elastomers. *J. Mech. Phys. Solids*, 57(2):268–286, Feb 2009.

[67] Ronald Samuel Rivlin. Large elastic deformations of isotropic materials iv. further developments of the general theory. *Philos. Trans. R. Soc. London, Ser. A*, 241(835):379–397, Oct 1948.

[68] A. N. Gent. A new constitutive relation for rubber. *Rubber Chem. Technol.*, 69(1):59–61, Mar 1996.

[69] M. Kurimoto, K. Naya, T. Kato, and Y. Suzuoki. Influence of elastomer material and stretch direction on relative permittivity of stretched dielectric elastomer. In *2018 IEEE 2nd International Conference on Dielectrics (ICD)*, pages 1–4, 2018.

[70] Massimiliano Gei, Stefania Colonnelli, and Roberta Springhetti. The role of electrostriction on the stability of dielectric elastomer actuators. *Int. J. Solids Struct.*, 51(3-4):848–860, Feb 2014.

[71] R. W. Ogden. *Non-linear elastic deformations.* Dover Publications, 2005.

[72] Morteza H Siboni, Reza Avazmohammadi, and Pedro Ponte Castañeda. Electromechanical instabilities in fiber-constrained, dielectric-elastomer composites subjected to all-around dead-loading. *Math. Mech. Solids*, 20(6):729–759, Oct 2014.

[73] R.T. Edmondson and Y.B. Fu. Stroh formulation for a generally constrained and pre-stressed elastic material. *International Journal of Non-Linear Mechanics*, 44(5):530–537, 2009.

[74] Michael Wissler and Edoardo Mazza. Electromechanical coupling in dielectric elastomer actuators. *Sens. Actuators, A*, 138(2):384–393, Aug 2007.

[75] Massimiliano Gei. Elastic waves guided by a material interface. *Eur. J. Mech. A. Solids*, 27(3):328–345, 2008.

[76] Jose Enrico Quinsaat, Iurii Burda, Ronny Krämer, Daniel Häfliger, Frank A. Nüesch, Mihaela Dascalu, and Dorina M. Opris. Conductive silicone elastomers electrodes processable by screen printing. *Sci. Rep.*, 9(1):13331, Sep 2019.

[77] Mark Kujawski, Justin Pearse, and Elisabeth Smela. Pdms/graphite stretchable electrodes for dielectric elastomer actuators. *Proc. SPIE, Electroactive Polymer Actuators and Devices (EAPAD)*, 7642:76420R, Apr 2010.

[78] M. Niklaus and H.R. Shea. Electrical conductivity and young's modulus of flexible nanocomposites made by metal-ion implantation of polydimethylsiloxane: The relationship between nanostructure and macroscopic properties. *Acta Mater.*, 59(2):830–840, Jan 2011.

[79] H. Shea. Miniaturized eaps with compliant electrodes fabricated by ion implantation. *Proc. SPIE, Electroactive Polymer Actuators and Devices (EAPAD)*, 7976:79760R, Mar 2011.

[80] Xiaobin Ji, Samuel Rosset, and Herbert R. Shea. Soft tunable diffractive optics with multifunctional transparent electrodes enabling integrated actuation. *Appl. Phys. Lett.*, 109(19):191901, Jul 2016.

[81] Silvain Michel, Xuequn Zhang, Michael Wissler, Christiane Löwe, and Gabor Kovacs. A comparison between silicone and acrylic elastomers as dielectric materials in electroactive polymer actuators. *Polym. Int.*, 59(3):391–399, 2009.

[82] Yi Chen, Lorenzo Agostini, Giacomo Moretti, Marco Fontana, and Rocco Vertechy. Dielectric elastomer materials for large-strain actuation and energy harvesting: A comparison between styrenic rubber, natural rubber and acrylic elastomer. *Smart Mater. Struct.*, 28(11):114001, Aug 2019.

[83] Rainer Kaltseis, Christoph Keplinger, Soo Jin Adrian Koh, Richard Baumgartner, Yu Feng Goh, Wee Hoe Ng, Alexander Kogler, Andreas Tröls, Choon Chiang Foo, Zhigang Suo, and et al. Natural rubber for sustainable high-power electrical energy generation. *RSC Adv.*, 4(53):27905–27913, Jun 2014.

[84] Kwangmok Jung, Joonho Lee, Misuk Cho, Ja Choon Koo, Jae-do Nam, Youngkwan Lee, and Hyouk Ryeol Choi. Development of enhanced synthetic elastomer for energy-efficient polymer actuators. *Smart Mater. Struct.*, 16(2):S288, Mar 2007.

[85] L.J. Romasanta, M.A. Lopez-Manchado, and R. Verdejo. Increasing the performance of dielectric elastomer actuators: A review from the materials perspective. *Prog. Polym. Sci.*, 51:188–211, Sep 2015.

[86] Gih-Keong Lau, Zhe-Xian Ren, and Kuan-Ting Chiang. Effect of stretch limit change on hyperelastic dielectric actuation of styrene-ethylene/butylene-styrene (sebs) copolymer organogels. *Smart Mater. Struct.*, 31(9):095019, Jul 2022.

[87] Leipeng Liu, Ying Lei, Zhicheng Zhang, Jinru Liu, Shenghua Lv, and Ziyi Guo. Fabrication of pda@sio2@rgo/pdms dielectric elastomer composites with good electromechanical properties. *React. Funct. Polym.*, 154:104656, May 2020.

[88] Ajeet Kumar, Dilshad Ahmad, Karali Patra, and Mokarram Hossain. Enhancement of electromechanical properties of natural rubber by adding barium titanate filler: An electro-mechanical study. *J. Appl. Polym. Sci.*, 138(39):50991, May 2021.

[89] Liang Jiang, David Kennedy, Stephen Jerrams, and Anthony Betts. Enhancement of dielectric properties with the addition of bromine and dopamine modified barium titanate particles to silicone rubber. *MRS Commun.*, 6(4):437–441, Oct 2016.

[90] Haoliang Liu, Liqun Zhang, Dan Yang, Yingchun Yu, Lu Yao, and Ming Tian. Mechanical, dielectric, and actuated strain of silicone elastomer filled with various types of tio2. *Soft Mater.*, 11(3):363–370, Feb 2013.

[91] Yi Yang Zhang, Gen Lin Wang, Jie Zhang, Ke Hong Ding, Zhi Feng Wang, and Ming Zhang. Preparation and properties of core-shell structured calcium copper titanate@polyaniline/silicone dielectric elastomer actuators. *Polym. Compos.*, 40(S1), Jul 2017.

[92] Neena George, Julie Chandra C.S., A. Mathiazhagan, and Rani Joseph. High performance natural rubber composites with conductive segregated network of multiwalled carbon nanotubes. *Compos. Sci. Technol.*, 116:33–40, May 2015.

[93] Zewang Xu, Shaodi Zheng, Xiaotian Wu, Zhengying Liu, Ruiying Bao, Wei Yang, and Mingbo Yang. High actuated performance mwcnt/ecoflex dielectric elastomer actuators based on layer-by-layer structure. *Composites, Part A*, 125:105527, Jul 2019.

[94] Jin-Young Kim, TaeYoung Kim, Ji Won Suk, Harry Chou, Ji-Hoon Jang, Jong Ho Lee, Iskandar N. Kholmanov, Deji Akinwande, and Rodney S. Ruoff. Enhanced dielectric performance in polymer composite films with carbon nanotube-reduced graphene oxide hybrid filler. *Small*, 10(16):3405–3411, Feb 2014.

[95] Ming Tian, Jing Zhang, Liqun Zhang, Suting Liu, Xiaoqing Zan, Toshio Nishi, and Nanying Ning. Graphene encapsulated rubber latex composites with high dielectric constant, low dielectric loss and low percolation threshold. *J. Colloid Interface Sci.*, 430:249–256, Jun 2014.

[96] Colin G. Cameron, Royale S. Underhill, Marc Rawji, and Jeffrey P. Szabo. Conductive filler: Elastomer composites for maxwell stress actuator applications. *Proc. SPIE*, Jul 2004.

[97] Nanying Ning, Qin Ma, Suting Liu, Ming Tian, Liqun Zhang, and Toshio Nishi. Tailoring dielectric and actuated properties of elastomer composites by bioinspired poly(dopamine) encapsulated graphene oxide. *ACS Appl. Mater. Interfaces*, 7(20):10755–10762, May 2015.

[98] Lixiu Tian. *Effective Behavior of Dielectric Elastomer Composites*. PhD thesis, California Institute of Technology, 2007.

Appendix A

Numerical scheme to solve tubular elastomer device

In section 3.2 the floating elastomer tube was introduced making a distinction between two boundary condition cases, the case with λ_z constant and the case with $\lambda_z(r)$ as a function of the radius. A DAE (eqs. (3.23), (3.31) and (3.32)) was introduced with boundary conditions for each case which require a numerical approach to solve. This appendix will go into detail about the approach used by the author to solve the DAE to obtain the results illustrated in section 3.2.4.

Case with λ_z constant

The simpler case is when λ_z is constant throughout the deformation. First the geometrical values in the undeformed configuration (a, b, c_0 and d_0), together with λ_z are picked. The material for the elastomer tube also needs to be chosen, meaning ε and μ need to be specified. To start the process the desired actuation potential difference Φ is chosen and an initial guess for the deformed inner radius c is made. The deformed outer radius d and the hoop stretch $\lambda_\theta(r)$ are given by eqs. (3.20) and (3.21) in terms of c. The boundary conditions are given by eqs. (3.34). An initial guess of the outer boundary condition $\tau_r(d)$ is made and the DAE is then numerically solved to obtain the function $\tau(r)$ such that the domain is bounded by the initial guess of c and the initial guess of the outer boundary conditions. The domain of the function gives an updated value of d which satisfies the guessed outer boundary condition. The continuity of volume due to the incompressibility of the elastomer is used, by checking the undeformed volume against the deformed volume, using the guessed c and the updated d. The process is iterated by altering the guess for c until the difference in the two volumes is sufficiently small ($< 1\%$ was used). The guessed outer boundary condition is then checked against the value obtained using eq. $(3.21)_2$ and updated accordingly. The process is repeated until both the continuity and outer boundary conditions are sufficiently satisfied ($< 1\%$).

During the numerical study it became apparent that the inner deformed radius c varied linearly with the outer boundary conditions $\tau_r(d)$, with one such case shown in Fig. A.1. Once a few points are calculated and a linear trend can be established, this relation can be leveraged to simplify the process; Instead of guessing c and $\tau_r(d)$ separately, a pair of numbers can be obtained from the linear regression. In this case the pair is used as a guess and Φ varied (instead of c) to quickly get to a close solution that satisfies the continuity of volume. From there only small alterations of c and $\tau_r(d)$ are needed to obtain a more exact solution for the given Φ.

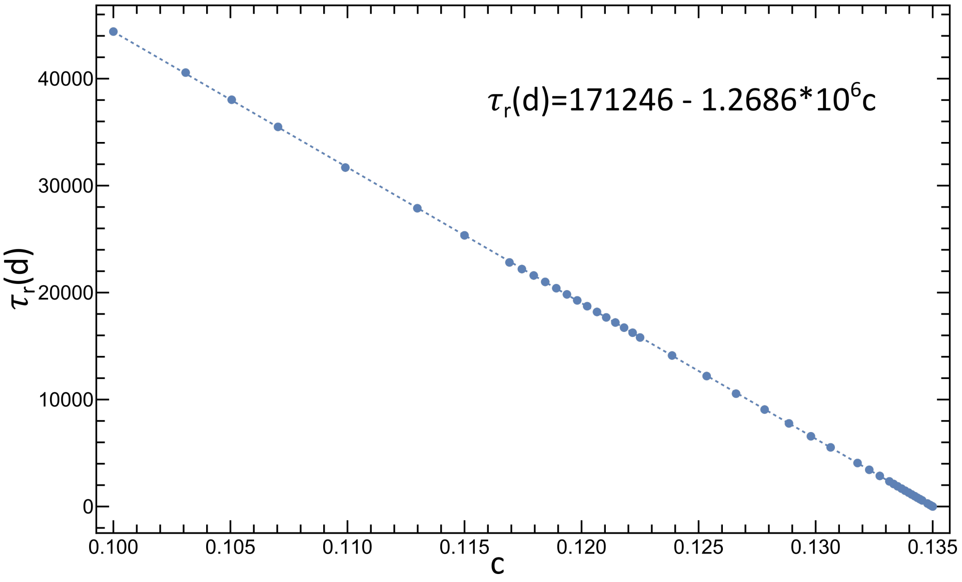

Fig. A.1 The linear relation between c and $\tau_r(d)$ shown using an elastomer with an initial geometry given by $a = 0.1$, $b = 0.2$, $c_0 = 0.135$ and $d_0 = 0.165$ and $\lambda_z = 1$ is constant throughout. The dotted line shows linear regression and dots mark the numerical solutions. The linear equation is shown on the graph.

Case with $\lambda_z(r)$ as a function of radius

When looking at the case with $\lambda_z(r)$ as a function of radius the general method remains the same. The DAE will now have an additional unknown variable that requires using eq. (3.36) to solve for. The previous procedure is followed, however, now d also requires a λ_z guess. As the elastomer is thin a value for λ_z at mid-volume is guessed and then the DAE is solved, as before, to obtain $\lambda_z(r)$. All the guesses are then checked as before, using the continuity of volume and the outer boundary condition, including the guess of λ_z at mid-volume with the newly solved function $\lambda_z(r)$. To note that, as mentioned previously, the continuity of volume now requires integration using eq. (3.37). The procedure is again repeated until the conditions are sufficiently satisfied ($< 1\%$). As Φ increases, it becomes more difficult to satisfy the outer boundary condition as any small change of λ_z or c causes a big change in the Maxwell stress. Because of this, it might be required to relax the outer boundary condition criteria to obtain a solution.

As before it became evident for this case as well that there was a linear trend between the inner deformed radius c and the outer boundary conditions $\tau_r(d)$. This can be leveraged, again, to quickly get a close solution that satisfies the continuity of volume. An example of the linear relation for this case is shown in Fig. A.2.

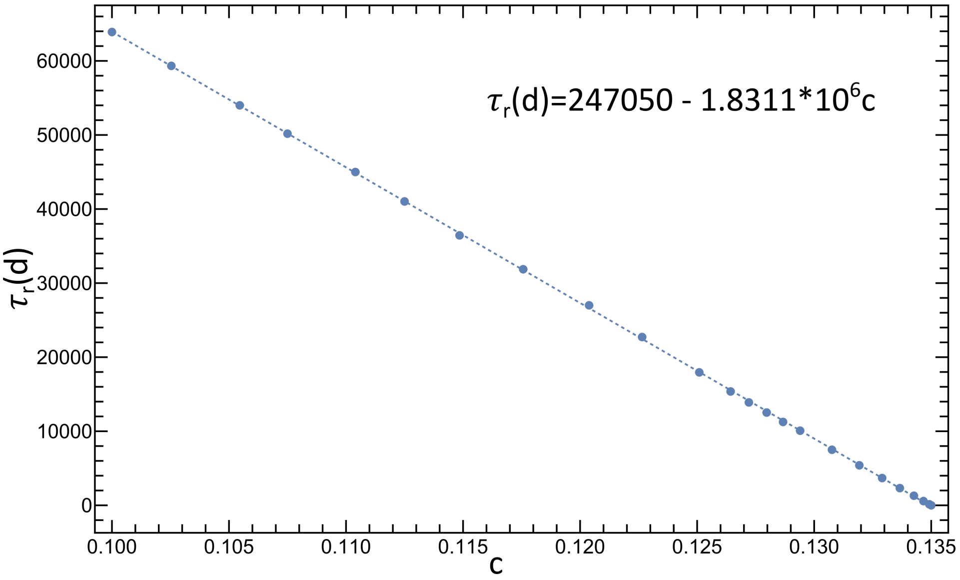

Fig. A.2 The linear relation between c and $\tau_r(d)$ shown using an elastomer with an initial geometry given by $a = 0.1$, $b = 0.2$, $c_0 = 0.135$ and $d_0 = 0.165$ and $\lambda_z(r)$ is a function of the radius. The dotted line shows linear regression and dots mark the numerical solutions. The linear equation is shown on the graph.

Appendix B

Rank–2 solution for macroscopic strain

Here a method is provided to solve the rank two composite eq. (5.18), following the one seen in Tian [98]. The problems that are encountered when trying to solve the equation are that it can be tricky to obtain $\mathbb{C}^{av^{-1}}$ and the average elastic concentration tensor $\mathbb{G}^{av}$. In this method these quantities are calculated implicitly. The jump conditions and the average quantities, eqs. (5.3) and (5.4) are used together with the governing eqs. (5.14) to obtain the following equations

$$\begin{gathered} c^a\boldsymbol{e}^a + c^b\boldsymbol{e}^b = \boldsymbol{e}^{av}, \quad \boldsymbol{m}^0 \cdot (\boldsymbol{e}^a - \boldsymbol{e}^b)\boldsymbol{m}^0 = 0, \\ (\mathbb{C}^a\boldsymbol{e}^a + \mathbb{A}^a\boldsymbol{E}^a \otimes \boldsymbol{E}^a - \mathbb{C}^b\boldsymbol{e}^b - \mathbb{A}^b\boldsymbol{E}^b \otimes \boldsymbol{E}^b)\boldsymbol{n}^0 = \boldsymbol{0}. \end{gathered} \tag{B.1}$$

Plugging the first of these equations into the second two gives

$$\begin{gathered} \boldsymbol{m}^0 \cdot \boldsymbol{e}^a\boldsymbol{m}^0 = \boldsymbol{m}^0 \cdot \boldsymbol{e}^{av}\boldsymbol{m}^0, \\ (c^a\mathbb{C}^b + c^b\mathbb{C}^a)\boldsymbol{e}^a\boldsymbol{n}^0 = \mathbb{C}^a\boldsymbol{e}^{av}\boldsymbol{n}^0 \\ -c^a\Big[\mathbb{A}^a(\boldsymbol{g}^a\boldsymbol{E}^{av} \otimes \boldsymbol{g}^a\boldsymbol{E}^{av}) - \mathbb{A}^b(\boldsymbol{g}^b\boldsymbol{E}^{av} \otimes \boldsymbol{g}^b\boldsymbol{E}^{av})\Big]\boldsymbol{n}^0. \end{gathered} \tag{B.2}$$

A column vector can be defined from any 2 x 2 matrix ψ which will be denote as $\hat{\psi}$ and is given by

$$\hat{\psi} = \begin{bmatrix} \psi_{11} \\ \psi_{22} \\ \frac{1}{\sqrt{2}}(\psi_{12} + \psi_{21}) \end{bmatrix}. \tag{B.3}$$

A 4th order tensor can also be turned into a 2d representation with the appropriate 2d matrices becoming a column vector. An example of this is seen with the constituent relation linking the stress and strain components, which can be expressed with the 2d matrix of the following form,

$$\begin{bmatrix} S_{11} \\ S_{22} \\ \sqrt{2}S_{12} \end{bmatrix} = \begin{bmatrix} C_{1111} & C_{1122} & \sqrt{2}C_{1112} \\ C_{2211} & C_{2222} & \sqrt{2}C_{2212} \\ \sqrt{2}C_{1211} & \sqrt{2}C_{1222} & 2C_{1212} \end{bmatrix} \begin{bmatrix} e_{11} \\ e_{22} \\ \sqrt{2}e_{12} \end{bmatrix}. \tag{B.4}$$

Using this notation T is defined as the row vector generated from the matrix $m_i^0 m_j^0$. For the construct the following matrices also need to be defined,

$$\begin{aligned} L_{mn}^{(i)} &= A_{ijkl}^b g_{km}^b g_{ln}^b n_j - A_{ijkl}^a g_{km}^a g_{ln}^a n_j \\ N_{kl}^{(i)} &= (c^b C_{ijkl}^a + c^a C_{ijkl}^b) n_j \\ O_{kl}^{(i)} &= C_{ijkl}^b n_j, \end{aligned} \tag{B.5}$$

which come from the various components of eq. (B.2)$_2$. Next the following matrices are constructed using the row vector forms of the newly defined matrices L, N and O, as follows

$$P = \begin{bmatrix} \mathbf{0} \\ c^b \hat{L}^{(1)} \\ c^b \hat{L}^{(2)} \end{bmatrix}, R = \begin{bmatrix} T \\ \hat{N}^{(1)} \\ \hat{N}^{(2)} \end{bmatrix}, Q = \begin{bmatrix} T \\ \hat{O}^{(1)} \\ \hat{O}^{(2)} \end{bmatrix}, \tag{B.6}$$

where the $\mathbf{0}$ in the P expression is a 3 component null vector. Equation (B.2)$_2$ can now be rewritten using the constructed matrices in a simpler manner,

$$R\hat{e}^a = Q\hat{e}^{av} + P\tilde{E}, \tag{B.7}$$

where $\tilde{E}$ is the column vector of the matrix $\boldsymbol{E}^{av} \otimes \boldsymbol{E}^{av}$. Solving for $\hat{e}^a$ gives,

$$\hat{e}^a = R^{-1}Q\hat{e}^{av} + R^{-1}P\tilde{E}. \tag{B.8}$$

W is next defined as the matrix form of the fourth order tensor,

$$c^a A_{ijkl}^a g_{km}^a g_{ln}^a + c^b A_{ijkl}^b g_{km}^b g_{ln}^b. \tag{B.9}$$

This is then used with the constructed quantities to obtain an expression of the average total stress (eq. (5.14)$_2$), using the expression of $\hat{e}^a$ and the avarage strain relationship eq. $(5.14)_3$ as,

$$\begin{aligned}\hat{S}^{av} &= c^a\hat{S}^a + c^b\hat{S}^b = c^a\hat{C}^a\hat{e}^a + c^b\hat{C}^b\hat{e}^b + W\tilde{E} \\ &= [\hat{C}^b + c^a(\hat{C}^a - \hat{C}^b)R^{-1}Q]\hat{e}^{av} + [c^a(\hat{C}^a - \hat{C}^b)R^{-1}P + W]\tilde{E}. \end{aligned} \tag{B.10}$$

As previously shown, the total stress is made up of two uncoupled terms, the mechanical and electrical terms. By observation we can thus see that the effective coupling and elastic modulus tensors for the composite can be obtained using the constructed variables as follows,

$$\begin{aligned}\hat{C}^{av} &= \hat{C}^b + c^a(\hat{C}^a - \hat{C}^b)R^{-1}Q, \\ \hat{A}^{av} &= c^a(\hat{C}^a - \hat{C}^b)R^{-1}P + W. \end{aligned} \tag{B.11}$$

These moduli can now be used in the expression,

$$\hat{e}^{av} = \hat{C}^{av^{-1}}(\hat{A}^{av}\tilde{E}) \tag{B.12}$$

to obtain the average strain. As can be seen it is now trivial to obtain the inverse of $\hat{C}^{av}$ and the use of the modulus $\mathbb{G}$, which was previously used to calculate $\mathbb{A}^{av}$, has been incorporated implicitly in the construct.